Fall 2022

Fabrication of Asymmetrical Hollow Fiber-Supported Thin Film Membranes, Stack Assembly, and Accelerated Long-Term Stability Test for Oxygen Production From Air

Myongjin Lee

Recommended Citation

Lee, M.(2022). *Fabrication of Asymmetrical Hollow Fiber-Supported Thin Film Membranes, Stack Assembly, and Accelerated Long-Term Stability Test for Oxygen Production From Air.* (Doctoral dissertation). Retrieved from https://scholarcommons.sc.edu/etd/7097

FABRICATION OF ASYMMETRICAL HOLLOW FIBER-SUPPORTED THIN FILM MEMBRANES, STACK ASSEMBLY, AND ACCELERATED LONG-TERM STABILITY TEST FOR OXYGEN PRODUCTION FROM AIR

by

Myongjin Lee

Bachelor of Engineering
Chonbuk National University, Korea, 2013

Master of Engineering
Chonbuk National University, Korea, 2015

Submitted in Partial Fulfillment of the Requirements

For the Degree of Doctor of Philosophy in

Mechanical Engineering

College of Engineering and Computing

University of South Carolina

2022

Accepted by:

Xingjian Xue, Major Professor

Dongkyu Lee, Committee Member

Guiren Wang, Committee Member

Guoan Wang, Committee Member

Cheryl L. Addy, Interim Vice Provost and Dean of the Graduate School

ACKNOWLEDGEMENTS

I would like to express my deepest appreciation to my advisor Dr. Xingjian Xue. The completion of my dissertation cannot be done without the extraordinary guidance and unwavering support from Dr. Xue. His invaluable insight into research highly affects me as a researcher. Dr. Xue's tremendous help has prepared me to get to this place in my academic life. It has been a great pleasure to work with Dr. Xue over the past seven years.

I am extremely grateful to Dr. Dongkyu Lee, Dr. Guiren Wang and Dr. Guoan Wang for serving as my committee members. I very much appreciate the valuable suggestions and encouragement.

My sincere thanks also go to my group members, Dr. Chunlei Ren, Yun Gan and Chunyang Yang. Whenever I encounter difficulties in my research, they are always there helping me and providing me with insightful suggestions.

I would like to express my special thanks to my parents, my nephew, my sister, my brother-in-law and my friends. They have provided me with endless support and encouragement throughout this entire process.

ABSTRACT

Air separation is a widely used process for oxygen production. Several separation technologies have been developed for air separation, including cryogenic distillation, swing adsorption, redox process of metal oxides, and electrochemical process. Among these technologies, electrochemical permeation process stands out as a cost-effective and simple process for pure oxygen production from air. The electrochemical permeation process employs a gas-tight membrane to permeate and separate oxygen from air directly, where the membrane conducts both ions and electrons simultaneously. Different membrane designs have been studied to obtain the improved performance for oxygen permeation, typically planar and tubular designs. Among these membrane configurations, micro-tubular type of membranes has demonstrated some advantageous characteristics, such as high surface to volume ratio, short sealing length, dynamic/transient thermal stability. Nonetheless, it is usually very difficult to fabricate micro-tubular membranes, especially for miniaturization designs where the diameters of micro-tubular membranes may reach millimeter or sub-millimeter scales. In the past few years, the fabrication of hollow fiber membranes has been demonstrated using the phase inversion-based spinning process. However, the small diameter of hollow fibers together with the brittleness of ceramic materials usually leads to insufficient mechanical strength for robust and durable operations particularly under harsh thermal cycling conditions. The insufficient mechanical strength also prevents conventional hollow fiber membranes from upscaling into hollow fiber membrane stacks and modules for industrial application.

The first goal of this dissertation is to develop a novel composite hollow fiber-supported thin film membrane. The sintering behaviors and TECs of a set of metal oxides were systematically measured in a wide range of temperatures. The results were used to guide material selection for hollow fiber substrate. The composite hollow fiber substrate precursor was then fabricated using slurry spinning process in combination with modified phase inversion method. The thin film separation layer and catalyst layer were then successfully fabricated on the composite substrate, forming an asymmetric hollow fiber substrate-supported thin film membrane device. Oxygen permeation test of the device was systematically conducted, and the fundamental mechanisms were analyzed. An accelerated long-term stability test of the membrane was also conducted (~ 550 h, ~ 46 thermal cycles), demonstrating excellent robustness and durability. The device was characterized and analyzed before and after the test.

Built upon the successful fabrication and testing of the asymmetric hollow fiber substrate-supported thin film membrane device, the second goal of the dissertation is to upscaling the single hollow fiber membrane technology for membrane stack and module development. In particular, the study elucidated the design of hollow fiber membrane stack, developed a novel reliable gas-tight high temperature sealing technology, and implemented the assembly of hollow fiber membrane stack. Using the upscaling approach, two membrane stacks with a slightly different materials systems were developed. Oxygen permeation performance of the stacks was systematically measured and compared with a single hollow fiber membrane. The fundamental mechanism was discussed. Accelerated long-term stability tests were also conducted to demonstrate the robustness and reliability of the hollow fiber stacks.

The third goal of the dissertation is to advance solid oxide fuel cells (SOFCs) using the developed hollow fiber membrane technology. SOFCs are fuel flexible that can use not only hydrogen but also hydrocarbon fuels and even carbon. Direct hydrocarbon fueled SOFCs may provide advantages of eliminating external reforming components for SOFC system and using the existing infrastructures for the production, storage and delivery of hydrocarbon fuels. These would improve system efficiency, reduce system cost, and facilitate practical applications of SOFC technologies. However, high catalytic activity of Ni can also lead to directly cracking of hydrocarbon compounds at high temperatures and CO hydrogenation as well as Boudouard reaction, causing carbon deposition in the anode. The carbon deposition in turn will deactivate active reaction sites, restrict gas flow, and damage microstructures, overall leading to severe degradations in anode performance and long-term stability. In this chapter, a synergic strategy was studied to design stable anode electrode by combining advantages of hollow fibers and materials. Comprehensive electrochemical performance and short-term stability test demonstrated excellent stability of the novel anode in direct methane fuels. The fundamental reaction mechanisms for the prevention of carbon deposition with the novel cell are elaborated.

TABLE OF CONTENTS

LIST OF TABLES

LIST OF FIGURES

CHAPTER 1

INTRODUCTION

1.1 Oxygen separation membrane

Production of oxygen from air separation has attracted great attention because of its various applications such as glass making, semiconductor manufacturing industry, food processing, petrochemical industry, metal manufacturing industry (e.g., copper and steel production), cutting and welding, combustion processes for hydrocarbon fuels, biological water purification, clean waste incineration and even for patients with chronic lung diseases [1-4]. Furthermore, it is very important when pure oxygen is applied in power plants instead of air. The carbon dioxide is generated from the combustion process as the emission gas, and this can be gradually collected for other industrial utilization and/or further sequestration. This can prevent the direct release of emission gas as a greenhouse gas to the environment, so it is environment friendly and highly efficient. This area will greatly expand because of demand of oxygen as a feed for all large-scale clean energy technologies. Thus, the separation of oxygen from air is important technology. Oxygen is the reactant in clean coal energy delivery in oxy-fuel coal combustion process. High concentration CO_2 flux gas is generated from burnt out of coal with a stream containing O_2 and CO_2. And it can be easily transported and stored to prevent the emission of greenhouse gases.

Oxygen separation is produced mainly by a cryogenic process or pressure swing adsorption. However, cryogenic process operates at very low temperature as -185℃ and at high pressure, so the system is very complex, expensive and energy intensive, while pressure swing adsorption can only generate less than 95% of purity oxygen [5, 6].

Dense ceramic membrane with mixed ionic and electronic conductivity (MIEC) is gaining considerable attention because it is more economically feasible technique for high-purity oxygen production and electrocatalytic reactors for hydrocarbon oxidation via air separation [7-11]. For oxygen separation, the dense ceramic membranes exhibit important advantages over cryogenic and swing adsorption. Unlikely to these two processes, the dense ceramic membrane can generate high-purity oxygen and the production of oxygen is continuous. Oxygen permeation through the dense ceramic membranes is surface exchange and bulk diffusion processes. First, gaseous oxygen transfer and adsorbs on the membrane surface. Oxygen molecules combine with electrons from permeate side are reduced to oxygen ions at the air feeding side. Then the oxygen ions migrate via oxygen vacancies in the dense membrane to the permeate side, where the oxygen ions release electrons and evolve into molecular oxygen. The released electrons then transfer back to the air feeding side through the dense membrane to compensate the ion flux. The lattice oxygen evolves into molecular oxygen, desorbs from the membrane surface, and oxidized to gaseous form in a reverse reaction of the first step. These processes could keep running as long as different oxygen partial pressures exist across the membrane at elevated temperatures. Due to such transport mechanisms, the oxygen selectivity of MIEC ceramic membranes may theoretically reach 100% under the gas-tight conditions, and the production of oxygen is continuous. Fig.1.1 [12] is the schematic of oxygen permeation across the MIEC membranes. The whole process can be denoted in Koreger-Vink notation [7]:

(1) $O_{2,g} \leftrightarrow O_{2,ad}$

(2) $O_{2,ad} \leftrightarrow 2O_{ad}$ $O_{ad} + 2e' + V_O^{\cdot\cdot} \rightarrow O_O^{\times}$

(3) $O_O^X(P'_{O_2}) \rightarrow O_O^X(P''_{O_2})$

(4) $O_O^{\times} \longrightarrow O_{ad} + 2e' + V_O^{\cdot\cdot}$ $2O_{ad} \leftrightarrow O_{2,ad}$

(5) $O_{2,ad} \leftrightarrow O_{2,g}$

The process is controlled by the oxygen surface exchange of first and last steps, bulk diffusion in the middle steps. When the oxygen transportation is considered as the only rate limiting step, Wagner equation is used to calculate the oxygen permeation flux [13].

$$J_{O_2} = -\frac{1}{16F^2} \cdot \frac{\sigma_i \cdot \sigma_e}{\sigma_i + \sigma_e} \cdot \nabla\mu_{O_2}$$

F is Faraday constant, σ_i, σ_e indicates conductivity of oxygen ions and electrons and $\frac{\sigma_i \cdot \sigma_e}{\sigma_i + \sigma_e}$ is ambipolar conductivity. $\nabla\mu_{O_2}$ means the chemical potential gradient of oxygen and can be described as below.

$$\nabla\mu_{O_2} = RT \cdot \frac{\partial lnP_{O_2}}{\partial x}$$

R is the gas constant and T is temperature, and *x* is the distance along the membrane thickness.

According to the Wagner Equation, the properties of materials such as conductivity and operating conditions such as temperature, partial pressure difference across the membrane would determine the oxygen permeation flux. It is obvious to see the thinner membrane permeate more oxygen under the same operating conditions. However, the Wagner Equation is only applied when the bulk diffusion process dominates, thus when the oxygen surface exchange is the rate limiting step, characteristic membrane thickness L_c can be induced, so the exchange and diffusion rates are comparable [13]. Therefore, to develop oxygen permeation membrane with high performance, high ambipolar conductivity of materials, decrease the dense membrane thickness, and improve the surface exchange rate should be considered.

1.2. Solid oxide fuel cell (SOFC)

Fuel cell is an energy device that converts the chemical energy from a fuel into electricity through electrochemical reaction. Fuel cell is different from batteries in requiring a continuous source of fuel and oxygen or air to sustain the chemical reaction, whereas in a battery the chemicals present in the battery react with each other to generate an electromotive force (EMF). The fuel cell can generate electricity as long as the fuels are supplied [14-15]. Compared to the conventional combustion-based heat engine, fuel cell directly converts the chemical energy into electricity while heat engine converts chemical energy to thermal energy first, and then to mechanical energy following by the final conversion to the electrical energy. This feature in fuel cells gives several advantages compared to the internal combustion-based energy generation technology.

The direct conversion of the chemical energy to electricity significantly increases the efficiency. Additionally, combustion-based energy generation technologies cause severe environmental problems such as, climate change, ozone layer depletion, acid rains [16].

However, there are no undesirable products from the fuel cells such as NO_x, SO_x and other pollutants [17]. Furthermore, the combustion-based technologies extremely depend on the fossil fuels which are finite in world supplies, in the meantime, fuel cells use renewable source carriers (i.e., hydrogen). Thus, fuel cell is cleaner, eco-friendly, more efficient energy conversion device. A single fuel cell consists of two porous electrodes (anode and cathode) and dense electrolyte which separate the two electrodes (shown in

Figure 1.2 [17]). It generates electricity directly from the electrochemical reaction of fuels with electrons because of its movement from high-energy reactant bonds to low-energy product bonds [17]. The fuel oxidation reaction is divided by two electrochemical reactions:

$O_2+4e^-\rightarrow 2O^{2-}$ (1.1)

$2H_2+2O^{2-}\rightarrow 2H_2O+4e^-$ (1.2)

At the cathode, the oxygen molecules in the oxidant (air, O_2) absorbed and reduced to oxygen ions with the aid of electrons in the cathode. These resulting oxygen ions flow through the dense electrolyte to the anode side. At the anode, oxygen ions oxidized the hydrogen fuel and released the electrons to the external circuit. The net result of the two reactions is that fuel is consumed and generated water, and an electric current is created which can be used to power electrical devices normally referred to as the load. The electrolyte only allows ions or charged atoms to pass through, therefore, the electrons are forced to flow through an external circuit and do work.

Solid oxide fuel cell (SOFC) is attributed to the solid oxide ceramic electrolyte. It is an all-solid state energy conversion device that converts the chemical energy from fuel to electricity by way of the electrochemical reaction [14]. The usage of ceramic material as the electrolyte exhibits high stability and corrosion resistance and make various configuration cell designs with good performance. Due to the requirement of ionic conductivity for the solid ceramic electrolyte, SOFC operates at 500-800°C [18-21]. The high operation temperature has advantages of rapid electrode reaction kinetics, reducing electrode polarization and increasing the efficiency of the energy conversion reaction.

Furthermore, various kinds of fuels can be electrochemically oxidized at the high temperature such as hydrocarbon fuels which is economical fuels. Direct hydrocarbon fueled SOFCs may provide advantages of eliminating external reforming components for SOFC system and using the existing infrastructures for the production, storage and delivery of hydrocarbon fuels [22-24]. These would improve system efficiency, reduce system cost, and facilitate practical applications of SOFC technologies. Among various geometric SOFC designs, planar and tubular are most widely investigated one. Planar SOFC have low in-plane ohmic resistance, thus it offers high volumetric and gravimetric power density. Mass-production of planar SOFC can be fabricated by tape-casting and spraying method at low cost. However, planar single cells require gas sealing at the edges for high temperature. Crack of the cell functional layer could be occurred result of the compressive sealing and leads to risking the performance stability. The large sealing area of the planar SOFC makes this design less favorable. The tubular SOFC shows the advantages of high mechanical strength and reduced sealing area. Concerning long term stability, the tubular SOFC shows important advantage in performance stability. Additionally, it is easier to connect between single cells in tubular SOFC and simple integration of the high temperature heat exchanger, favoring the tubular design assembling of the cell stack.

The power density of tubular SOFC depends on the inverse of cell diameter which leads to the research of diameter on the scale of millimeters [25]. The small diameter tubular single cells have larger active area within the same volume, increasing the volumetric power density.

Anode supported cell is the most widely investigated and well developed. Ni-containing anode supported cell is considered as the representative due to the high electronic conductivity and great electrocatalytic property of nickel in supporting layer. As a result, the polarization losses of the single cells are significantly reduced and this cell structure display higher performance. Using a thin electrolyte in this design greatly reduces ohmic loss, which enables lower operating temperature and higher performance.

However, using nickel in the supporting layer gives rise to the stability problem especially in hydrocarbon fuels. As well known, nickel is an excellent catalyst for cracking of hydrocarbon fuels and carbon deposition occurs rapidly on the nickel phase when hydrocarbon fuels are directly used (Equation 1.3) [24].

$CH_4\,(Ni) \rightarrow C\,(Ni) + 2H_2$ (1.3)

As a results, volume expansion of the anode supporting layer have been reported [26-27] This irreversible volume expansion of the supporting layer leads to the weak mechanical strength and formation of cracks, resulting in poor performance and even further failure of the cells. Significant efforts have been made to modify Ni-cermet anode to improve their resistant property for carbon deposition. Carbon resistant metals and oxides such as Cu, Sn, Ag and their derivates have been investigated as the surface modification and alloying with Ni-Cermet [28-30]. In spite of these modifications, carbon deposition is inevitable issue for Ni-based anodes because of the Ni-catalytic cracking of hydrocarbon fuels. To overcome the use of Ni-based anode, efforts have been made to develop Ni-free anode materials. A class of perovskite and layered perovskite type of mixed ionic and electronic conducting oxides, such as $La_{0.75}Sr_{0.25}Cr_{0.5}Mn_{0.5}O_3$, La_{1-}

$_xSr_xTiO_3$ and their derivatives were investigated [31-33]. Even though these materials exhibited good property for carbon deposition resistance, however, the power densities of corresponding SOFCs are usually much lower than Ni-cermet anodes. In this respect, Ni-cermet is still favored anode material due to its high electronic conductivity and electrocatlytic properties [34]. Cerium oxide can release and uptake oxygen by the following chemical reaction [35]:

$$CeO_2 \rightarrow CeO_{2-x} + (x/2)O_2 \quad (1.4)$$

The characteristic of oxygen storage capacity could be used to catalyze the electrochemical oxidation of hydrocarbon fuels. Using Ni-cerium oxide cermet is a feasible way to internally convert the hydrocarbon to hydrogen via the partial oxidation reaction (Equation 1.5) [36].

$$CH_4(CeO_2) + H_2O \rightarrow CO + 3H_2 \quad (1.5)$$

Additionally, when aliovalent ions (divalent or tetravalent cations) are doped into ceria lattice, oxygen vacancies are created by charge compensation mechanism, further improving oxygen storage capacity and catalytic property of ceria.

1.3 Preparation of ceramic hollow fiber membranes

1.3.1 Ceramic hollow fiber membranes

While the traditional design for membrane and solid oxide fuel cell, either tubular or disk configuration, has shown disadvantages in usage efficiency because of low area/volume ratio (30-250 m^2/m^3) and this leading to the limiting their industrial application [37, 38]. Ceramic hollow fibers can be considered as alternative solution due to its higher packing density, higher area/volume ratio (~3000 m^2/m^3) [39]. The configuration is less than 2mm of outer diameter and the membrane layer is coated on the surface of a porous fiber supporter. As shown in Figure 1.3 [39], these fibers subsequently will be packed together and sealed the ends before placing in a shell.

Hollow fiber membranes are first developed in the 1960s for reverse osmosis application and they are commonly produced using various polymers [40]. Unlike polymeric hollow fibers the ceramic hollow fiber membranes demonstrate excellent performance even operated under harsh conditions such as high temperature, high pressure or in organic solvents, acidic/basic solutions, oxidative/reductive conditions [41-43].

The mostly used technique to fabricate hollow fiber nowadays is phase inversion because of its simplicity compared to traditional extrusion process. Phase inversion is a demixing process in which initially homogeneous polymer solution is transformed from a liquid state to a solid state in a controlled manner. There are several ways to achieve the transformation: Thermally induced phase separation, evaporation induced phase separation, vapor induced phase separation, and immersion precipitation [44, 45]. Among these, the immersion precipitation is the most commonly used method. It can be explained by a ternary phase diagram in Figure 1.4 [46]. After immersing the polymer solution in coagulation bath (nonsolvent, mostly water), the exchange of solvent and nonsolvent makes the solution composition changes dramatically. The homogeneous solution moves from stable one phase region to two phase metastable region and starts to precipitate when reach the miscibility gap (Point B). Then the solution separates into a polymer-poor phase and polymer-rice phase. The polymer-rich phase starts to solidify at point C and finish at point D in the end. Different separation rates contribute to the final asymmetric structure. Delayed demix which means slow exchange rate favoring form a dense skin layer with a sponge like sublayer. While instantaneous demix which indicates fast solvent-nonsolvent exchange prefer forming a porous skin layer with a finger-like sublayer [46, 47].

Ceramic hollow fiber membranes usually employ a combined phase inversion-sintering technique. And the polymers serve as a binder to hold ceramic particles together instead of acting as the functional materials in ceramic hollow fiber membranes. Thus, the fabrication of ceramic hollow fiber membrane is more complicated, and its microstructures is controlled by many factors, spinning suspension, spinning of hollow fiber precursors, and high temperature sintering. For the spinning suspension, ceramic powder particle size and distribution, concentration of ceramic powder, and additives should be considered [48, 49]. Small particles move to interface faster than bigger particles, a layered structure will be formed. Moreover, smaller particles are easy to sinter and densify at high temperature. The higher concentration of ceramic powders which is solid content, the more viscous of the solution lead to slower exchange rate, thus thicker and denser membrane. On the contrary, higher concentration of solvent leads to the solution less viscous which is good for the finger-like channels formation. Additives used to control the viscosity of the solution. Some organic additives could let the ceramic powders disperse well in the solution to improve its uniformity, and some mineral additives can promote the following sintering behavior of the membranes.

Secondly, spinning of hollow fiber precursors. There are 4 parameters directly affect the microstructures of nascent hollow biers. (1) Extrusion rate of suspension: slow extrusion rate can reduce the finger-like voids formation which is good for dense membrane while faster extrusion is applied for finger-like channels. (2) Internal coagulant type and its flow rate: the influence of flow rates is similar to those of spinning rates of suspension when water is using as internal coagulant. When NMP or NMP/H2O mixer is used, either delay the coagulation of polymers, thus promoting the extension of finger-like channels from outside or delay the demix rates and inhibits the growth of finger-like voids inside depending on the concentration of mixer. (3) Bath temperature: the finger-like channels will be facilitated at a higher bath temperature due to enhanced exchange rates at higher temperature. (4) Spinneret structure: the inner and outer diameter of the spinneret, and flow angle of suspension are needed to be considered [50-56].

Lastly, sintering temperature, heating and cooling rates, dwelling time are important factors in affecting the performance of the fabricated membrane. Sponge-like layers usually densify during the high temperature sintering, while finger-like voids still could remain the shape even after sintering at elevated temperatures.

1.4 Objectives

Great efforts have been dedicated in finding materials to satisfy all the requirements that not only have perfect performance but also excellent chemical and mechanical strength. However, currently developed materials with exceptionally high performance generally degrade quickly. Fabricating novel and favorable microstructure, especially utilizing ceramic hollow fibers featuring radially well aligned microchannels open at inner surface, seems to be a critical solution for scaling up and practical applications.

In chapter 2, LSCF-ZnO composite hollow fiber substrate supported asymmetric oxygen permeation membrane for long-term operation under harsh thermal conditions is fabricated and optimized. In chapter 3,4, scaling-up and the sealing method of the LSCF-ZnO composite substrate supported membrane into a stack was presented and evaluated the oxygen permeation flux and the long-term stability of the stack.

In chapter 5, two strategies were adopted as synergy effects to improve SOFC single cell stability in methane fuel. One strategy is using microchannel-structured inert YSZ supporter as diffusion barrier. The other strategy is doping zirconia into the Ni-samarium doped ceria cermet anode to improve oxygen storage capacity and catalytic property of ceria.

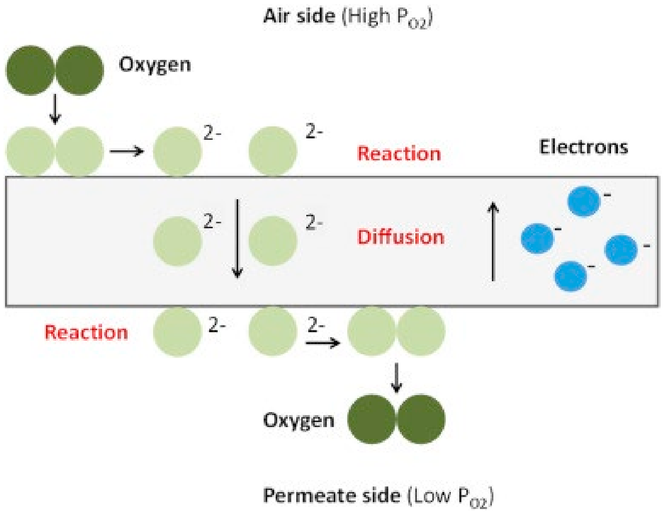

Figure 1.1 Schematic of the oxygen transport mechanism in a mixed ionic-electronic conducting membrane [12].

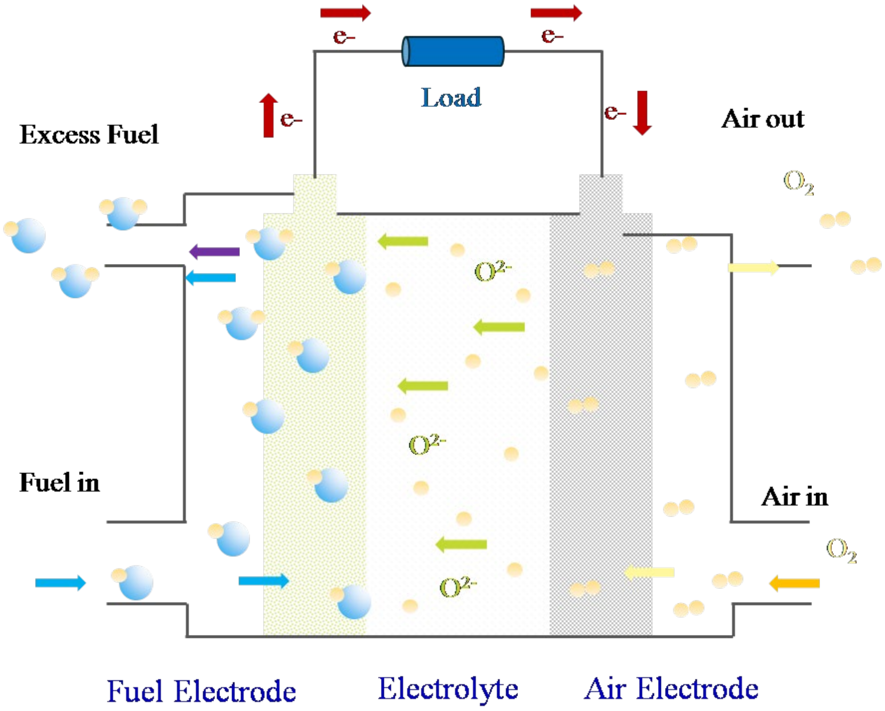

Figure 1.2. Schematic of the solid oxide fuel cell [17].

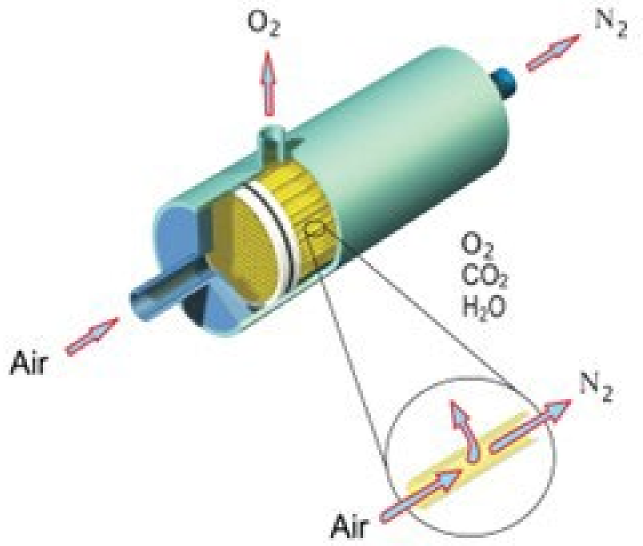

Figure 1.3 Schematic of a hollow fiber bundle used to separate oxygen, carbon dioxide, and water from air [39].

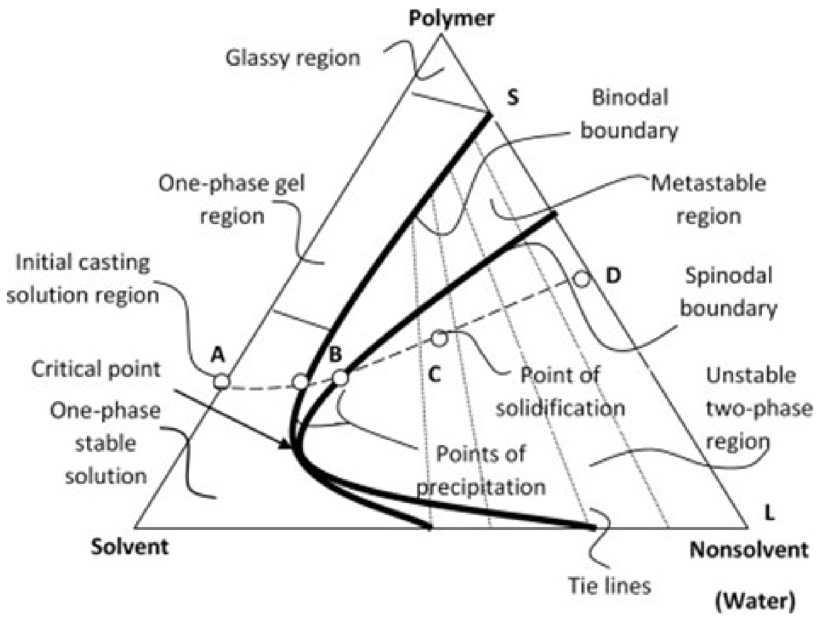

Figure 1.4 Schematic representation of the three-component phase diagram describing the formation of water-precipitation phase separation membranes [46].

CHAPTER 2

FABRICATION AND ACCELERATED LONG-TERM STABILITY TEST OF ASYMMETRICAL HOLLOW FIBER-SUPPORTED THIN FILM OXYGEN SEPARATION MEMBRANE

2.1 Introduction

Air separation is a widely used process for oxygen production. Several separation technologies have been developed for air separation, including cryogenic distillation, swing adsorption, redox process of metal oxides, and electrochemical process [2,4, 57-58]. Among these technologies, electrochemical permeation process stands out as a cost-effective and simple process for pure oxygen production from air [7, 10]. The electrochemical permeation process employs a gas-tight membrane to permeate and separate oxygen from air directly, where the membrane conducts both ions and electrons simultaneously. Very complicated multiphysics transports are involved in oxygen permeation process. Briefly, at feed side, oxygen reduction reaction (ORR) takes place, reducing the surface adsorbed oxygen molecules into ions by incorporating electrons from oxygen lean (permeate) side. The generated oxygen ions then transport to the permeate side through oxygen vacancies in the gas-tight membrane. At the permeate side, oxygen evolution reaction (OER) arises, producing oxygen molecules and electrons. The generated electrons transport back to the feed side through the dense membrane, remaining pure oxygen gas at the permeate side. The ORR/OER are catalyzed by the materials at feed/permeate surface respectively, while the process is driven by chemical potentials induced by oxygen partial pressure across the membrane. Different membrane designs have been studied to obtain the improved performance for oxygen permeation, typically planar and tubular designs. Among these membrane configurations, micro-tubular type of membranes has demonstrated some advantageous characteristics, such as high surface to volume ratio, short sealing length, dynamic/transient thermal stability. Nonetheless, it is usually very difficult to fabricate micro-tubular membranes, especially for miniaturization designs where the diameters of micro-tubular membranes may reach millimeter or sub-millimeter scales. In the past few years, the fabrication of hollow fiber membranes has been well demonstrated using the phase inversion-based spinning process [54, 59-61]. Built upon the fabrication of basic hollow fiber membranes, a few strategies have also been studied to improve membrane performance and stability, including ultrathin hollow fiber membrane [62, 63], hollow fiber with surface catalyst [64], dual phase hollow fiber membrane [65]. Recently, the solid oxide fuel cell structure with short-circuit strategy was employed to separate oxygen while enhancing stability [66].

The fabrication of traditional hollow fiber membrane involves several steps, including slurry preparation, slurry spinning and phase inversion process to obtain hollow fiber precursor, followed by one-step high temperature sintering to obtain gas-tight sample. Because of the requirement for conducting both ions and electrons, the materials used for membranes are either mixed ionic and electronic conductors (MIECs) or the composite of ionic and electronic conductors. These materials are generally rare earth metal oxides.

Even though the membrane can be well sintered, its mechanical strength is usually not sufficient for robust and durable operations particularly under harsh thermal cycling conditions. The insufficient mechanical strength also prevents conventional hollow fiber membranes from assembling into membrane stack. Consequently, alternative strategies for stack assembly are employed to mitigate the issue induced by insufficient mechanical strength of hollow fibers [67-71]. For example, the hollow fibers are bundled together using LSCF slurry to improve the mechanical strength while obtaining stack functionality [72-74], or a dead-end design of single hollow fiber membrane is used so that mechanical loads on individual hollow fibers can be avoided in a stack assembly [75, 76]. However, these stack assembly strategies would lose advantages brought by unique features of hollow fiber membranes, such as very highly effective surface area for ORR/OER, facile gas transport. To essentially overcome these issues, it is necessary to improve mechanical strength of individual hollow fiber membranes. One potential method is to use composite materials for hollow fibers. For instance, suitable metal oxide, particularly simple oxides, can be mixed with MIEC to form a composite membrane for this purpose. However, the addition of simple metal oxide may decrease the effective conductivity of the membrane for charge transport. Recently, our group has developed a substrate-supported thin film asymmetrical hollow fiber membrane, where a hollow fiber substrate is used to support a thin film gas-tight permeation layer [77]. As a result, material for the substrate can be different from the permeation layer. This design strategy may overcome the above issue, where the composite material is used for the substrate without affecting the conductivity of the permeation layer. However, this design could also induce issues for reliable fabrication of the membrane device. Typically, the sintering behavior and thermal expansion coefficient (TEC) of the substrate are different from the permeation layer. It is critical to be able to identify the materials with compatible sintering behavior and TECs for reliable fabrication and operation of the membrane.

In this research, a composite hollow fiber-supported thin film membrane was studied. The composite of LSCF-simple oxide was used as a model material system to demonstrate the membrane fabrication. The sintering behaviors of a set of simple oxides were measured and evaluated in a wide range of operating temperatures. The ZnO was singled out as a material component for the composite hollow fiber substrate LSCF-ZnO.

The sintering behavior of composite green hollow fibers with different LSCF-ZnO ratios was characterized and compared with LSCF green hollow fiber. The TECs of ZnO and LSCF as well as the composites with different LSCF-ZnO ratios were systematically measured. The composite hollow fiber with the sintering behavior and TEC close to those of LSCF was used as the substrate to fabricate substrate-supported thin film LSCF. A thin, porous catalyst layer $PrBaCo(Fe_{0.6}Zr_{0.2}Y_{0.2})O_{5+\delta}$ (PBCFZY) was then dip-coated on the dense LSCF layer, forming an asymmetrical membrane device. The performance of the membrane was systematically measured under different operating conditions. An accelerated long-term stability test was conducted to evaluate the durability and robustness of the membrane. The microstructure of the membrane device was characterized before and after the tests.

2.2 Experimental

2.2.1 Sintering behavior and TEC of metallic oxides and composites of metallic oxide and LSCF

The sintering behaviors of Alumina powders (α-Al_2O_3, ultra-pure grade, Inframat Advanced Materials, USA), Zinc oxide powders (ZnO, 200 Mesh, Alfa Aesar, USA), magnesium oxide powders (MgO, Alfa Aesar, USA), zirconium oxide powders (ZrO_2, Spectrum, USA), and titanium oxide powders (TiO_2, 22 Mesh, Alfa Aesar, USA) were measured. Specifically, alumina powders were mixed with 2 wt.% polyvinyl butyral (PVB, Butvar B-98, Spectrum, USA) and then pressed at 300 MPa to form pellets using a stainless-steel die facilitated by a hydraulic equipment. ZnO, MgO, ZrO_2, TiO_2 pellets were obtained in the same way. The green pellet was loaded into a dilatometer system (DIL 402 PC, Netzsch, Germany). The temperature of the pellet was increased from room temperature to 1350 °C with a heating rate of 5 °C min^{-1}. The time history of corresponding thickness change of the pellet was measured and recorded.

The thermal expansion coefficient (TEC) of ZnO, LSCF (Fuel cell materials, USA) and LSCF-ZnO composites with different weight ratios were measured. For this purpose, 2 g of ZnO powders was pressed to form a rectangular bar using a stainless-steel die with a pressure applied by a hydraulic equipment. The formed ZnO bar was sintered at 1300 °C in air for 6 h. The LSCF bar was obtained in the same way. For LSCF-ZnO composites, two compositions were considered, including 50 wt.% ZnO mixed with 50 wt.% LSCF (simply denoted as LSCF-ZnO5050) and 25 wt.% ZnO mixed with 75 wt.% LSCF (simply denoted as LSCF-ZnO7525). The composite ZnO and LSCF powders were mixed, followed by ball-milling in ethanol for 48 h to form uniform composite powders.

After drying, the composite powders were pressed to form rectangular bars followed by sintering in air at 1300 °C for 6 h to obtain LSCF-ZnO5050 and LSCF-ZnO7525 sample bars respectively. The sintered sample bars were then loaded into a dilatometer system (DIL 402 PC, Netzsch, Germany). The sample thermal expansion was measured from room temperature to 1300 °C. The TECs of the corresponding materials were then calculated using the thermal expansion curves.

2.2.2 Fabrication of asymmetric hollow fiber membrane and sintering behavior measurement

To fabricate hollow fiber substrate, the substrate slurry was first prepared. Specifically, the 5.21 wt.% polyether sulfone (PESF, Veradel 3000P, Solvay Specialty Polymers, USA) and 0.74 wt.% polyvinylpyrrolidone (PVP, K30, CP, Sinopharm Chemical Reagent Co., China) were dissolved in 26.05 wt.% N-methyl-2-pyrrolidone (NMP, HPLC grade, Sigma Aldrich, USA). After ball-milling for 2 h, an organic solvent was obtained. The as-prepared LSCF-ZnO7525 composite powders with 68 wt.% were mixed with the prepared organic solvent, followed by ball-milling for 48 hours to form a homogeneous LSCF-ZnO7525 slurry. The bubbles in the as-prepared slurry were removed by a vacuum pump system. The deaired slurry was then loaded into the chamber of a stainless-steel spinneret apparatus. The details of the slurry spinneret apparatus were published elsewhere [77]. The flow of the mixture coagulant with 95 vol. % NMP and 5 vol. % tap water was connected to the central spinneret orifice while the slurry was connected to the ring-type orifice surrounding the central orifice. A pressurized nitrogen gas system was used to drive the flows of both central coagulant and slurry through the spinneret orifices. The in-house built slurry spinning system and operating parameters were detailed elsewhere [77, 78]. Upon immersing into the water bath, phase-inversion process took place on the surface of the extruded slurry, forming hollow fiber precursor.

The difference of NMP solvent concentrations at inner and outer surfaces driven the formation of radially well-aligned microchannels, open at the inside of hollow fiber precursor. The hollow finer precursor was immersed in water for at least 48 hours, fully completing the exchange process. The hollow fiber precursor was then dried in air at room temperature and cut into desired length for further heat treatment and functional layer fabrication. The LSCF-ZnO5050 composite hollow fiber and LSCF hollow fiber were obtained using the same fabrication process. And sample shrinkage was measured from room temperature to 1200 ºC using a dilatometer.

To fabricate thin film LSCF dense separation layer on hollow fiber substrate, LSCF solution was first prepared. Specifically, LSCF powders (5.4 wt.%) were mixed with ferro binder B73210 (Ferro, USA; 4.1 wt.%) and α-terpineol (TCI, Japan; 5.4 wt.%) in ethanol (Decon Labs, Inc., USA; 85.1 wt.%), followed by ball-milling to form LSCF solution. The LSCF solution was then dip-coated onto the green substrate. The coated samples were sintered at 1270 °C in air for 6 h to densify the LSCF coating layer while bonding the coating layer and substrate together, forming the membrane device LSCF-ZnO7525 substrate/dense thin film LSCF.

For the fabrication of PBCFZY catalytic layer, PBCFZY powders were first synthesized using citric acid – nitrate combustion method. Briefly, stoichiometric amounts of Pr_6O_{11} (99.99%, Alfa Aesar, USA), BaN_2O_6 (99%, Acros Organics, USA), $Co(NO_3)_3 \cdot 6H_2O$ (97.7%, Alfa Aesar, USA), $Fe(NO_3)_3 \cdot 9H_2O$ (98.0-101.0%, Alfa Aesar, USA), Zirconyl nitrate solution (99%, Sigma Aldrich, USA), and Y_2O_3 (99.9%, Acros Organics, USA) were dissolved in a dilute nitric acid solution. After magnetic stirring, a transparent solution was formed. Citric acid (99.0-102.0%, BDH, UK) and ethylenediaminetetraacetic acid (EDTA, 99.4-100.6%, BDH, UK) with molar ratio of citric acid: EDTA: metal ions = 1.5: 1: 1 as complexants were mixed with the transparent solution. Ammonia was dropped into the solution to adjust its pH value close to 8. The homogenous solution was evaporated on a hot plate at 80 ºC, forming a viscous gel, followed by self-igniting. The complete combustion of the gel led to ash-like material.

The ash-like material was then ground in ethanol using high-energy ball-milling equipment. After drying, the powders were clacinated at 1000 ºC in air for 6 h to form PBCFZY phase. With the prepared PBCFZY powders, thin film PBCFZY porous catalytic layer was further fabricated on the dense LSCF layer. Briefly, PBCFZY powders (10.25 wt.%) was mixed with ferro binder B73210 (3.85 wt.%) and α-terpineol (5.13 wt.%) in ethanol (80.77 wt.%). The mixture was ball-milled for 48h to form PBCFZY solution. The PBCFZY solution was then dip-coated onto the dense LSCF layer, followed by firing at 1000 °C in air for 3h, forming asymmetric hollow fiber membrane device of LSCF-ZnO7525 substrate/dense LSCF/porous PBCFZY.

2.2.3 Performance measurement and characterization

The gas tightness test of the fabricated hollow fiber membranes was conducted at room temperature before the performance test. Specifically, the hollow fiber sample was sealed at one end by epoxy resin while being connected to the pressured nitrogen gas at the other end. The membrane sample was immersed into water while a pressure of up to 2 bar was applied to the nitrogen gas. The bubbles on the membrane surface were used to identify its gas-tightness.

For oxygen permeation measurement, alumina tubes were used to support 50 mm hollow fiber membrane. The conductive adhesive ink (DAD-87, Shanghai Research Institute for Synthetic Resins, China) was first used to seal the connecting part, followed by aging at 900 °C in air for 30 min. The ceramic paste (Aremco Products Inc., USA) was then applied on the surface sealing part of the adhesive ink. After drying, alumina tube/hollow fiber membrane/alumina tube assembly was heat-treated at 950 °C in air for 30 min to bond the sealing part. During oxygen permeation test, argon sweep gas was supplied into the lumen side of the hollow fiber membrane while the shell side was exposed to ambient air. The operating temperature of the membrane was controlled by a high temperature tube furnace. The effluent gas from the hollow fiber membrane was sampled by a 5Å molecular sieve column and the concentrations of sampled gas species were analyzed using an online gas chromatography (GC-8A, Shimadzu, Japan).

Microstructures of hollow fiber membrane samples were characterized by scanning electron microscopy (SEM, Zeiss Gemini500 FESEM, Germany). The spatial distribution of elements was analyzed using energy-dispersive X-ray spectroscopy (EDS) mapping technology.

2.3 Results and Discussion

Fig.2.1a shows the sintering behaviors of typical simple metallic oxides MgO, ZrO_2, Al_2O_3, TiO_2, and ZnO. It is easy to see that ZnO started to sinter around 600 ºC and kept sintering until the specified maximum temperature of 1300 ºC. The V-type curve of sintering rate can be observed for ZnO in Fig.2.1b, where the magnitude of ZnO sintering rate increased with sintering temperature from 600 to 900 ºC. Beyond 900 ºC, the magnitude of the sintering rate decreased with increasing sintering temperatures. At the beginning of ZnO sintering stage, the neighboring ZnO particles in the bulk start to connecting and necking, and ZnO particles coalesce and grow, leading to porosity decrease and shrinkage of bulk volume. On the other hand, with increasing sintering temperatures, the volume of the bulk increases due to thermal expansion. The sintering rate is induced by the combinational effects of sintering and thermal expansion. Between 600 and 900 °C, the sintering effect could be much stronger than the thermal expansion effect, leading to the increasing shrinkage rate of the bulk with the temperature. Beyond 900 °C, the sintering effect could become weaker than the thermal expansion effect, yielding the deceasing shrinkage rate. The rest of the materials demonstrates that the temperature initiating the sintering process is higher than ZnO, and none of these demonstrates V-type sintering rate curve. In particular, TiO_2 started to sinter around 850 °C and continued the sintering process up to 1300 °C. During this process, the magnitude of its sintering rate kept increasing with the sintering temperature. The temperatures starting to sinter for MgO, ZrO_2, Al_2O_3 are approximately 1250 °C, much higher than those of ZnO and TiO_2. Once the sintering is started, it seems that the sintering rates of ZrO_2, Al_2O_3 are faster than those of MgO and TiO_2. Obviously, ZnO and TiO_2 started to sinter at relatively low temperatures. It has been realized that at least ~10% linear fractional shrinkage of substrate is needed for thin film densification during the sintering of substrate-supported thin film device [79, 80]. As one can see from Fig.2.1a, upon reaching the sintering temperature of about 950 °C, the 10% shrinkage of ZnO substrate was obtained. For TiO_2 bulk, when 10% shrinkage was obtained, the sintering temperature needed to reach up to 1300 °C. Comparing these materials, ZnO is selected as a component of substrate for asymmetric membrane fabrication due to its superior sintering activity.

The addition of ZnO in the substrate leads to the fact that the material of the substrate is different from that of thin film dense separation layer, and thus the sintering activity and TEC mismatch between the two layers. To obtain reliable fabrication, the sintering behaviors and TECs of the substrate and dense separation layer are further measured respectively. For this purpose, the bulk samples were prepared using the identical fabrication process of the substrate as mentioned above. The dilatometer system was used to measure the longitudinal shrinkage of the prepared hollow fiber samples, including LSCF-ZnO5050 composite hollow fiber and LSCF-ZnO7525 composite hollow fiber as well as LSCF hollow fiber. The temperature of the samples was controlled by the furnace of the dilatometer system, increasing from room temperature to 1200 ºC at a heating up rate of 5 °C·min^{-1}. Fig. 2.2a shows the sintering behavior of the samples. From room temperature up to about 280 ºC, the longitudinal lengths of the samples show a slight increase due to thermal expansion of the materials. Around 280 – 300 ºC, a spike shrinkage of the substrate precursors occurred, which was probably induced by the viscous deformation of polymers in the precursors [81]. Beyond 300 ºC, a slightly different sintering behaviors were demonstrated by LSCF, LSCF-ZnO5050, and LSCF-ZnO7525 substrates. In particular, the longitudinal length of LSCF sample increased a little bit between 300 up to 800 ºC probably due to thermal expansion effect. Beyond 800 ºC, LSCF sample started to quickly sinter due to the burning out of polymers and coalesce of ceramic nanoparticles. However, LSCF-ZnO5050 and LSCF-ZnO7525 substrates demonstrated little change of the longitudinal length in 300 – 900 ºC. While thermal expansion effect should increase the longitudinal length of the samples, the sintering effect of ZnO component started to occur around 600 ºC, making the sample shrink. As a result, the thermal expansion effect could be canceled out by the sintering effect. Beyond 900 ºC, the burning out of polymers and coalesce of ceramic nanoparticles play a dominant role, leading to rapid shrinkage of the LSCF-ZnO5050 and LSCF-

ZnO7525 substrates. When the sintering temperature reached 1200 °C, the shrinkage of pure LSCF substrate was a little bit less than 8%, while LSCF-ZnO7525 and LSCF-ZnO5050 substrates obtained 9% shrinkage. This result further confirmed the sintering aid role of ZnO for LSCF component. The sintering rates in Fig. 2.2a are also consistent with the shrinkage of the samples. Around 280 – 300 ºC, a significant sintering rate increase was observed for three samples due to the viscous deformation of polymers in the precursors. Between 300 – 700 ºC, the sintering rates showed little change. Beyond 700 ºC, the sintering rates of the three samples increased with sintering temperature. It can be observed that the sintering rate of LSCF-ZnO7525 was very close to that of LSCF between 700 and 850 ºC. Beyond 850 ºC, the sintering rate of LSCF-ZnO7525 was larger than that of LSCF. However, the sintering rate of LSCF-ZnO5050 was lower than that of LSCF between 700 and 900 ºC, and lower than that of LSCF-ZnO7525 between 700 and 1050 ºC. While both LSCF-ZnO7525 and LSCF-ZnO5050 could be used as the substrate for substrate-supported thin film LSCF fabrication, the sintering behavior of the former with faster sintering rate facilitates to densify thin film LSCF at relatively lower temperatures than the latter with slower sintering rate.

In substrate-supported thin film device, the material of the substrate is usually different from that of the thin film. The TEC mismatch between the substrate and thin film could also affect the reliability of the fabricated device. Therefore, the TECs of the composite substrates and involved material components are systematically measured. Fig. 2.2b shows the thermal expansion curves of LSCF, ZnO, and their composites when the temperature increased from room temperature to 1200 ºC. The TECs of the materials were also obtained by linear curve-fitting and showed in the figure. The ZnO bulk demonstrates a linear thermal expansion curve with TEC of $8.29 \times 10^{-6}\,\mathrm{K}^{-1}$. Interestingly, the LSCF and LSCF-ZnO composites demonstrate bilinear regions of thermal expansion. The interfacial temperature between the two linear regions is around 1000 K. The TEC values of the materials at the temperatures below 1000 K are lower than those above 1000 K. Obviously, the bilinear behavior of the TECs is induced by LSCF phase in the composite. In principle, the oxygen loss from and/or incorporation into LSCF bulk due to defect reaction can be expressed by Kroger-Vink notation,

$$\mathrm{O_O^{\times}} + 2\mathrm{M_M^{\cdot}} \leftrightharpoons \frac{1}{2}\mathrm{O_2(g)} + \mathrm{V_O^{\cdot\cdot}} + 2\mathrm{M_M^{\times}} \qquad (1)$$

where $\mathrm{O_O^{\times}}$ represents lattice oxygen, M the B-site element of Fe or Co, g the gas phase, $\mathrm{V_O^{\cdot\cdot}}$ the oxygen vacancy, the subscript × denotes neutral charge, the subscript · and ·· represent single and double positive charge respectively. To maintain an equilibrium state at relatively high temperatures, e.g., beyond 1000K, more lattice oxygens will be lost from the LSCF bulk, causing thermal induced reduction. As a result, more oxygen vacancies will be created, which in turn leads to the decrease of B-O bond and expansion of $\mathrm{BO_6}$ octahedra. Therefore, such a thermal induced reduction contributes to the faster expansion of LSCF bulk and the composites at high temperatures [82, 83]. It can be observed that the TECs of LSCF-ZnO composites are between that of pure LSCF and pure ZnO bulk. The less content of ZnO in the composite, the closer TEC of the composite to pure LSCF. Since asymmetric membrane with substrate-supported LSCF thin film will be fabricated, LSCF-ZnO7525 composite is selected as substrate material based on the consideration of sintering behavior and TEC match. The prepared LSCF solution was dip-coated onto the green substrate LSCF-ZnO7525, followed by co-sintering at 1270 ºC in air for 6 h, forming a substrate-supported dense thin film membrane device LSCF-ZnO7525/LSCF. The PBCFZY catalytic layer was then fabricated on the dense LSCF layer by dip coating and sintering at 1000 ºC in air for 3 h. Fig. 2.3a shows the cross-sectional SEM image of membrane LSCF-ZnO7525/LSCF/PBCFZY, where multi-layer structure was obtained. It is observed that the microchannels are open at the inner surface and well-aligned in the radial direction of the LSCF-ZnO7525 substrate. Obviously, the microchannels remained very well after high temperature sintering processing, demonstrating their excellent thermal stability. Fig. 3b indicates that ~ 20 μm dense thin film LSCF is intimately in contact with both the substrate and surface porous PBCFZY catalyst layer, and about 10 μm porous PBCFZY catalyst layer is obtained.

The EDS analysis results of the sample cross section are shown in Fig. 2.3c. The Zn element is confined within the substrate region, and La and Sr elements are limited in the regions of both substrate and dense separation layer. The Fe and Co elements spread in the entire cross section with different densities in different regions, e.g., substrate and dense separation layer as well as porous catalytic layer. A relatively high Fe density was observed in both dense separation and substrate regions while low Fe density was in the porous catalytic layer. The distributions of these elements, Zn, La, Sr, Fe, Co, are consistent with the materials and structures of the fabricated membrane device. The element Ba was mainly confined within the porous catalytic layer with a slight scattering in the separation layer and substrate. However, the elements Pr, Zr, and Y distributed everywhere, including not only porous catalytic layer but also separation layer and substrate. This observation is not consistent with the multi-layer design of the membrane device. The PBCFZY catalytic layer was fabricated on the dense separation layer through dip coating and sintering process. On one hand, it is extremely difficult to fully (100%) densify the thin film LSCF separation layer at 1270 ºC, some micro/nano pores might still exist after sintering. On the other hand, the PBCFZY was synthesized using a citric acid – nitrate combustion method, where very fine nano particles were obtained. The solution for dip coating of PBCFZY catalytic layer contained 90% ethanol. During the dip coating process, PBCFZY nanoparticles could be infiltrated into the pores, diffusing into both the separation layer and substrate. The high sintering temperature might also contribute to diffusion of elements of Pr, Ba, Zr, and Y. This could be the reason that the elements of Pr, Ba, Zr, and Y, which were supposed to be confined within the catalytic layer, were observed in the separation layer and substrate. While this phenomenon is worth further studying from device fabrication point of view, it will be shown later that such a side diffusion did not bring obvious detrimental effects on membrane performance and stability.

The fabricated hollow fiber membrane was systematically tested for oxygen permeation from air in the temperature range of 750 – 950 ºC. The shell side of the hollow fiber as the feed side was exposed to ambient air. Argon gas as sweep gas was supplied to the lumen side. Effluent gas from lumen side was analyzed by an online GC. A high temperature test furnace was used to control the membrane temperature during the test. Fig. 2.4 shows the measurement results of LSCF-ZnO7525/LSCF/PBCFZY membrane. For a constant sweep gas flow rate, oxygen permeation flux increased with operating temperature from 750 to 950 ºC, indicating thermally activated nature of oxygen permeation process. At a given operating temperature, oxygen permeation flux increased with sweep gas flow rate, implying that oxygen evolution reaction (OER) and associated transport subprocesses at the permeate side is a limiting subprocess involved in oxygen permeation process. In fact, increasing the flow rate of argon sweep gas will decrease oxygen partial pressure at the permeate side. Since the ambient air is supplied to the feed side, this in turn will increase oxygen partial pressure difference across the membrane. Accordingly, the chemical potential will be increased, enhancing oxygen permeation flux through the membrane. Combining the effects of both operating temperature and argon sweep gas, it is easy to see that the membrane performance was improved more prominently by increasing sweep gas flow rate at higher operating temperatures. The Arrhenius plot derived from Fig. 2.4a is shown in Fig. 2.4b. The activation energy derived from Arrhenius plot (Fig. 2.4b) is shown in Fig. 2.4c.

Obviously, the overall activation energy of oxygen permeation through the membrane asymptotically increased with increasing argon sweep gas flow rate. It is worth noting that the sweep argon gas at the room temperature was supplied to the lumen side of the membrane. This will decrease the temperature of the membrane. The decreased membrane temperature will increase activation energy for oxygen permeation because the oxygen ion transport through oxygen vacancies in the bulk is a thermally- activated process. This could be the reason that activation energy increased with increasing argon sweep gas flow rate. In general, the dense separation layer conducts both electrons and ions. Reducing the thickness of the separation may decrease ohmic resistance for charge transport. Therefore, thin film separation layer is beneficial to improve oxygen permeation flux of membrane devices. To verify this understanding, a few LSCF membranes with different thickness of separation layers are summarized in Table 2.1. Obviously, oxygen permeation flux increases with decreasing the thickness of dense separation layer. Due to different membrane designs, e.g., with/without different surface catalysts, and the membranes were tested under different conditions, e.g., different sweep gases with different flow rates, it is very difficult to perform a comprehensive comparison. However, this simple comparison is sufficient to verify the effectiveness of thin film dense separation layer for performance improvement of membrane devices.

A long-term accelerated stability test was also conducted with the fabricated hollow fiber membrane. The argon sweep gas flow rate was maintained at 50 mL·min^{-1}. The stability test was run about 550 h and the results are shown in Fig. 2.5, where the left vertical axis shows the time history of oxygen permeation flux while the right vertical axis demonstrates that of the applied thermal loads. The sampling time for oxygen permeation flux with an online GC was 1 h during the daytime. At the constant temperature of 850 $^{\circ}$C in the first 190 h, oxygen permeation flux of the membrane was very stable without any obvious degradation. In fact, a slight performance enhancement was obtained probably due to the activation of membrane material system. The constant temperature load was followed by very harsh thermal cycling loads for about 350 h. The thermal cycling loads were composed of three basic cycling patterns. In the first cycling process, the temperature was decreased from 850 to 600 $^{\circ}$C at the cooling down rate of 3 $^{\circ}$C min^{-1}, maintained at 600 $^{\circ}$C for 1 h, increased back to 850 $^{\circ}$C at the heating up rate of 3 $^{\circ}$C min^{-1}, and then maintained at 850 $^{\circ}$C for 1 h. The second and third cycling processes are quite similar to the first one except that the cooling down and heating up rates were 5 $^{\circ}$C min^{-1} and 7 $^{\circ}$C min^{-1}, respectively. The combination of these three basic thermal cycling loads was applied to the membrane during stability test. In particular, the first and the second as well as the third cycling processes were applied consecutively. The first cycling process was repeated for three times, followed by repeating the second cycling process for four times and third cycling process for five times. After these three different cooling down and heating up rates, the thermal cycle loads with the heating/cooling rate of 5 ºC min^{-1} were applied to the membrane. A total of 46 thermal cycling loads was applied to the membrane in about 350 h. During the thermal cycling process, oxygen permeation flux was able to rapidly respond to the temperature changes. When the membrane was maintained at 850 ºC, oxygen permeation flux reached about $1.05\ \mathrm{ml \cdot cm^{-2} \cdot min^{-1}}$. After the temperature was reduced to 600 ºC, oxygen permeation flux decreased to a little bit above $0.0\ \mathrm{ml \cdot cm^{-2} \cdot min^{-1}}$. This observation further confirms the understanding that oxygen permeation process is thermally activated in nature. Once the temperature was increased to 850 from 600 ºC, oxygen permeation flux was quickly recovered back to its original high value of about $1.05\ \mathrm{ml \cdot cm^{-2} \cdot min^{-1}}$. After a total of 46 thermal cycles in about 350 h, oxygen permeation flux was very stable with negligible degradation. This result clearly indicates the excellent stability of the membrane. After the accelerated long-term stability test, the membrane sample was further characterized. Fig. 2.6a shows the cross-sectional SEM image of the sample. Multi-layer structure can still be clearly observed. The radially well-aligned microchannels remained very well, indicating their long-term stability and thermal cycling robustness. The enlarged area (Fig.2.6b) marked with red circle in Fig. 2.6a shows that the dense LSCF separation layer still intimately contacted with both the substrate and porous PBCFZY catalytic layer. No delamination or cracks could be observed. The EDS analysis results of the sample cross section are shown in Fig. 2.6c. The Zn element was still confined within the substrate region, no diffusion into the separation layer or catalytic layer could be detected. The La and Sr elements were limited in the regions of both substrate and dense separation layer while Fe and Co elements were spread in the substrate and dense separation layer as well as porous catalytic layer with different densities in different regions. These element distributions are consistent with the materials used by the membrane and its multi-layer structure. The element Ba was mainly confined within the porous catalytic layer with a slight scattering in the separation layer and substrate. The elements Pr, Zr, and Y were distributed everywhere in the membrane, including substrate, separation layer, and surface catalytic layer. Interestingly, comparing the SEM and EDS of the membrane before (Fig. 2.3) and after (Fig. 2.6) the long-term stability test, one can see that little changes occurred, no further element diffusion took place. This observation indicates that the microstructure and element distribution of the membrane were very stable, which is consistent with the stability of the membrane during the long-term test with severely harsh thermal cycling conditions, e.g., ~550 h, 46 thermal cycles.

2.4 Conclusion

The sintering behaviors of a set of simple oxides, ZnO, MgO, ZrO_2, Al_2O_3, TiO_2, were systematically measured in a wide range of operating temperatures. The ZnO was identified as a material component for the composite hollow fiber substrate LSCF-ZnO. The sintering behaviors and TECs of the LSCF-ZnO composites were further systematically measured to optimize the LSCF-ZnO ratios. As a result, the LSCF-ZnO composite with the sintering behavior and TEC close to those of LSCF was identified. The LSCF-ZnO composite hollow fiber substrate precursor with the identified LSCF-ZnO ratio was then fabricated using slurry spinning process in combination with modified phase inversion method. The thin film separation layer was then successfully fabricated on the composite substrate through dip-coating and co-sintering process. A thin, porous PBCFZY catalyst layer was then built on the dense LSCF separation layer via dip-coating and sintering process, forming an asymmetrical membrane device ZnO-LSCF/LSCF/PBCFZY. Experimental results indicate that oxygen permeation flux increased with increasing operating temperature, indicating thermally activated nature of oxygen permeation process. The permeation process is sensitive to argon sweep gas flow rate at the permeate side and the corresponding OER is a limiting step for oxygen permeation process. The oxygen permeation process is affected by operating conditions in a complicated way, including temperature, oxygen partial pressure/sweep gas flow rate. An accelerated long-term stability test demonstrated excellent robustness and durability of the membrane device. By replacing a considerable amount of high cost LSCF with low cost ZnO in the substrate, the capital cost of the membrane can also be significantly reduced.

Table 2.1 Comparison of oxygen permeation flux of LSCF membranes in open literature, measured under the gradient of Air/He or Air/Ar at 900°C.

Reference	Surface catalysts	Dense layer thickness (μm)	Sweep gas	J_{O2} (mL/cm^2/min)
This work	$PrBaCo(Fe_{0.6}Zr_{0.2}Y_{0.2})O_{5+\delta}$	20	Ar	1.76
[84]	HCl	40	He	0.6
[85]	LSCF	40	He	1.5
[86]	None	88	He	1.4
[87]	Pt	100	Ar	1.1
[88]	None	300	He	0.3
[89]	$Ba_{0.5}Sr_{0.5}Co_{0.9}Nb_{0.1}O_{3-\delta}$	530	He	0.7
[90]	LSCF	710	He	1.0
[64]	$(La_{0.5}Sr_{0.5})_2CoO_{4+\delta}$	750	He	0.9

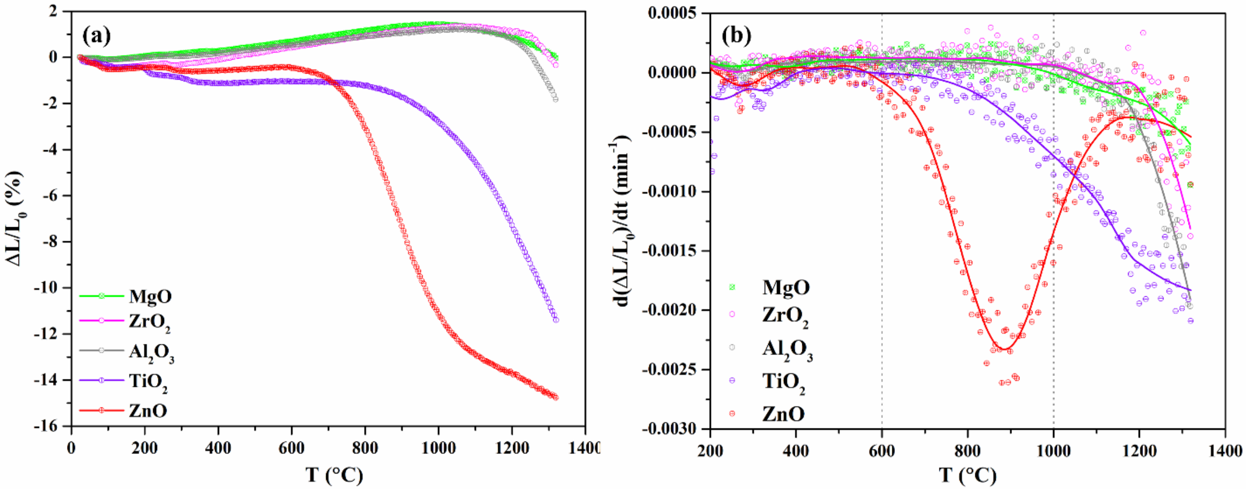

Figure 2.1 (a) Sintering behavior curves of different substrates and (b) their corresponding sintering rates versus temperature.

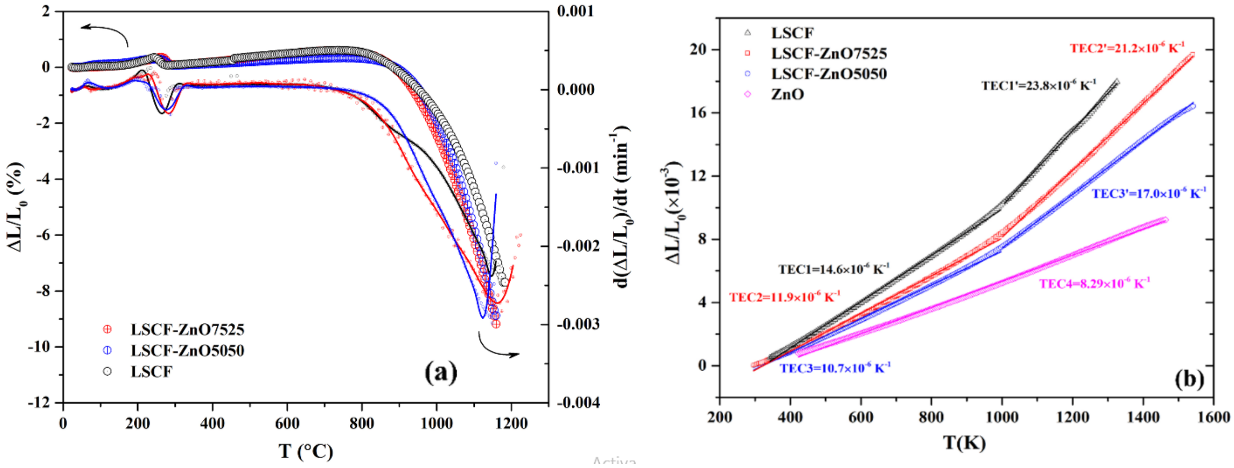

Figure 2.2 Sintering behavior of LSCF and LSCF-ZnO composite substrate precursors, (a) and thermal expansion curves for LSCF, ZnO and LSCF-ZnO composites (b).

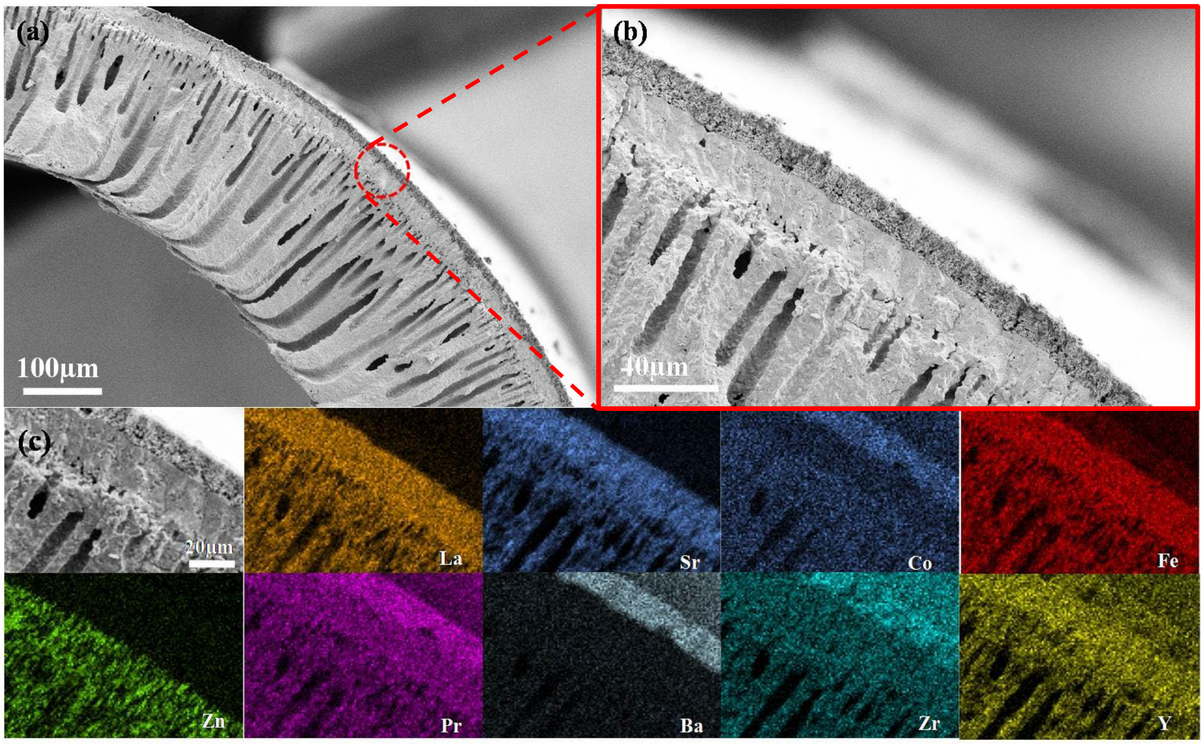

Figure 2.1 Cross sectional SEM image of the LSCF-ZnO7525 supported LSCF membrane coated with PBCFZY catalytic layer (a), Enlarged figure of local area marked with red circle in figure (a) (b) and EDS image of the figure (b) (c).

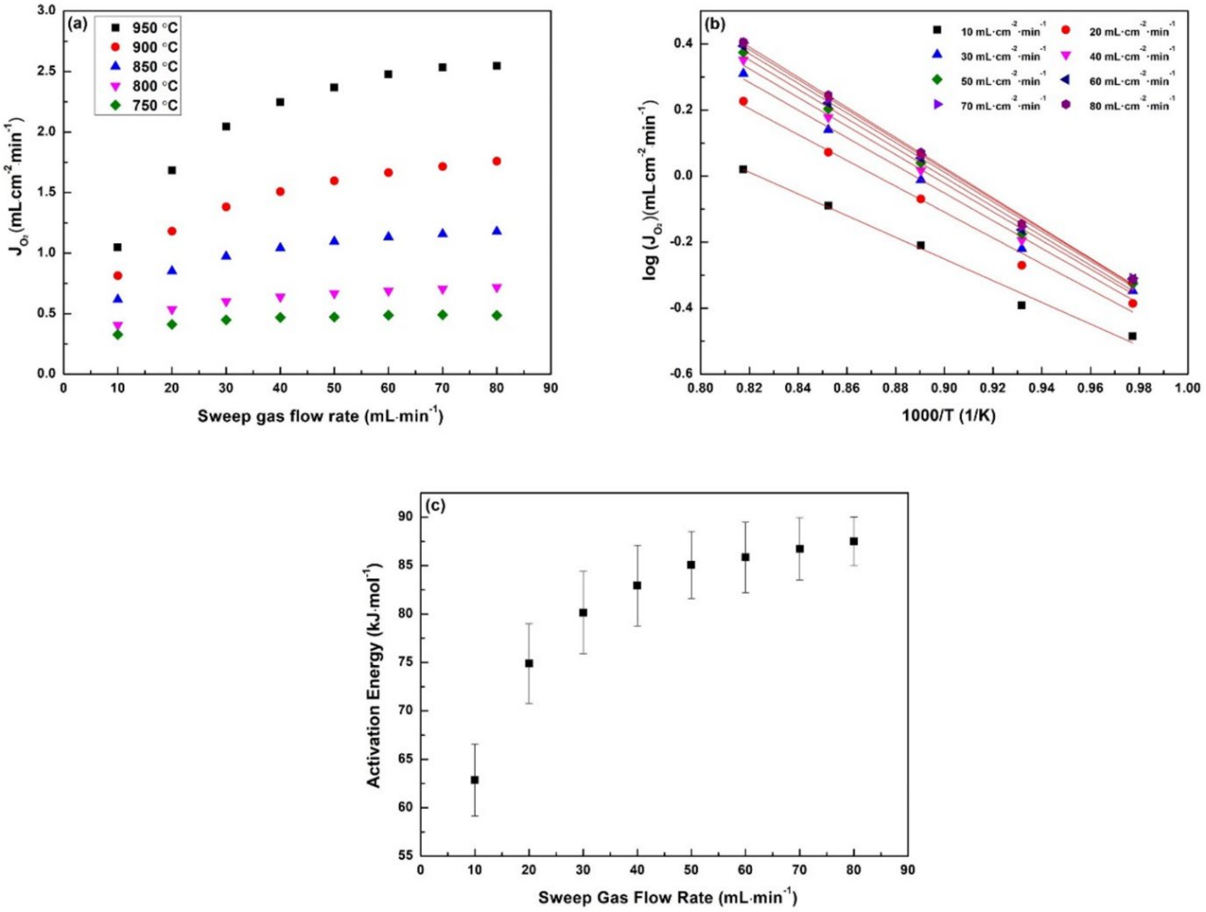

Figure 2.4 Oxygen permeation performance of the membrane (LSCF-ZnO 7525 substrate/LSCF 1270 ºC 6h/PBCFZY catalytic layer 1000 ºC 3h. oxygen permeation flux (a), Arrhenius plot (b), activation energy (c).

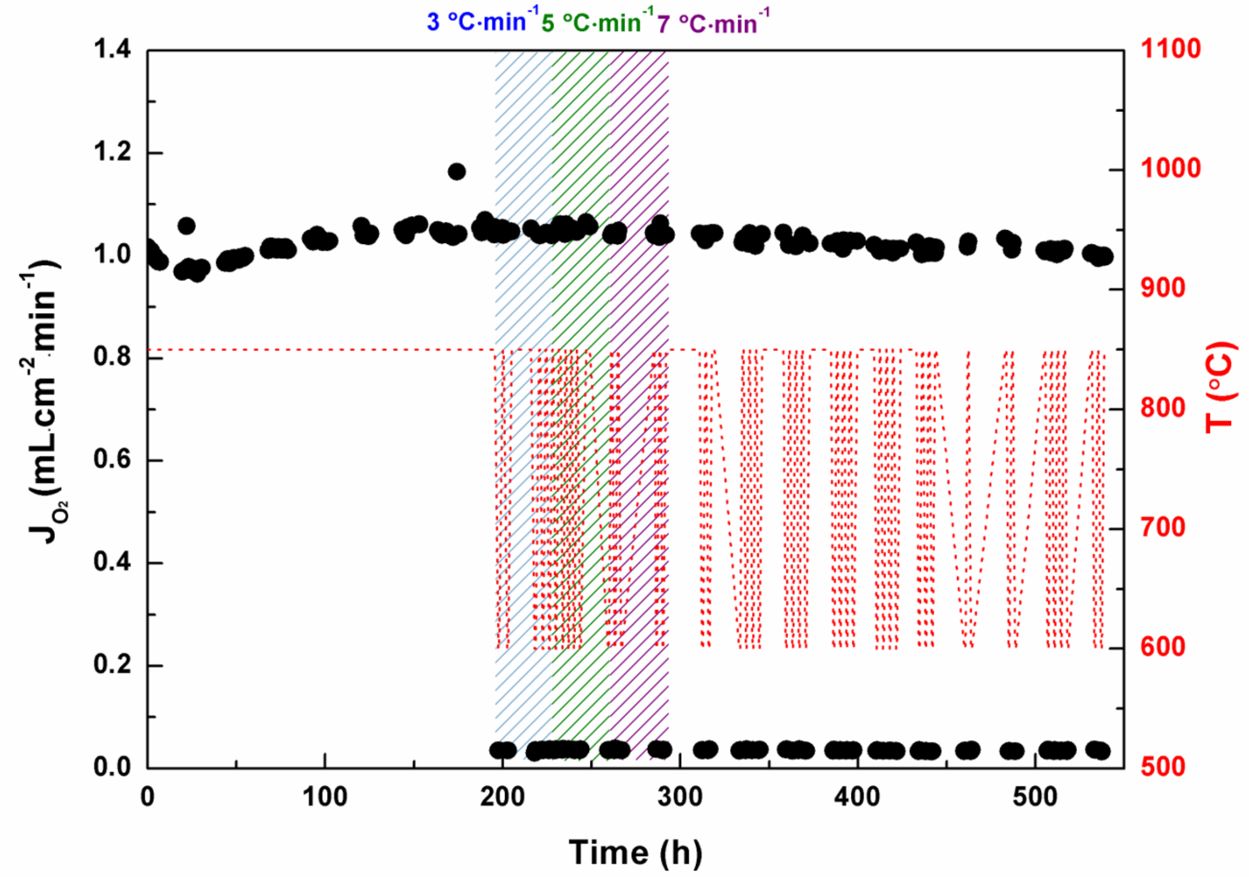

Figure 2.2 Performance of the membrane LSCF-ZnO 7525 substrate/LSCF 1270 ºC 6h/PBCFZY catalytic layer under long-term (~ 550 h) accelerated stability test: ~190 h test at 850 ºC followed by 350 h test with a total of 46 thermal cycles between 850 and 600 ºC.

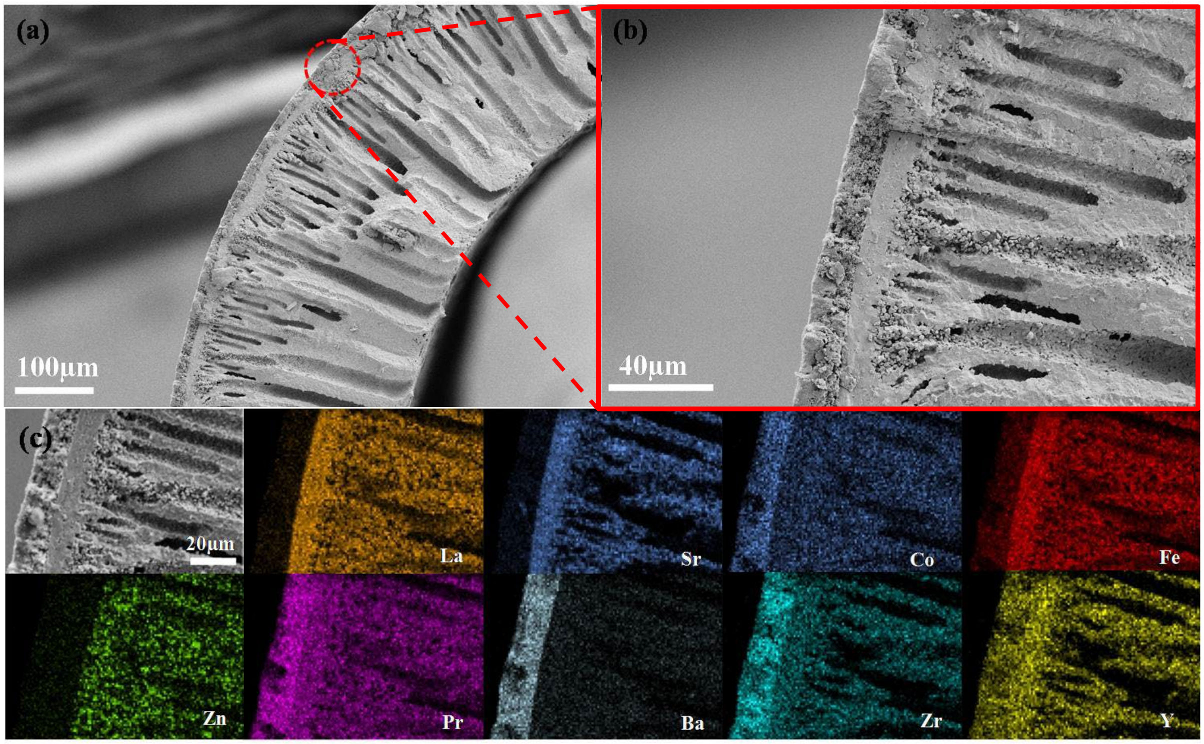

Figure 2.3 Cross sectional image of the membrane after stability test (a), Enlarged figure of local area marked with red circle in figure (a) (b) and EDS image of the figure (b) (c).

CHAPTER 3

STACK DEVELOPMENT WITH ASYMMETRIC HOLLOW FIBER-SUPPORTED THIN FILM MEMBRANES FOR OXYGEN SEPARATION FROM AIR

3.1 Introduction

Oxygen is an important chemical and widely used in industrial processes such as the manufacturing of glass, semiconductors, and metals etc., petrochemical process, and other industrial processes. With increasing concerns on pollutions and climate change, oxy-combustion technology is pursued to replace conventional air-combustion for coal gasification and clean coal process, where oxygen instead of air is directly used for combustion process. Oxy-combustion technology can provide a series of advantages, including significant improvement on the efficiency of power plant, facile CO_2 capture with high CO_2 concentration, and minimization of NO_x emissions [91, 92]. Therefore, mass production of oxygen is a critical step, enabling these technologies. In industry, oxygen has been produced using the technologies of cryogenic process [93] and pressure swing adsorption [94]. However, these technologies are usually very complex in system design, energy-intensive and expensive in operations. Oxygen production from air separation using membrane technologies has attracted increasing attentions in the past decades. One of such membrane technologies is based on the concept of molecular sieve, where gas species with molecular sizes less than the pore size of porous material bulk can pass through and is separated from the feeding gases [95]. Therefore, very uniform pore size and porous structure are critical for such a membrane technology. It is very difficult to separate gas species with same or similar molecular sizes. Consequently, it is very difficult for such a membrane to achieve very high selectivity. The membrane technology with electrochemical permeation process can overcome this shortcoming. Compared to molecular sieve-based porous membrane, the electrochemical membrane is gas-tight, not allowing any gas species to pass through directly. An indirect route is utilized for certain gas species, e.g., oxygen, to pass through. Specifically, oxygen reduction reaction (ORR) at membrane surface of the feed side converts oxygen molecules into oxygen ions. The oxygen ions are then incorporated into oxygen vacancies of membrane bulk, transporting toward the permeate side. On the surface of permeate side, oxygen evolution reaction (OER) changes oxygen ions back to oxygen molecules by releasing electrons, completing oxygen separation from the feed side. Therefore, high purity oxygen with 100% selectivity in theory can be obtained using electrochemical separation membrane. During the process, ions and electrons transport in opposite directions in material bulk between feed surface and permeate surface, enabling continuous operations of ORR and OER, and oxygen separation. This requires that membrane material be able to conduct ions and electrons simultaneously, such as mixed ionic and electronic conductors (MIECs) or the composite of ionic and electronic conductors. From operation point of view, oxygen partial pressure gradient across the membrane is needed to drive ORRs and OERs. These features make electrochemical membranes very attractive in oxygen production from air.

For practical applications, suitable geometric design of membranes is needed to facilitate not only high-performance oxygen production but also fabrication and setup of membrane systems. The widely used designs are planar and tubular membranes. While these designs have their different advantages, the common issue is the need of a relatively long sealing length. This issue was significantly mitigated by miniaturizing tubular design, e.g., hollow fiber membrane [96]. In addition to the short sealing length, the unique feature of hollow fiber membranes is their large area to volume ratio [97]. This renders the upscaling possible towards a compact hollow fiber membrane stack.

Nevertheless, the intrinsic small diameters and material brittleness limit mechanistic strength of individual hollow fiber membranes, therefore their robustness and stability. This in turn limits the upscaling ability of hollow fiber membranes for compact stack/module development, especially using the classic stack design strategy [98,99]. To circumvent this issue, alternative strategies were attempted to scaling up hollow fiber membrane technology, including cantilever-like hollow fiber stack assembly [69, 76, 100] and hollow fiber bundle [60, 72, 73]. The cantilever-like assembly strategy can prevent mechanical loads from applying on hollow fiber membranes, therefore mitigating the reliable issue induced by the insufficient mechanical strength. But one side port of individual hollow fibers needs to be closed end for appropriate operations, confining stack operating modes to the vacuum mode only. The bundle strategy is to bundle individual hollow fibers together with porous ceramic material, significantly enhancing the mechanical strength of bundle stack. It is noteworthy that the porous material used to bundle hollow fiber membranes will increase the resistance for gas diffusion between bundle circumference and individual hollow fibers in the bundle. If too many hollow fibers are bundled together, oxygen partial pressure at the middle part of the bundle would become low, directly deteriorating its oxygen permeation performance. In this situation, the hollow fibers in the middle part could only play a role in enhancing the mechanical strength of the bundle.

It was also observed that increasing the number of hollow fibers in a bundle can effectively improve its mechanical strength for a small number of hollow fibers but becomes less effective beyond a certain number due to complicated structural interactions among hollow fibers. Clearly, to effectively scaleup hollow fiber technology with bundle strategy, the number of bundled hollow fibers should be limited. It is worth mentioning that gas-tight sealing is very critical for membrane technology. The sealing issue becomes more prominent at stack level due to the increased sealing length. For easy gas-tight sealing, the low-temperature sealant materials of epoxy resin or silicon were typically used for hollow fiber stacks. To avoid high-temperature conditions, the sealing portions of the stack must be located out of hot zone. Consequently, a significant portion of hollow fibers only plays a role of supporting, gas transport and facilitating sealing, contributing little to oxygen permeation. Given high capital cost of membrane materials, ideally, the full length of hollow fibers in the stack should be able to participate in efficient oxygen permeation. This requires that the full length of hollow fibers and therefore the sealing portion be confined in hot zone. This further implies that hollow fibers in the stack should be strong enough to support various loads and sealing portions should be reliable in harsh temperature conditions.

The mechanical strength of hollow fiber membranes is dependent on the used materials and microstructures obtained during fabrication process. At early stage, hollow fiber membrane is fabricated using slurry spinning and one-step sintering process. The resultant microstructure of the hollow fiber is a sandwiched structure, where the middle sponge-like layer is sandwiched by finger-like layer on either side, and the inner and outer surfaces are covered with relatively dense thin skin layers [69, 101-103]. A high sintering temperature is needed to obtain gas-tight membrane with such microstructures; however, it is very difficult to eliminate finger-like pores. The closed finger-like pores in the membrane reduce effective conductivity for charge transport and may induce redundant ORRs/OERs. To mitigate this issue while taking advantage of finger-like pores, hollow fibers with finger-like pores open at the inner surface were fabricated using modified slurry spinning process [63, 87, 104]. Instead of using tap water as coagulant at outer/inner surface of hollow fibers during spinning process, a mixture of solvent and tap water was used as coagulant at the inner surface. The solvent gradient between inner and outer surfaces leads to different phase exchange rates and creates open finger-like pores at the inner surface. After one-step sintering, gas-tight hollow fiber membrane was obtained. Since the skin layer formed through phase inversion process is porous, a relatively high sintering temperature is needed. The open finger-like pores facilitate facile gas diffusion, however, the mechanical strength of such a hollow fiber is even weaker than the above multilayer counterpart. To improve the mechanical strength of hollow fibers, both material and microstructure strategies have been attempted in open literature.

For example, $La_{0.6}Sr_{0.4}CoO_3$ (LSC) was composited with stainless steel to improve the mechanical strength of the corresponding hollow fiber membrane but deteriorate oxygen permeation flux [105]. Hollow fiber with multi-bores was also fabricated to improve its mechanical strength but significantly sacrifice permeation performance because it is difficult to control microstructure of the membrane [106]. Recently, our group developed an asymmetric hollow fiber substrate-supported thin film membrane [107]. This new strategy provides the flexibility to use different materials and microstructures in different layers, therefore obtaining excellent tradeoff between oxygen permeation performance and mechanical strength. A composite hollow fiber substrate with radially aligned open microchannels provides sufficient mechanical strength and allows facile gas transport, while a thin film on the substrate may significantly reduce ohmic resistance for charge transport. Although multiple steps are involved in fabricating such a hollow fiber membrane, a relatively low sintering temperature is needed to densify thin film gas separation layer. This new hollow fiber membrane demonstrated excellent robustness and reliability and can potentially be used for upscaling of membrane technology with various stack designs.

In this research, membrane stack was developed using hollow fiber substrate-supported thin film membranes. For the proof of concept, three hollow fibers were used for the stack assembly. Hollow fibers were arranged in parallel and connected to supporting alumina tubes at either end through sealing. A reliable gas-tight sealing was obtained by using ceramic paste and conductive adhesive ink alternatively so that the entire stack can be operated in hot zone. Alumina tubes were used to support hollow fibers and serve as gas distributor and collector at gas inlet and outlet respectively. Oxygen permeation performance of the stack was systematically measured and compared with a single hollow fiber membrane. The fundamental mechanism was discussed. An accelerated long-term stability test (~320 h) was also conducted to demonstrate the robustness and reliability of the stack. While the stack with three hollow fiber membranes was developed in this study, upscaling hollow fibers to large stacks and modules can be implemented using the same strategy. Other strategies such as membrane bundle and cantilever-like stack are also applicable.

3.2 Experimental

3.2.1 Fabrication of hollow fiber membrane, stack design, and assembly

Composite hollow fiber-supported thin film membrane was fabricated via modified phase inversion, dip-coating, and sintering processes. Briefly, a composite powder (simply denoted as LSCF-ZnO7525) was prepared using ball-milling process, composed of 75 wt.% $La_{0.6}Sr_{0.4}Co_{0.2}Fe_{0.8}O_{3-\delta}$ (LSCF, Fuel cell materials, USA) and 25 wt.% zinc oxide (ZnO, 200 Mesh, Alfa Aesar, USA). LSCF-ZnO7525 slurry was prepared by ball-milling with 68 wt.% LSCF-ZnO7525 powder and organic solvent (5.21 wt.% polyether sulfone, 0.74 wt.% polyvinylpyrrolidone, 26.05 wt.% N-methyl-2-pyrrolidone). Hollow fiber precursor was then obtained through slurry spinning process using lab-built spinneret apparatus, where tap water and the mixture of 95 vol. % N-methyl-2-pyrrolidone and 5 vol. % tap water were used as outer and inner coagulants respectively. LSCF thin film dense separation layer was then fabricated on LSCF-ZnO7525 hollow fiber substrate, followed by the fabrication of $PrBaCo(Fe_{0.6}Zr_{0.2}Y_{0.2})O_{5+\delta}$ (PBCFZY) catalytic layer on the separation layer by dip-coating and sintering process respectively, forming a single hollow fiber membrane LSCF-ZnO7525/LSCF/PBCFZY. The details of the fabrication process and associated system have been reported elsewhere [77, 107-110].

Fig. 3.1a shows the photo of the fabricated sample membranes. The sample cross-sectional scanning electron microscopy (SEM) image shown in Fig. 3.1b and 3.1c indicates that radially well-aligned microchannels with the diameter of 20-30 μm are embedded in LSCF-ZnO7525 substrate and open at the inner surface. The dense LSCF separation layer with the thickness of ~ 30μm shows intimate contact with both LSCF-ZnO7525 substrate and ~ 15 μm PBCFZY catalyst layer. The open microchannels start from inner surface of hollow fiber and reach all the way to the LSCF dense separation layer.

With the fabricated LSCF-ZnO7525/LSCF/PBCFZY hollow fiber membranes, membrane stack was developed. The top part in Fig. 3.1d shows the membrane stack design. Two alumina tubes were used to support individual hollow fiber membranes at either end. The alumina tubes also play a role of gas distributor and collector at inlet and outlet respectively. The dimensions of alumina tube are internal diameter x external diameter x length = 1cm x 1.2cm x 26cm. Individual hollow fiber membranes were arranged in parallel and connected to the alumina tubes. The connecting portions between the alumina tubes and membranes were sealed by conductive adhesive ink (DAD-87, Shanghai Research Institute for Synthetic Resins, China) and ceramic paste (Aremco Products Inc., USA). Conductive adhesive ink and ceramic paste were applied for sealing alternatively. Specifically, a thin layer of conductive adhesive ink was applied to the connecting part, followed by aging at 200 °C in air for 30 min. After positioning and fixing all the hollow fibers, conductive adhesive ink was further applied to the surface of the sealing area, followed by aging at 900 °C in air for 30 min. Then ceramic paste and conductive adhesive ink were alternatively applied for additional two times with sufficient drying in air at room temperature between every single sealing step. The resultant membrane stack assembly is shown in the bottom part of Fig. 3.1d. The individual hollow fiber with the length of ~ 45 mm was assembled in the stack. After sealing, the length of the membranes exposed to ambient air is ~ 22 mm. The total area for oxygen permeation is ~ 3.9 cm^2. While three hollow fiber membranes were assembled to form a stack in this study, membrane stack at large scale can be obtained using the same strategy.

3.2.2 Oxygen permeation performance measurement and characterization

Oxygen permeation performance of the developed hollow fiber membrane stack was systematically measured. Fig. 3.2a shows the schematic of experimental setup. A high-temperature furnace (MTI, USA) was used to control the temperature of the membrane stack system. Hollow fiber membranes and sealing portions as well as part of the supporting tubes were confined in the hot zone. Argon at room temperature was supplied into the supporting alumina tube at one end, which was further distributed into individual hollow fiber membranes in the stack. Argon flow rate was controlled by a gas flow meter (APEX). The shell sides of the involved hollow fiber membranes were exposed to ambient air. The supporting alumina tube at the other end collected gases from the lumen sides of hollow fibers. The compositions of effluent gases from outlet alumina tube were analyzed by an online gas chromatography (GC-8A, Shimadzu, Japan) equipped with a 5Å molecular sieve column. Fig. 3.2b illustrates transport processes through individual hollow fiber membranes in the stack, including ORR at the surface of shell side, OER at the surface of lumen side, and charge (ions and electrons) transport via dense separation layer. Oxygen permeation performance of the stack was measured in the temperature range of 750 – 950 °C and at different argon sweep gas flow rates of 30 – 480 mL min^{-1}.

An accelerated long-term stability test (~ 320 h) was also conducted. In the stability test, a constant argon sweep gas flow rate of 240 mL·min^{-1} was supplied into the stack, and a constant operating temperature 900 °C was first applied, followed by fluctuating temperatures between 900 and 600 °C for about 16 thermal cycles. The time history of oxygen permeation performance was monitored and recorded by the online GC.

Scanning electron microscopy (SEM, Zeiss Gemini500 FESEM, Germany) was used to observe microstructures of fabricated and post-test membrane samples and energy-dispersive X-ray spectroscopy (EDS) mapping technology was employed to analyze spatial distribution of elements in the samples. X-ray diffraction (XRD; D/Max-3C) technique was utilized to examine the phases of materials and post-test membrane samples.

3.3 Results and Discussion

Fig. 3.3a shows oxygen permeation rates of the stack in the temperature range of 750-950 °C with the argon sweep gas flow rates of 30-480 $mL \cdot min^{-1}$. For a given argon sweep gas flow rate, oxygen permeation rate increases with operating temperature, indicating thermally activated nature of oxygen permeation process. Depending on specific operating temperatures, argon sweep gas flow rate demonstrates different effects on oxygen permeation rate. At 850 °C and below, oxygen permeation rate increases with argon sweep gas flow rate, implying that the process associated with permeate side is a limiting subprocess. Beyond a certain sweep gas flow rate (simply denoted as threshold value), oxygen permeation rate approaches a constant value, indicating that the process associated with permeate side is no longer a limiting subprocess. It is also observed that the threshold value of sweep gas flow rate increases with increasing operating temperatures, implying that operating temperature may change the limiting subprocess to a non-limiting one. When the stack is operated at temperatures above 850 °C, oxygen permeation rate keeps increasing with argon sweep gas flow rate. In other words, increasing temperature may raise the threshold value of sweep gas flow rate. This result further indicates that operating temperature is coupled with oxygen permeation process in a very complicated way. When argon sweep gas flow rate is increased, oxygen partial pressure will be decreased at the permeate side. Since the feed side of the stack is exposed to ambient air, the chemical gradient of oxygen across the membranes will be increased. Accordingly, oxygen permeation performance should be enhanced.

Nevertheless, the observations shown above clearly indicate that this is not always the case. It is worth mentioning that argon at room temperature was supplied to the stack. This will decrease temperatures of individual hollow fibers in the stack, deteriorating stack performance. This effect becomes stronger at higher sweep gas flow rates. The competing effects of oxygen gradient and argon sweep gas flow rate led to the complicated oxygen permeation behaviors at different temperatures and sweep gas flow rates. Fig. 3.3b shows oxygen permeation flux of the stack, which is obtained by normalizing oxygen permeation rate with surface area of the stack. Obviously, oxygen permeation flux demonstrates the same trend as oxygen permeation rate. Arrhenius plots derived from oxygen permeation flux (Fig. 3.3b) are shown in Fig. 3.3c. The corresponding activation energies calculated from Fig. 3.3c are shown in Fig. 3.3d. The activation energy of the stack increases with increasing argon sweep gas flow rate. As mentioned above, argon sweep gas at room temperature was supplied to the stack, which directly decreases the temperature of individual hollow fiber membranes in the stack.

This in turn increases energy barriers of every single step involved in oxygen permeation process because the process is thermally activated in nature. When sweep gas flow rate increases from 30 to 180 mL·min^{-1}, activation energy increases at a rapid rate;

beyond 180 mL·min^{-1}, activation energy increases at a relatively slow rate. In principle, sweep gas flow should enhance heat transfer effect, i.e., the higher the sweep gas flow rate, the lower the individual hollow fiber temperature. Consequently, activation energy keeps increasing with argon sweep gas flow rate. Nevertheless, different increasing rates of activation energy at different sweep gas flow rates also imply that activation energy is affected by other parameters. It is mentioned above that argon sweep flow decreases oxygen partial pressure at the permeate side of individual hollow fiber membranes, and therefore increasing oxygen gradient across individual membranes. Since the temperature at feed side of individual membranes is slightly higher than permeate side, oxygen permeation through membranes would slightly increase individual membrane temperatures. This effect is dependent on argon sweep gas flow in a complicated way. This could be the reason that activation energy increases at different rates from sweep gas flow rate range of 30 to 180 mL·min^{-1} to the range of beyond 180 mL·min^{-1}. Inserted figure in Fig. 3.3d is the activation energy of a single hollow fiber membrane under the same operating conditions as the stack. At the same equivalent argon sweep gas flow rate, the activation energy of a single membrane is always larger than the stack. For example, at argon sweep gas flow rate of 30 mL·min^{-1} for the stack or equivalently 10 mL·min^{-1} for the single membrane, the activation energy of single membrane is ~ 73 kJ·mol^{-1} while that of the stack is ~ 55 kJ·mol^{-1}. Similarly, at argon sweep gas flow rate of 240 mL·min^{-1} for the stack or equivalently 80 mL·min^{-1} for the single membrane, the activation energy of single membrane is ~ 93 kJ·mol^{-1} while that of the stack is ~ 75 kJ·mol^{-1}. Obviously, hollow fiber membranes demonstrate different activation energy in the stack from the single membrane setting even though the operating condition is the same. When single hollow fibers are assembled into a stack, radiation heat transfer among hollow fibers facilitates to maintain their temperatures at a slightly higher level than the single membrane setting counterpart. Therefore, the activation energy of the membrane stack was smaller than the single hollow fiber membrane under the same operating conditions.

Fig. 3.4a shows oxygen permeation rates of the stack and single hollow fiber membrane under different temperatures and argon sweep gas flow rates. At a given sweep gas flow rate, oxygen permeation rate increases with operating temperature for both the stack and single membrane because of thermally activated nature of oxygen permeation process as mentioned above. For a given operating temperature, a larger sweep gas flow rate leads to a slightly higher oxygen permeation rate. At an equivalent argon sweep gas flow rate, e.g., 40, 60, and 80 $mL\cdot min^{-1}$ for the single membrane or equivalently 120, 180, and 240 $mL\cdot min^{-1}$ for the stack respectively, the oxygen permeation rate of the stack is always higher than the single membrane. When single hollow fibers are assembled in parallel to form a stack, effective length and therefore area for oxygen permeation is increased compared to a single membrane. Since operating conditions of the stack are the same as the single membrane, e.g., temperature, sweep gas flow rate, the increased length and area directly lead to the increased oxygen permeation rate. Fig. 3.4b displays oxygen permeation flux of the stack and single membrane, which is obtained by normalizing oxygen permeation rate in Fig. 3.4a using the surface area of the stack and single membrane respectively. One can see that oxygen permeation flux shows similar trend to oxygen permeation rate. At relatively low operating temperatures, oxygen permeation flux of the stack is close to or slightly lower than the single membrane. At relatively high operating temperatures, however, the former is obviously higher than the latter. For instance, at 750 °C, oxygen permeation flux of both stack and single membrane reached approximately the same value of ~ 0.5 $mL\cdot cm^{-2}\cdot min^{-1}$; when the temperature of 950 °C was applied, the stack obtained oxygen permeation flux of ~ 1.25, 1.75, and 2.0 $mL\cdot cm^{-2}\cdot min^{-1}$ at argon sweep gas flow rate of 120, 180, 240 $mL\cdot min^{-1}$ respectively or equivalently the sweep gas flow rate of 40, 60, and 80 $mL\cdot min^{-1}$ for single hollow fiber membrane. While the single membrane obtained oxygen permeation flux of ~ 2.25, 2.5, and 2.52 $mL\cdot cm^{-2}\cdot min^{-1}$ under the same operating conditions respectively. As mentioned above, a cluster of hollow fiber assembly in a stack facilitates to maintain high temperatures of individual membranes due to mutual radiation heat transfer effects, therefore enhancing oxygen permeation performance. On the other hand, a cluster of hollow fibers in the stack permeates more oxygen than a single membrane, diluting oxygen concentration nearby in a faster way. As a result, oxygen gradient across the membranes in the stack is lower than a single membrane setting, leading to a smaller oxygen permeation flux. The combination of these two effects leads to different oxygen permeation fluxes in the same operating conditions. At relatively low temperatures, radiation heat transfer effect could be comparable to oxygen concentration dilution effect, resulting in similar oxygen permeation flux for both stack and single membrane. With increasing temperatures, the effect of the latter could exceed the former, therefore oxygen permeation flux of the stack is lower than the single membrane under the same operating conditions. Compared to a single membrane, stack assembly increases surface area for oxygen permeation. It is anticipated that oxygen permeation rate of the stack should be higher than the single membrane under identical operating conditions. This understanding is confirmed by the results in Fig. 3.4c, where the same argon sweep gas flow rate was applied to both the stack and single membrane. At every single operating temperature, oxygen permeate rate of the stack is higher than the single membrane. However, the oxygen permeation flux of the former is lower than the latter (Fig. 3.4d) under identical operating conditions. With increasing temperatures, the difference in oxygen permeation flux produced by the single membrane and membrane stack also increases. Argon sweep gas flow is split into three parallel-connected hollow fibers, resulting in lower sweep gas flow rate in each of the hollow fibers in the stack than in the single membrane setting.

Therefore, oxygen partial pressure at the permeate side of the former is lower than the latter. Recalling the dilution of oxygen concentration at the feeding side in the stack, it is not difficult to see that oxygen permeation performance of the stack would be weakened by these two effects. On the other hand, it is mentioned above that radiation effect among parallel-connected three hollow fibers in the stack facilitates to maintain their high temperatures, enhancing oxygen permeation performance of individual hollow fibers.

The difference of oxygen permeation flux between single hollow fiber membrane and the stack in the same operating condition could be determined by these three effects. At relatively low operating temperatures (750 – 800 ºC), the influence of radiation effect could be comparable to those of oxygen concentration dilution and argon sweep gas flow, leading to the result that oxygen permeation flux of the single membrane is just slightly higher than the stack. At relatively high temperatures (850 – 950 ºC), oxygen permeation performance will be significantly improved due to thermally activated nature of membrane materials and the dilution effect of oxygen concentration will be further enhanced. Accordingly, the influence of the radiation effect could be much weaker than those of oxygen concentration dilution and argon sweep gas flow. This could be the reason that oxygen permeation flux of the single membrane is much higher than the stack in these conditions.

An accelerated long-term stability test was also conducted, where a constant argon sweep gas flow rate of 240 mL·min^{-1} was supplied into the stack. During the test, different thermal loads were applied to the stack and oxygen permeation rate was sampled using GC during the daytime but without sampling during the nighttime. And the corresponding oxygen permeation flux of the stack was obtained. Fig. 3.5 shows the time history of the applied thermal loads (right vertical axis) on the stack and oxygen permeation flux (left vertical axis). During the first ~ 192 h, stack temperature was maintained at 900 °C and oxygen permeation rate was sampled every two hours.

Following this constant thermal load, a fluctuating thermal load was applied to the stack. Specifically, stack temperature was cooled down from 900 to 600 °C at a cooling rate of 3 °C·min^{-1}, kept at 600 °C for 1 h, heated up back to 900 °C at the same rate, and then kept at 900 °C for 1 h. This thermal cycle was repeated for three times. The thermal cycle with cooling/heating rates of 5 and 7 °C·min^{-1} was then applied and repeated for three times respectively. After a total of 9 thermal cycles, the heating/cooling rate was changed back to 5 °C·min^{-1} for additional 7 cycles. During thermal cycles, oxygen permeation rate was sampled every 30 min to capture its rapid response. From Fig. 3.5, one can see that oxygen permeation flux was very stable and maintained at ~ 1.65 mL·cm^{-2}·min^{-1} at the constant temperature of 900 °C during the first 192 h. Once thermal cycling load was applied to the stack, the corresponding oxygen permeation flux varied between ~ 1.65 mL·cm^{-2}·min^{-1} and ~ 0.02 mL·cm^{-2}·min^{-1} when the temperature alternated between 900 and 600 °C respectively. Overall, during the accelerated long-term test with a total of 320 h and 16 thermal cycles, the stack demonstrated excellent stability and robustness. No obvious performance degradation was observed. Since the sealing portions of the stack were in the hot zone, the result also implies that the sealing portions were very robust and stable.

After the stability test, material phases of membranes in the stack were further characterized. Membrane sample was taken off from the stack and then crushed into powder, which was characterized by XRD technique. As a comparison, the XRD patterns of as-synthesized PBCFZY and as-purchased LSCF were obtained. Meanwhile, the mixture of PBCFZY (50 wt. %) and LSCF (50 wt. %) was heat-treated in air at 1100 ^{o}C for 10 h. The XRD patterns of the mixed powders were also obtained. Fig. 3.6 shows XRD patterns of PBCFZY, LSCF, the mixture of PBCFZY and LSCF after heat treatment, and the post-test membrane sample respectively. Obviously, after the heat treatment of PBCFZY and LSCF mixture, the main peaks corresponding to PBCFZY and LSCF phase were observed, and no secondary phases could be detected, indicating excellent chemical compatibility between PBCFZY and LSCF. The XRD of the post-test membrane sample in the stack shows that the main peaks correspond to LSCF, PBCFZY, and ZnO phases, no other secondary phases could be detected within the sensitivity of XRD technique. The result further indicates the excellent chemical compatibility and stability of the membrane materials.

The post-test membrane samples in the stack were also characterized using SEM and EDS techniques. As shown in Fig. 3.7a, radially aligned microchannels in the substrate created at the fabrication stage remained very well after stability test, indicating their excellent robustness and stability. The zoomed part in Fig. 3.7b clearly shows that the

LSCF dense separation layer intimately contacts with both the LSCF-ZnO7525 substrate and PBCFZY porous catalyst layer. No delamination can be observed at PBCFZY/LSCF or LSCF/LSCF-ZnO7525 interfaces. Since the stack experienced very harsh thermal cycling conditions, the SEM observation indicates that the microstructure of hollow fiber membrane in the stack is very stable and robust. The EDS results are shown in Fig. 3.7c. La and Sr elements were strictly confined within the region of LSCF-ZnO7525 substrate and LSCF separation layer. Zn element was confined within the region of LSCF-ZnO7525 substrate. Ba and Zr elements were mainly confined in the PBCFZY porous layer but slightly diffuse into the LSCF separation layer and LSCF-ZnO7525 substrate. Co and Fe elements were distributed in the entire cross-section but had different densities in different regions due to different element contents in PBCFZY and LSCF phases respectively. Interestingly, the elements of Pr, Zr, and Y supposed to be only in the PBCFZY porous layer were diffused into both LSCF separation layer and LSCF-ZnO7525 substrate. Previous study has shown that these element diffusions were mainly induced by high sintering temperature at the membrane fabrication stage and the accelerated long-term stability test did not further worsen the element diffusion [25]. The stable and robust performance of the stack in the long-term harsh thermal cycling conditions (~320 h, 16 thermal cycles) further verifies that the microstructures of individual hollow fiber membranes and associated sealing portions are very stable and robust.

Table 3.1 provides comparisons of small-scale hollow fiber membrane stacks developed in this study and open literatures, including stack/design assembly, sealant, stability test conditions, and oxygen permeation performance at 900 ºC. Three types of stack designs were identified, e.g., hollow fibers were bundled with ceramic slurry (simply denoted as bundle stack), hollow fibers were individually sealed to the stack at one end like cantilever fibers while the other end of the fibers was a closed-end (simply denoted as cantilever-like stack), and hollow fibers were parallelly assembly into stack in this study by sealing either end of the fibers (simply denoted as parallel stack). As mentioned above, the designs of bundle and cantilever-like stack were employed to circumvent reliability issue induced by weak mechanical strength of individual hollow fibers. For example, cantilever-like stack can avoid external mechanical loads applied on individual hollow fibers, while the bundle design can enhance the stack reliability by bundling individual hollow fibers together. In present study, the strong mechanical strength of composite hollow fiber substrate-supported asymmetric thin film membrane allows to assembly hollow fibers individually in parallel, forming a membrane stack. Such a parallel stack design can fully take advantage of microstructural features of individual hollow fiber membranes, enhancing stack performance. In fact, oxygen permeation flux of the parallel stack reached ~ 1.60 $mL\cdot cm^{-2}\cdot min^{-1}$ at 900 ºC, which is much higher than those of bundle and cantilever-like stacks with similar material systems under the same operating temperatures. The parallel stack also demonstrated excellent accelerated long-term stability with ~ 320 h and 16 thermal cycles. It is noteworthy that the sealing portions of the parallel stack were operated in the hot zone while those of the bundle and cantilever-like stack were operated out of hot zone. Given the very harsh thermal cycling conditions, the results further confirm the excellent stability and robustness of the stack in this study. While the parallel stack was demonstrated with sealing portions being operated in hot zone, the composite hollow fiber substrate-supported asymmetric thin film membranes are also applicable to the bundle and cantilever-like stack designs with sealing portions being operated out of hot zone.

3.4 Conclusion

In this research, oxygen permeation flux and long-term stability of the LSCF-ZnO 7525 composite hollow fiber substrate supported asymmetrical membrane stack was studied. By utilizing the composite substate, the mechanical strength of the membrane was improved. The ceramic paste and the conductive adhesive ink were used to seal which can withstand high temperature. This sealing strategy make the whole membrane area can be placed in the high temperature furnace zone without any sacrifice the effective membrane area compared to sealing with epoxy resin or silicon sealant. The oxygen permeation process of the stack is affected by operating temperature and sweep gas flow rate. The stack showed high oxygen permeation flux and maintained this flux for 320 h of long-term stability test even under 16 cycles of thermal cycling conditions. The stack demonstrated robust structure and durability, showed the feasibility of assembly of stack in this work.

Table 3.1 Comparison of long-term stability of membrane stack at 900℃ in open literature.

Number of single membranes	**Sealant and sealing part region**	**Stack design**	**Oxygen permeation flux ($mL\cdot cm^{-2}\cdot min^{-1}$)**	**Stability test (h)**	**No. of thermal cycles**	**Reference**
3 LSCF/PBCFZY	Ceramic paste/conductive adhesive ink; in hot zone	Parallel stack	1.60	320	16	This work
3 $La_{0.6}Sr_{0.4}CoO_{3-\delta}$	>350℃ sealant; out of hot zone	Cantilever-like stack	0.96	300	None	[23]
5 LSCF	N/A; out of hot zone	Bundle	0.22	45	5	[14]
8 LSCF	Epoxy, silicone glue; out of hot zone	Cantilever-like stack	0.02	50	None	[12]
10 LSCF	High temperature silicone; out of hot zone	Bundle	0.3	120	None	[13]

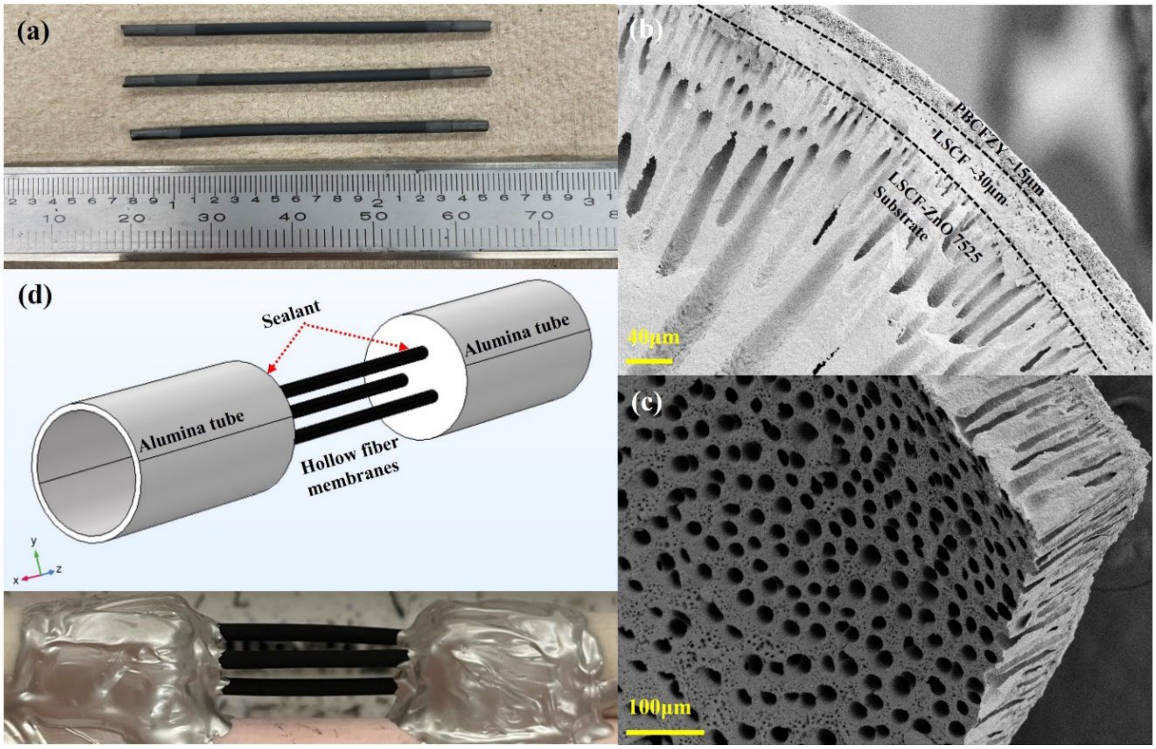

Figure 3.1 Photo of the fabricated LSCF-ZnO 7525/LSCF functional layer/PBCFZY catalytic layer membranes (a), SEM image of the hollow fiber membrane; (b) Cross-sectional of the fabricated membrane (b-c), Inner surface of the LSCF-ZnO 7525 substrate (c), 3D design of the stack assembly, and the assembled stack test stand (d).

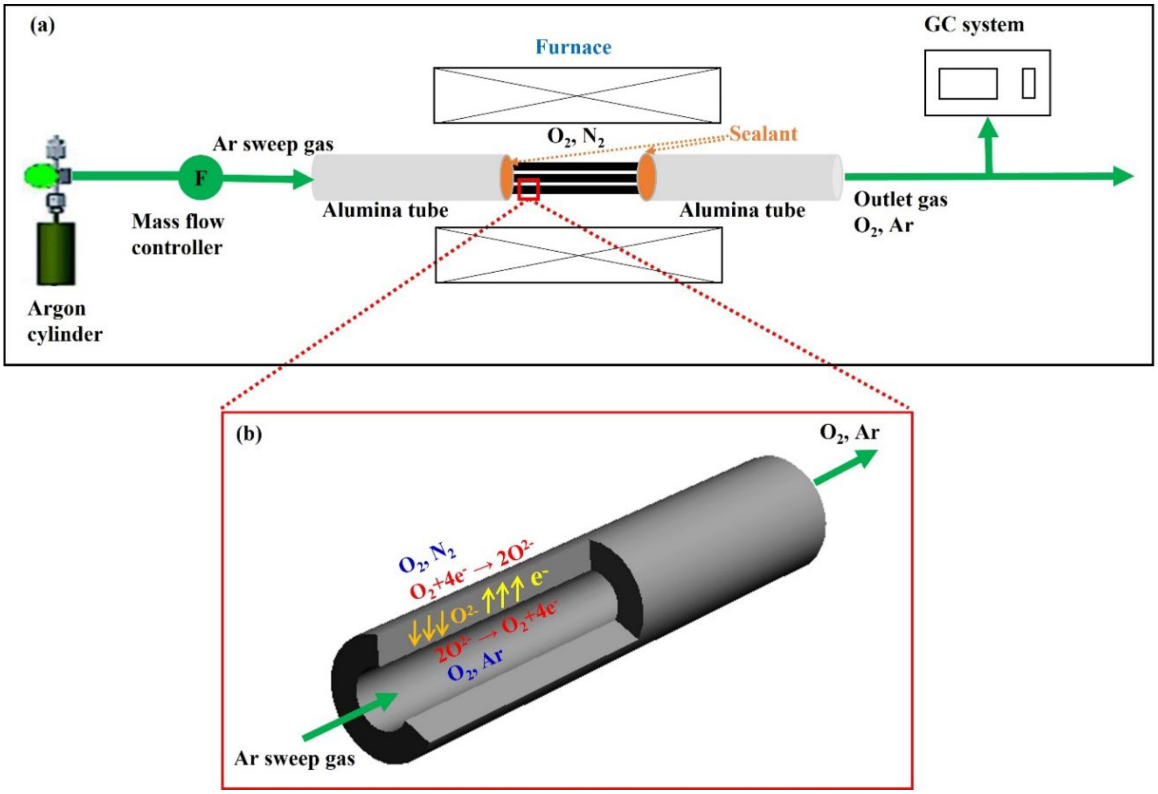

Figure 3.2 Schematic diagram of the stack test stand setup for oxygen separation performance measurement (a), Illustration of oxygen permeation process of the membrane (b).

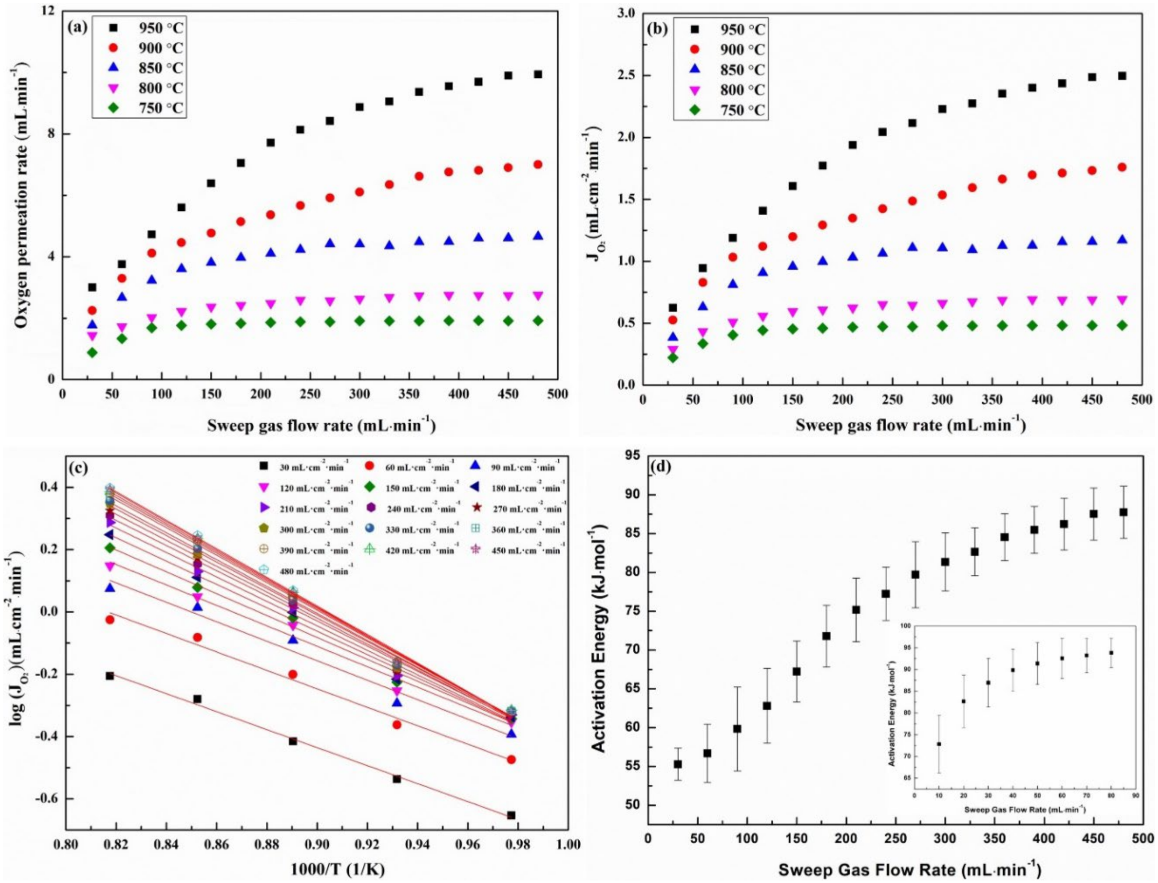

Figure 3.3 Oxygen permeation performance of the membrane stack; Oxygen permeation rate (a), Area normalized oxygen permeation flux (b), Arrhenius plot (c), and activation energy (d).

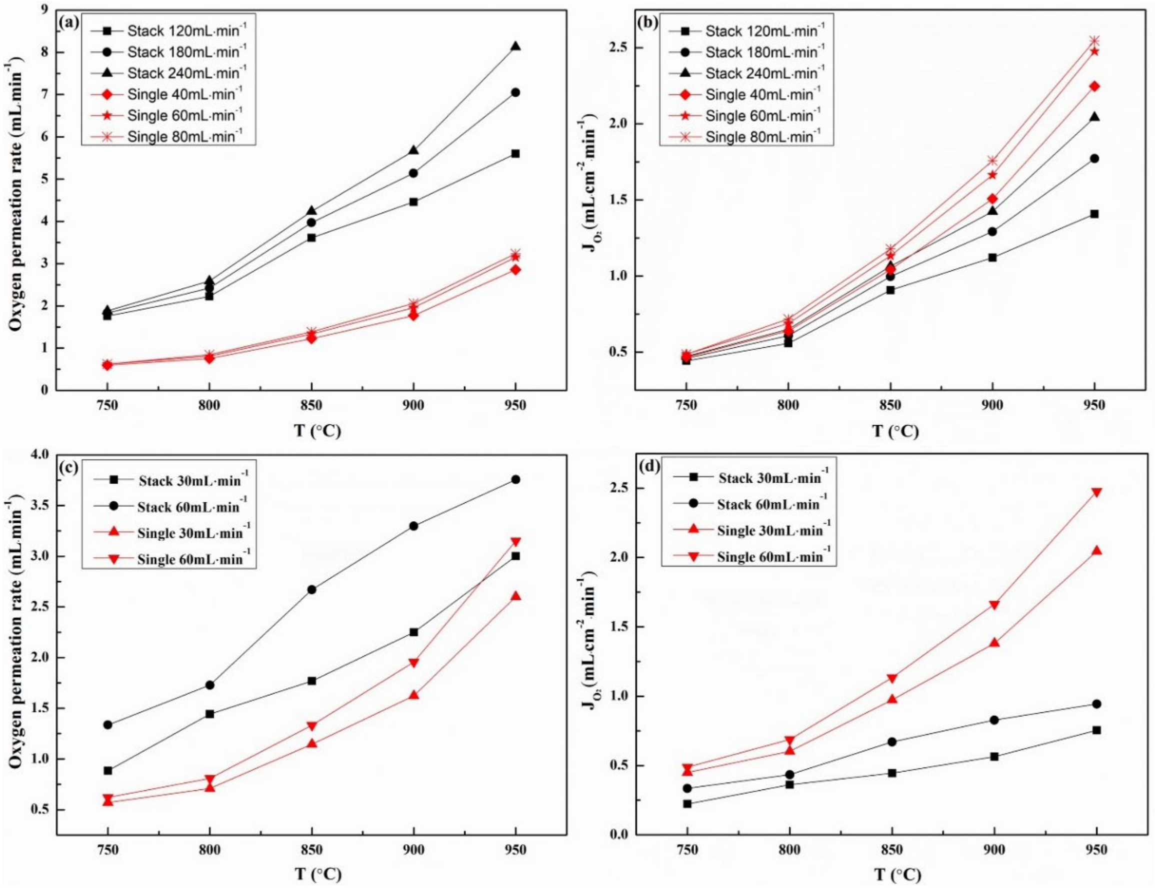

Figure 3.4 Comparison of the oxygen permeation rate (a, c) and oxygen permeation flux (b, d) of the membrane stack and the single membrane.

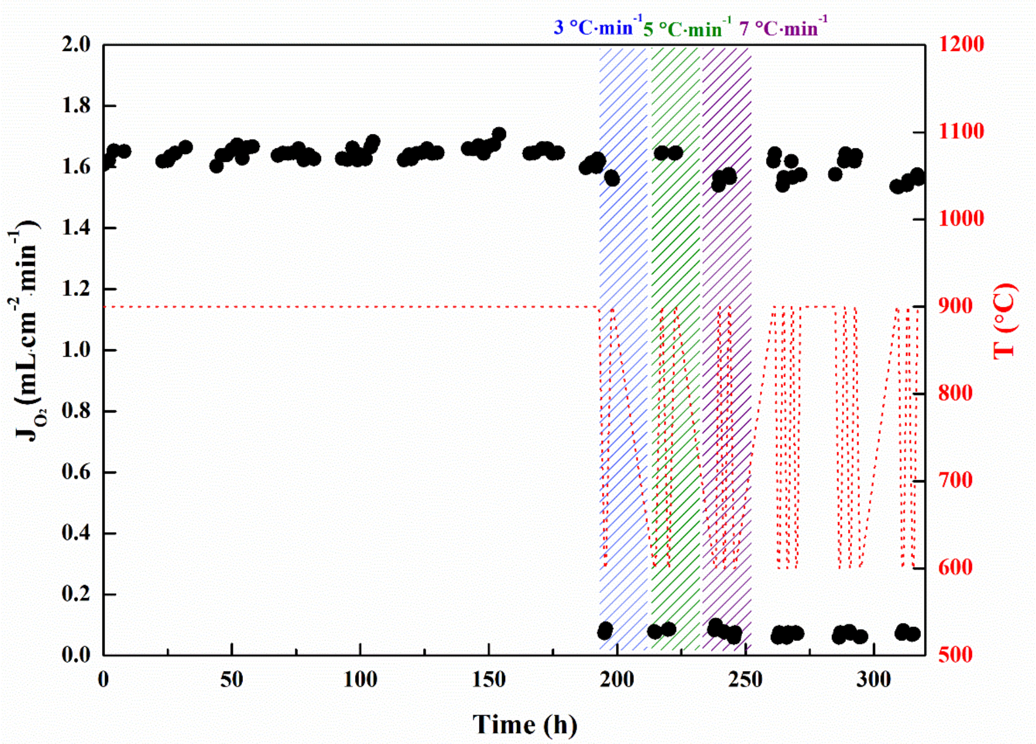

Figure 3.5 Performance of the membrane stack under long-term (~ 320 h) accelerated stability test.

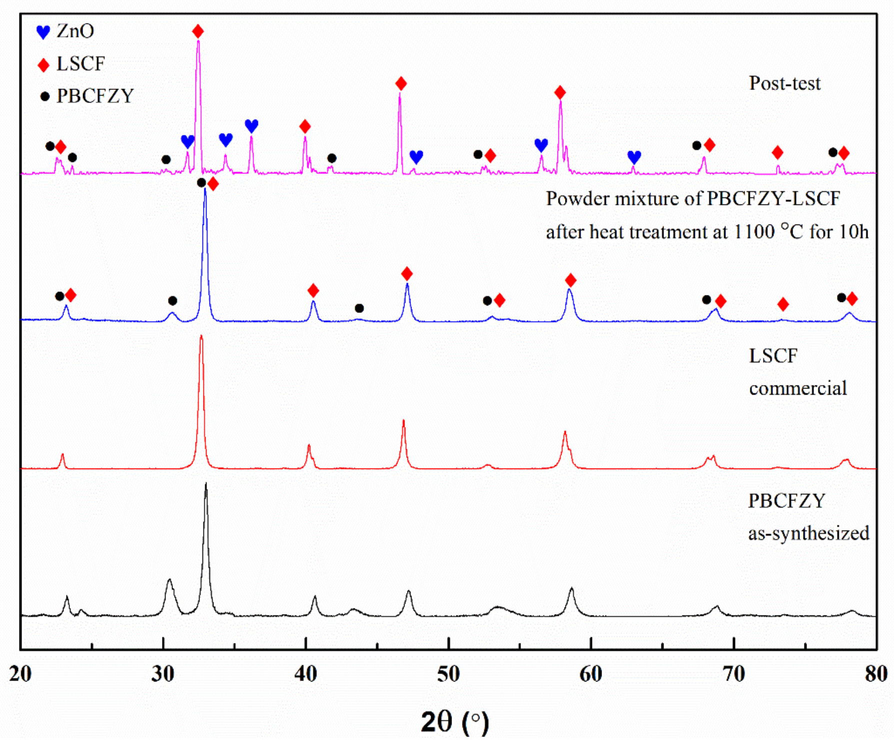

Figure 3.6 XRD pattern of the membrane after the long-term stability test.

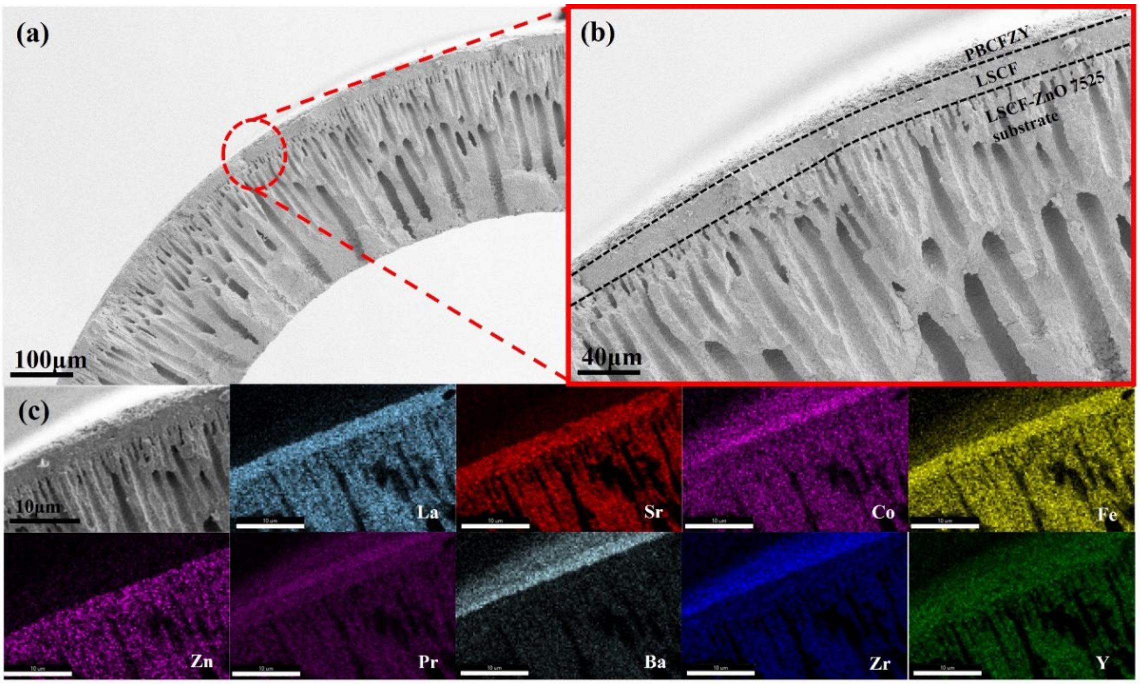

Figure 3.7 Cross sectional image of the membrane after stability test (a), Enlarged figure of local area marked with red circle in figure (a) (b), EDS image of the figure (b) (c).

CHAPTER 4

OXYGEN PERMEATION AND LONG-TERM STABILITY OF HOLLOW FIBER MEMBRANE STACK

4.1 Introduction

Ceramic based oxygen permeation membrane has demonstrated to be simple and cost-effective in producing highly pure oxygen among various developed air separation techniques [111-114]. The membrane normally employs mixed ionic and electronic conducting (MIEC) ceramic materials and separate oxygen from air directly driven by the oxygen partial pressure gradient across the gas-tight membrane at elevated temperature. Briefly, the whole oxygen permeation process could be divided into three parts: oxygen reduction reaction (ORR) at air feed side of the membrane, the transport of oxygen ions and electrons through the dense membrane, and the oxygen evolution reaction (OER) at permeated side. Therefore, the oxygen permeation flux of single membrane could be improved by ameliorate these three governing factors. Besides developing novel high performance membrane material, different membrane designs, typically planar and tubular ones have also been studied to enhance the oxygen permeation [115-119]. Micro-tubular type which has tubular diameter within millimeter or even sub-millimeter scale stands out among various membrane configurations for its distinct advantage, for example, high surface to volume ratio, short sealing length, dynamic /transient thermal stability etc. However, the manufacturing process of these ceramic capillaries, or the so-called hollow fibers is usually difficult [96, 120-122].

In the past few years, hollow fiber membranes have been widely fabricated by phase inversion spinning technique. After a few decades' development, hollow fiber which has a thin and dense function layer coated on a thick but porous substrate layer is also successfully obtained by adjusting the spinning parameters. Particularly, after high temperature sintering, a large number of featuring finger-like microchannels in the substrate absolutely favor the gas diffusion within the substrate thus enhancing the gas permeation across the membrane. For example, Ren et al. fabricated LSCF-GDC catalytic layer/ LSCF-GDC function layer/ LSCF-GDC micro-channeled support asymmetric membrane system by rational design and achieved an oxygen permeation of 1.02 $mL \cdot cm^{-2} \cdot min^{-1}$ at 850°C [77]. However, as most of membrane employ either mixed ionic electronic conducting perovskite materials or the composites of ionic and electronic conductors, the intrinsic brittleness of ceramics contribute to poor mechanical strength and insufficient stability for robust and durable operations of the membrane especially under harsh thermal cycling conditions. The tradeoff effect between permeability and stability makes the idea of improving the packing density of the membrane stack is more practical from engineering consideration. In addition, the small inner diameter of hollow fiber led to strong pressure drop along the length axis, thus limiting the fiber length which in turn needs a large number of fibers in a stack to reach a desired yield of permeated oxygen [67, 71, 100, 121, 123-124]. To improve the mechanical strength as well as obtaining stack functionality, An et al. [72] bundled five LSCF hollow fibers together with porous BSCF as binder which demonstrated high stability at high temperatures and good flux reproducibility when subjected to thermal cycles, while at a price of sacrificing the unique advantage of hollow fiber such as high effective surface area for ORR/OER.

Moreover, each of fiber in the stack requires sealing at high temperature which still remain as a major challenge. Tan et al. [69] used medium temperature sealant to bundle 7 fibers and build a module composing of 127 of such bundles. The so called 889 hollow fiber system deliver oxygen of 0.84 $L\cdot min^{-1}$ at 960°C for more than 1167h. But all the fibers close one end to mitigate the applied thermal stress during high temperature operation, and the effective surface area of the fiber is lost to avoid failure of silicone sealant which make the strategy not cost-effective.

Recently, our group has developed a novel design for robust and durable operation of oxygen permeation, namely LSCF-ZnO hollow fiber substrate/ LSCF dense function layer/ LSCF porous catalytic layer membrane system. By simply adding proper amount of ZnO into LSCF, the formed composite hollow fiber substrate provides excellent mechanical strength and robustness. The membrane system also employs silver and ceramic as sealant which produced oxygen permeation flux of ~2 $mL\cdot min^{-1}\cdot cm^{-2}$ at 900°C and degraded only 15% after 400h of test under harsh thermal cycling conditions [125]. The results provide a promising solution which may essentially overcome the issue associated with stability and high temperature sealing. In this paper, three above mentioned hollow fibers were bundled into a small stack using the same sealing strategy and the performance of the stack was systematically measured under different operating conditions. An accelerated long-term stability test was also conducted to evaluate its potential application in stacks in the future.

4.2 Experimental

4.2.1 Membrane stack assembly

The mixture of 75wt.% $La_{0.6}Sr_{0.4}Co_{0.2}Fe_{0.8}O_{3-\delta}$ (LSCF, Fuel cell materials, USA) and 25wt.% Zinc oxide (ZnO, 200 Mesh, Alfa Aesar, USA) which is simply denoted as LSCF-ZnO7525, were fabricated into hollow fiber substrates by spinneret spinning in combination with a modified phase inversion process using an in-house built spinning system. The dense LSCF thin-film functional layer was then prepared via dip-coating and sintering process. The detail information of the spinning system and dip-coting process were presented in the previous paper [126]. Afterwards, LSCF ink was prepared by thoroughly mixing the 60 wt.% of LSCF powder, 4 wt.% of ethyl cellulose and 36 wt.% of α-terpineol. The LSCF porous catalytic layer was later fabricated by brush painting the ink on the dense separation film twice, followed by calcinating at 1000 ℃ for 3h.

To construct membrane stack for evaluation, three fabricated hollow fiber membranes with an average length of 40~45mm were used. The photo of the fabricated LSCF-ZnO7525/LSCF dense functional layer/LSCF porous catalytic layer hollow fiber membrane is shown in Fig. 4.1(a). Fig. 4.1 (b) and (c) represent the cross section and the inner surface of the fabricated membrane respectively. Dense and crack free LSCF functional layer with a thickness of about 30μm showed intimate adhesion on the substrate, and the 5μm of porous LSCF catalytic layer attached to the dense LSCF functional layer. The LSCF-ZnO 7525 substrate showed porous microstructure with well aligned microchannels. Three of these membranes were connected and sealed to two supporting alumina tubes at either end respectively. In particular, the conductive adhesive ink (DAD-87, Shanghai Research Institute for Synthetic Resins, China) was first used to seal the connecting part, followed by aging at 900 °C in air for 30 min. The ceramic paste (Aremco Products Inc., USA) was then applied on the surface of the sealing part. After drying, alumina tube/hollow fiber membrane bundles/alumina tube assembly was heat-treated at 950 °C in air for 30 min to bond the sealing part for subsequent oxygen permeation measurement. The test assembly design and the photo of the practical test assembly were shown in Fig. 4.1(d). The exposed length of the membrane after sealing is about 20~22 mm and the resultant total area of the stack was 3.3 cm^2.

4.2.2 Stack performance evaluation

For oxygen permeation test, argon sweep gas was fed into the alumina supporting tube connected with membrane bundles while the shell side of bundle was exposed to ambient air. The operating temperature of the membrane bundle was controlled by a high temperature tube furnace (MTI, USA). The effluent gas from the bundle was sampled by a 5Å molecular sieve column and the concentrations of sampled gas species were analyzed using an online gas chromatography (GC-8A, Shimadzu, Japan). The whole testing setup for assembled stack and the oxygen permeation process are schematically illustrated in Fig. 4.2.

The oxygen permeation flux of the bundle is then determined using the measured species concentrations and Eqn. (1),

$$J_{O_2} = \frac{F(C_{O_2} - C_{N_2}(21/79))}{A} \qquad (1)$$

where J_{O_2} is the permeated oxygen flux of the membrane, A the effective area of the membrane, F the flow rate of the effluent gas, C_{O_2} the concentration of oxygen in the effluent gas, and C_{N_2} the concentration of nitrogen leaking into the sweep gas.

4.3 Results and Discussion

The oxygen permeation performance of the assembled bundle was evaluated in the temperature range of 950-750 °C with different argon sweep gas flow rates of 30-480 mL·min^{-1}, and the results are shown in Fig. 4.3. Fig. 4.3(a) represents the oxygen permeation rate, and the Fig. 4.3(b) is the oxygen permeation flux normalized by the membrane bundle area. The normalized oxygen flux reduced significantly from the oxygen permeation rate; this is due to the large membrane area of the bundle. It is obvious to see that the operating temperature increased from 750 to 950 °C, the oxygen permeation flux increased accordingly from 0.27 to 1.89 mL·cm^{-2}·min^{-1} with argon sweep gas flow rate at 480 mL·min^{-1}. The oxygen ion transport of the mixed ionic and electronic conductor is increased with elevated temperature, which is consisted with the permeation flux results. At fixed temperature, the oxygen permeation flux increased with the increased argon sweep gas flow rate. The change of the sweep gas flow rate directly affects to the oxygen partial pressure gradient across the membrane, the increasing sweep gas flow rate decreases the oxygen partial pressure at the lumen side, leading to the improving the oxygen permeation process. Specifically, at 950 °C, with the Ar sweep gas flow rate from 30 to 480 mL·min^{-1}, the oxygen permeation flux is increased from 0.54 to 1.89 mL·cm^{-2}·min^{-1}. However, change of the oxygen flux is slight at 800 and 750 °C (0.27 to 0.52 mL·cm^{-2}·min^{-1} at 800 °C and 0.15 to 0.27 mL·cm^{-2}·min^{-1} at 750 °C). Thus, it can be concluded that the oxygen surface exchange reactions and the bulk diffusion reaction are promoted by higher operating temperatures, and the operating temperature play more important role on permeation process than that of sweep gas flow rate. Fig. 4.3(c) and the Fig. 4.3(d) are Arrhenius plots derived from the oxygen permeation flux

(Fig. 4.3b) and the corresponding activation energies respectively. The activation energy of the membrane bundles showed (~ 100 kJ·mol^{-1}). The activation energy of the typical LSCF membrane from the open literature is also ~100 kJ·mol^{-1} [127], which is consistent with the membrane bundle in this work concluded that the oxygen permeation through the membrane bundle is functioned well.

To investigated scaling-up effect, Fig. 4.4 (a-b) compares the oxygen permeation rate and flux of the stack and the single membrane at the argon sweep gas flow rates of 40, 60, and 80 mL·min^{-1} per single membrane. To compare the oxygen permeation rate and flux at the similar sweep gas flow rate, the sweep gas flow rate in bundles was multiplied by number of membranes, which are 120, 180, 240 mL·min^{-1}. It is clearly to see that oxygen permeation rate increased with the increased number of membranes from single to three membranes. However, after normalized by area, oxygen flux showed lower in stack than single membrane due to the larger area of the stack. Fig. 4.4 (c-d) showed the comparison between the single membrane and the bundles at the same inlet Ar sweep gas flow rate (30 and 60 mL·min^{-1}) for further comparison. The oxygen permeation rate of the stack showed still higher, and the oxygen permeation flux of the stack showed lower than the single membrane. It is obvious to see that the oxygen permeation flux difference between the stack and the single membrane is larger than Fig. 4.4 (b). This is due to the different saturation point between the stack and the single membrane. For the single membrane, the oxygen permeation flux reached its saturation point at 80 mL·min^{-1} of Ar flow rate.

The oxygen partial pressure gradient is directly affected by the sweep gas flow rate. Stack has larger area, but the portion of the ambient air is same as the single membrane, so to reach the saturation point, the stack needs higher Ar sweep gas flow rate (~480 mL·min^{-1}). In this way, when compared the flux at 60 mL·min^{-1} sweep gas flow rate, the difference between the single membrane and the stack showed larger because the single membrane is almost reached its saturation point while the stack is far lower to reach its saturation point.

The stack was kept at argon sweep gas flow rate of 240 mL·min^{-1} to evaluate the performance stability and the result is shown in Fig. 4.5. Horizontal axis is time history, and the left vertical axis is corresponding oxygen permeation flux, and the right vertical axis represents applied thermal loads. First, the stack was kept at 900 ℃ for 192 h and the sampling time was 2 h during the daytime. During this time, the oxygen permeation flux of the stack showed stable performance. After 192 h, the thermal cycling stability of the stack was investigated by applied thermal loads between 900-600 ℃ with different cooling down and heating up rates. First, the stack was cooled down to 600 ℃ with 3 ℃·min^{-1} kept if 1 h and then heated back to 900 ℃ at the same rate and kept for 1 h. This cycle was repeated for 3 times and the rate changes to 5 and 7 ℃·min^{-1}, and these cycles also repeated for 3 times each. The oxygen permeation flux was tested every 30 min at each temperature for 94 h. After 9 cycles with 3 different rates, the rate was kept at 5 ℃·min^{-1} for 105 h, 11 cycles. The stack showed stable performance for 200h, and the performance decreased, but still maintained stable performance until the rest of the test.

Overall, the stack showed maximum degradation was 10.5% after long-term stability test for 411 h and 20 thermal cycles. XRD, SEM and EDS was carried out to characterize the post-test membrane sample. Fig. 4.6 shows the XRD pattern of the membrane sample before and after stability test. The main peaks are corresponded to LSCF and ZnO phase, and no impurities were detected, indicating great chemical stability of the membrane.

SEM and EDS of the post-test membrane samples are shown in Fig. 4.7. No obvious cracks in the substrate or coated layer, and no interdiffusions could be observed at the interfaces between the substrate and the functional layer after stability test, indicating the stable microstructure of the membrane. However, it is obvious to see that the coarsening of the LSCF layers. It is well known that LSCF has coarsening problem at high temperature especially because of Sr segregation [134], which consist with our EDS results of post-test sample. This Sr segregation may hinder the oxygen surface exchange process. The performance degradation can be explained by particle coarsening of LSCF at high temperature. Even though the performance degraded over the 411 hours of performance stability test, but it is reasonable to considered that the assembled stack in this work functioned well and the sealing method is feasible.

Table 1 compares the performance and the performance stability of the membrane stack using different hollow fiber membranes in open literature. Only few research efforts have been reported about long-term stability especially thermal loads. This work demonstrates not only high oxygen permeation flux but also longer performance stability and more thermal loads. By using LSCF-ZnO hollow fiber substrate, the fabricated membrane provides great mechanical strength and robustness. And the silver and ceramic paste can be used to sealing the membrane to stack, showed promising solution for the high temperature sealing. This could be the season of the high oxygen permeation flux and the stable performance. The results suggested the advantage of the LSCF-ZnO supported membrane stack developed and evaluated in this work.

4.4. Conclusion

In this work, the feasibility of oxygen permeation membrane stack assembly and the oxygen permeation performance such as oxygen permeation flux and stability of the assembled stack were studied. To improve the mechanical strength of the membrane, 75 wt.% LSCF- 25 wt.% ZnO composite substrate was used to fabricate membrane with the configuration of LSCF-ZnO 7525/LSCF dense functional layer/LSCF porous catalytic layer. To assemble the membrane into stack, silver and ceramic paste were used to seal both end of the membrane. These silver and ceramic paste can endure high temperatures which leads to stack placed in the high temperature without sacrifice any effective membrane area. The assembled stack showed high oxygen permeation flux. The stack tested for 411h including 20 thermal cycling conditions, showed 10.5% of maximum performance degradation. The assembled stack demonstrated very good oxygen permeation flux and stable performance. Overall, the stack showed the feasibility of assembly of stack including sealing for high temperature for oxygen permeation applications.

Table 4.1 Comparison of long-term stability of membrane stack in open literature.

Number of membranes	**Sealant**	**Assembly design**	**Oxygen permeation flux (mL·cm^{-2}·min^{-1})**	**Long-term hours (h)**	**Thermal loads (cycles)**	**Reference**
3LSCF	Ceramic paste/conductive adhesive ink	Individual with either end sealed	1.55	411	20	This work
7 BCBZ	BCBZ slurry	Bundle to single body with one dead end	2.77	60	4	[60]
7 LSCF	Silicone sealant	Bundle to single body with one dead end	1.54	260	None	[76]
5 LSCF	BSCF slurry	Bundle to single body	0.22	45	5	[72]

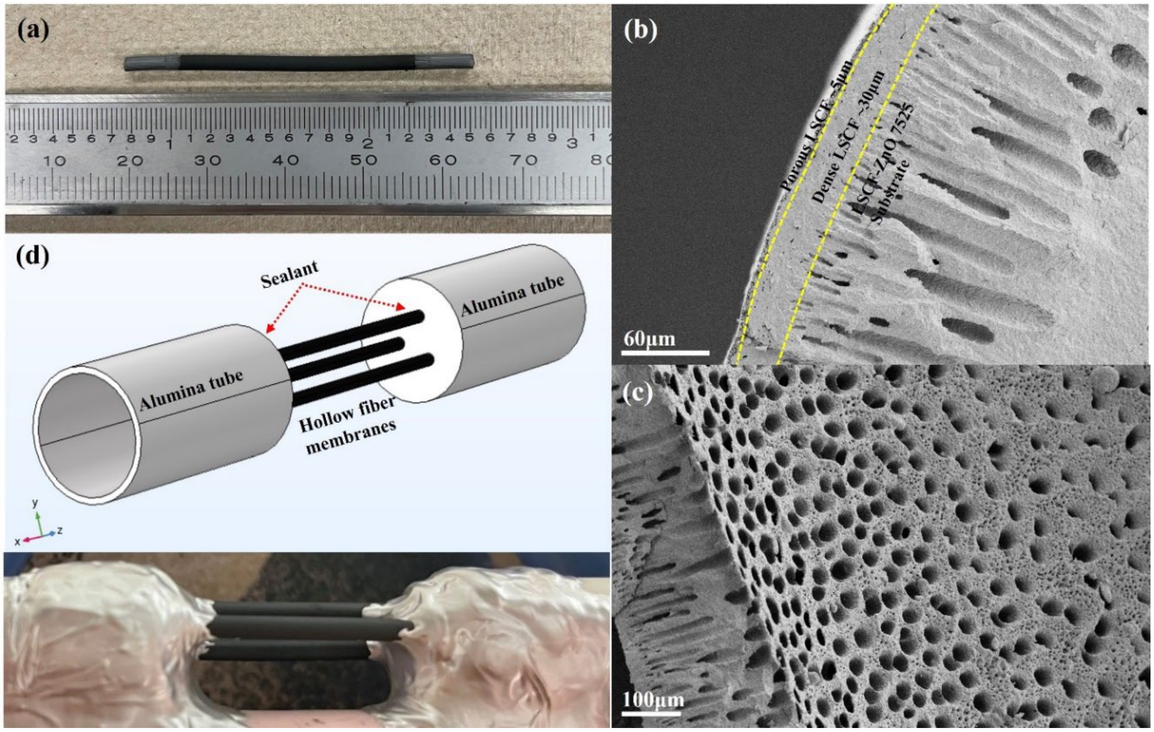

Figure 4.1(a) Photo of the fabricated LSCF-ZnO 7525/LSCF dense functional layer/LSCF porous catalytic layer membrane, (b-c) SEM image of the hollow fiber membrane; (b) Cross-sectional of the fabricated membrane, (c) Inner surface of the LSCF-ZnO 7525 substrate, (d) 3D design of the stack assembly, and the assembled stack test stand.

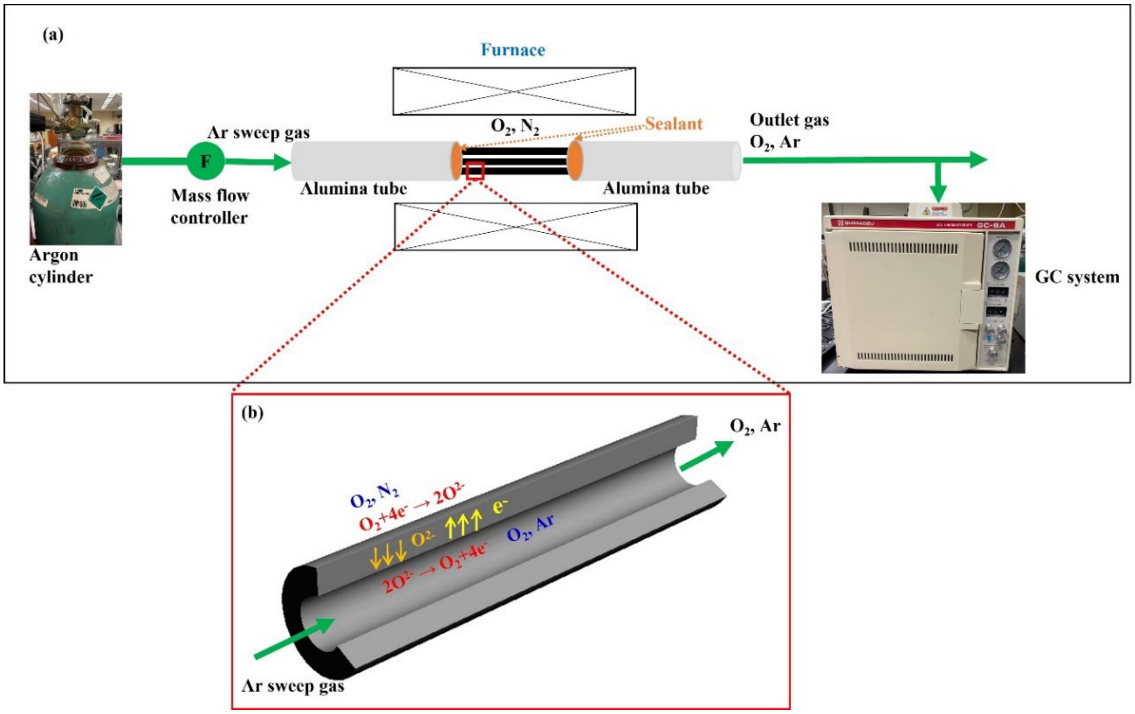

Figure 4.2 (a) Schematic diagram of the stack test stand setup for oxygen separation performance measurement, (b) Illustration of oxygen permeation process of the membrane.

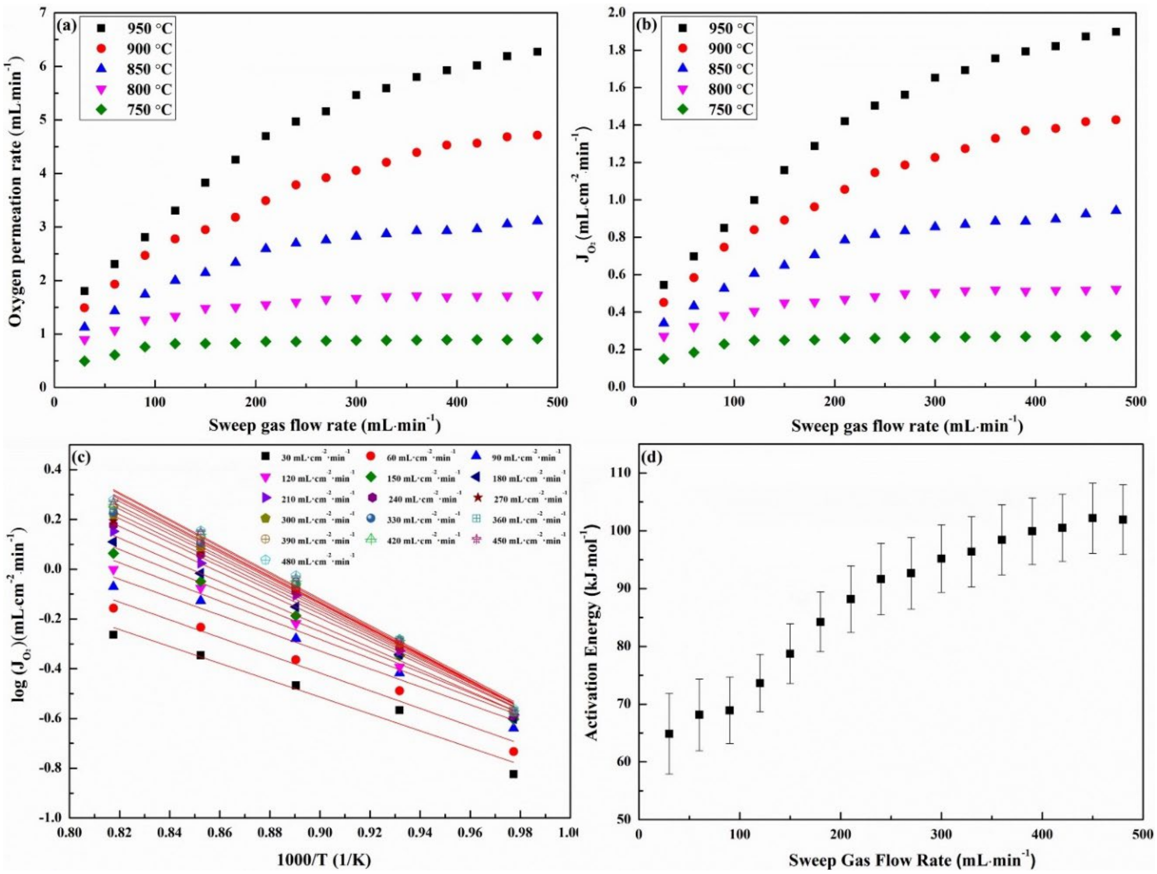

Figure 4.3 Oxygen permeation performance of the membrane stack (a) Oxygen permeation rate, (b) Area normalized oxygen permeation flux, (c) Arrhenius plot, and (d) Activation energy.

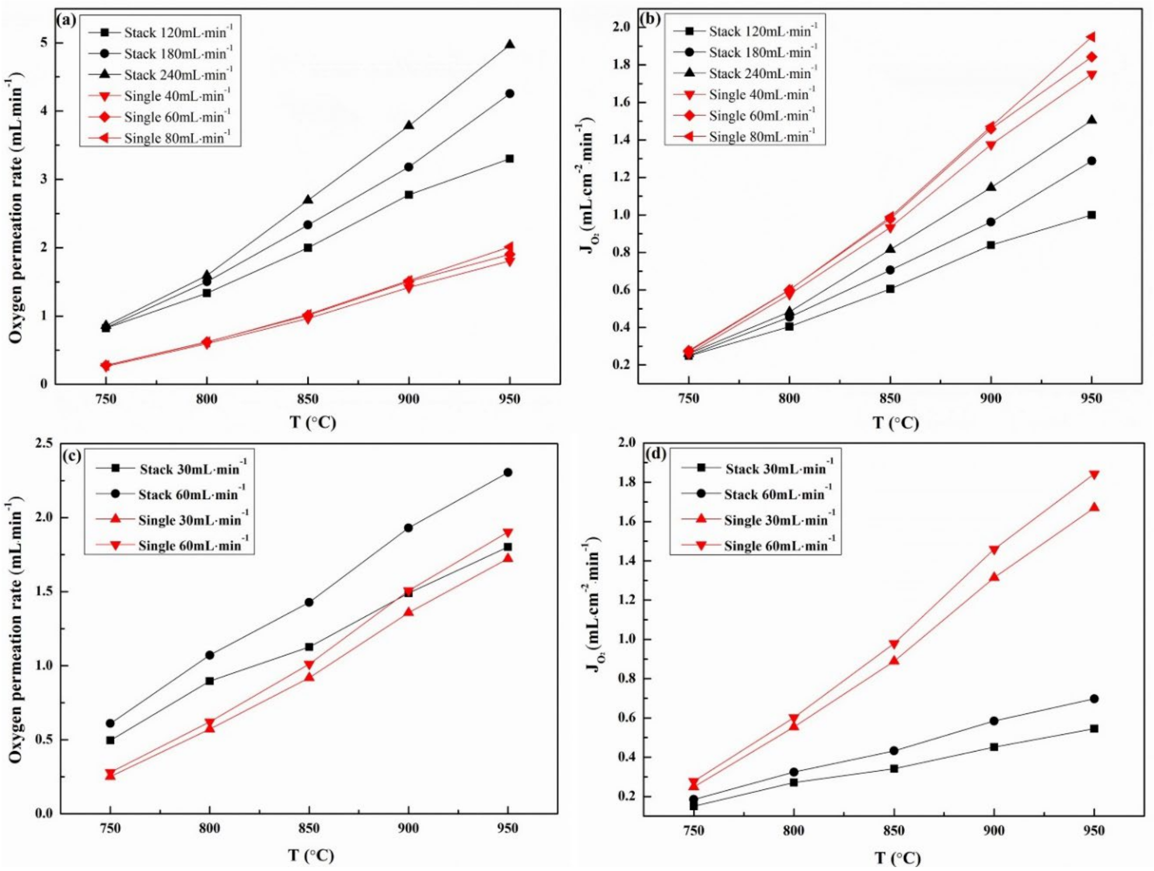

Figure 4.4 Comparison of the oxygen permeation rate (a, c) and oxygen permeation flux (b, d) of the membrane stack and the single membrane.

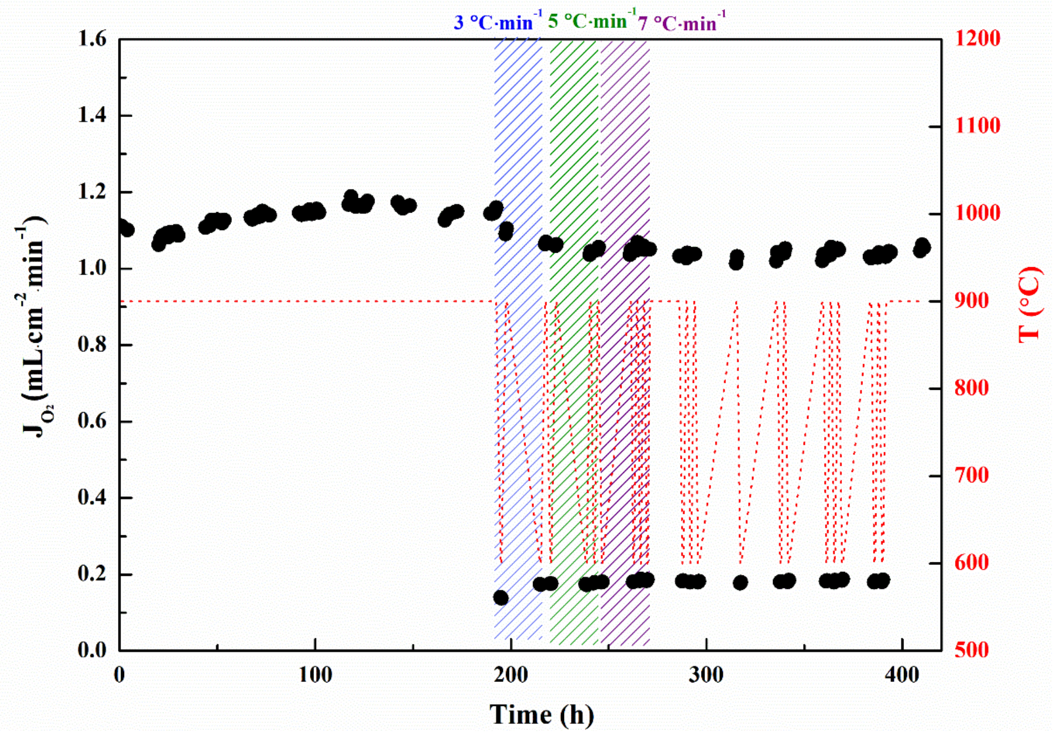

Figure 4.5 Performance of the membrane stack under long-term (~ 411 h) accelerated stability test.

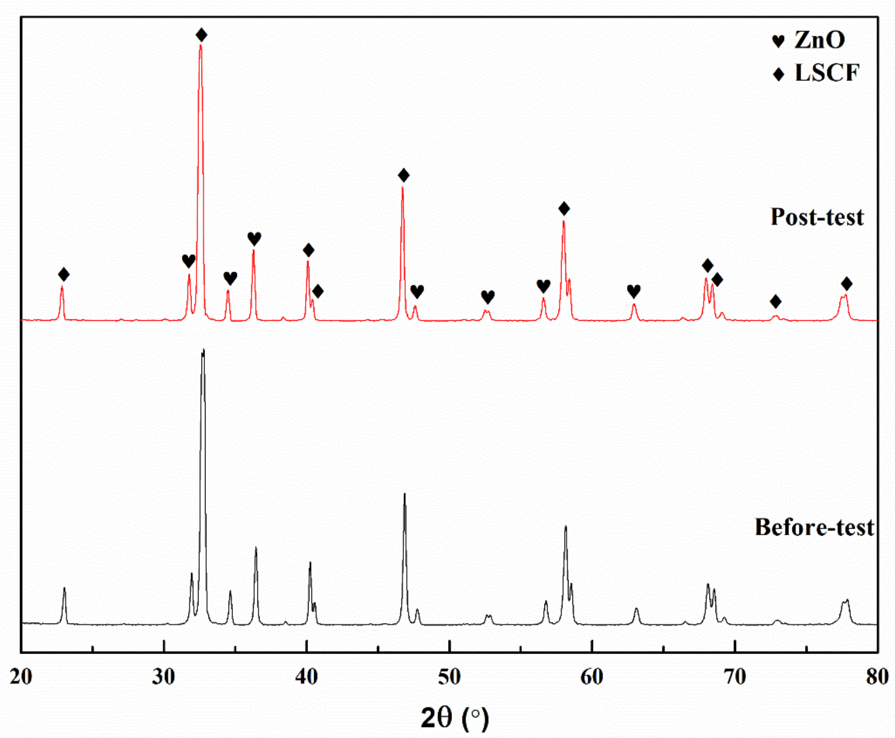

Figure 4.6 XRD pattern of the membrane after the long-term stability test.

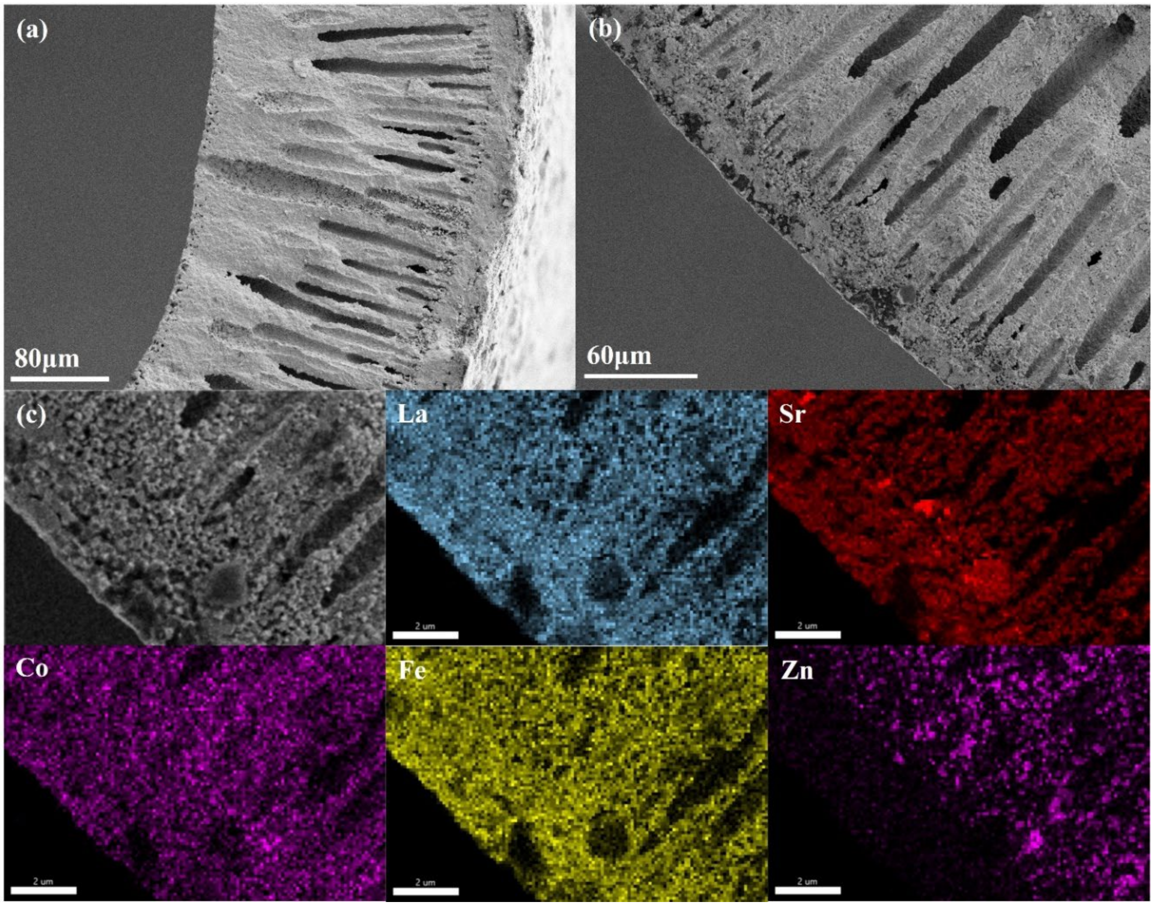

Figure 4.7 (a-b) Cross sectional image of the membrane after stability test, (c) EDS image of the figure (b).

CHAPTER 5

FABRICATION AND CHARACTERIZAION OF THIN-FILM SOFC SUPPORTED BY MICROCHANNEL-STRUCTRUED SUBSTRATE FOR DIRECT METHANE OPERATION

5.1 Introduction

Solid oxide fuel cell (SOFC) is an energy conversion device that converts chemical energy in fuels into electrical energy very efficiently and is environmentally friendly. SOFCs are fuel flexible that can use not only hydrogen but hydrocarbon fuels and even carbon [35, 128-130]. Direct hydrocarbon-fueled SOFCs may provide advantages of eliminating external reforming components for SOFC systems and using the existing infrastructures for the production, storage, and delivery of hydrocarbon fuels. These would improve system efficiency, reduce system cost, and facilitate practical applications of SOFC technologies. The state-of-the-art anode material is Ni-cermet, a composite of Ni and electrolyte material. The Ni phase is an electronic conductor and catalyst, while the electrolyte phase is an ionic conductor. The catalytic activity of Ni enables the reforming of hydrocarbon fuels for producing syngas, a mixture of H_2 and CO, through catalytic oxidation, such as steam reforming and CO_2 reforming as well as water-gas shift reaction. However, the high catalytic activity of Ni can also lead to the direct cracking of hydrocarbon compounds at high temperatures and CO hydrogenation as well as Boudouard reaction, causing carbon deposition in the anode. The carbon deposition, in turn, will deactivate active reaction sites, restrict gas flow, and damage microstructures, overall leading to severe degradations in anode performance and long-term stability [131-135]. Therefore, the carbon deposition issue in Ni-cermet anode electrode of hydrocarbon-fueled SOFCs has been a major barrier towards practical applications.

Significant efforts have been made to modify Ni-cermet anodes to improve their properties for carbon deposition resistance. These include surface modification and alloying of Ni-cermet with carbon-resistant metals and oxides, such as Cu, Sn, Ag, Ru, W, CeO_2, and their derivatives [28-29, 136-142]. Despite these modifications, it is generally realized that the carbon deposition issue is inevitable for Ni-based anodes due to the Ni-catalytic cracking of hydrocarbon fuels, especially in large-scale applications. Attempts have been made to develop Ni-free anode materials to circumvent the use of Ni-based anode. These typically include a class of perovskite- and layered perovskite-type of mixed ionic and electronic conducting oxides, such as $La_{0.75}Sr_{0.25}Cr_{0.5}Mn_{0.5}O_3$, $La_{1-x}Sr_xTiO_3$, $Sr_2Mg_{1-x}Mn_xMoO_{6-\delta}$, $PrBaMn_2O_{5+\delta}$, and their derivatives [31-32, 143-145]. Despite the fact that such materials demonstrated good properties as anodes for carbon deposition resistance, the power densities of corresponding SOFCs are usually much lower than Ni-cermet counterparts.

Further, complete conversion from hydrocarbon to syngas is hardly to achieve with such Ni-free anode materials. In this context, Ni-cermet is still a preferred anode material due to its high electronic conductivity and (electro)catalytic properties [24]. Another strategy to mitigate the carbon deposition issue is co-feeding a considerable amount of water with hydrocarbon fuels so that the oxygen to carbon ratio is maintained at a sufficiently high level in anode electrode. As a result, complete internal reforming of hydrocarbon fuels can be obtained. Meanwhile, it can also prevent Ni from being oxidized. However, too much water supply will dilute fuels in the anode, which in turn decreases open-circuit voltage and deteriorate the electrochemical performance of SOFCs. In this respect, precise control of operating temperature and oxygen to carbon ratio in the anode electrode may need much less water feeding. Nevertheless, the operation under precisely controlled thermodynamic conditions is possible but not practically feasible [146].

Recently, the concept of a diffusion barrier layer has been employed to increase diffusion resistance of hydrocarbon fuels into the anode functional layer and product gases (i.e., H_2O, CO_2) out of the anode functional layer. As a consequence, the concentration ratio of product gases to hydrocarbon fuel in the anode functional layer will be high enough to suppress carbon build up in the anode functional layer [147-149]. On the one hand, the diffusion barrier layer increases fuel/gas diffusion resistance and concentration polarization loss of the anode; on the other hand, the high concentration ratio of product gases to hydrocarbon fuel will dilute fuels in the anode functional layer. Both of the effects will deteriorate the electrochemical performance of SOFCs. Therefore, a trade off is needed between carbon deposition suppression and good electrochemical performance when the diffusion barrier layer is employed for anode electrodes. One strategy for such a trade off could be obtained through a synergistic combination of a diffusion barrier layer and suitable Ni-cermet anode material. The diffusion barrier layer is used to tune carbon/oxygen ratios without diluting fuels too much in the anode functional layer. This requires that the porous microstructure of barrier layers enable facile fuel/gas diffusions. The Ni-cermet anode material should possess sound oxygen storage and catalytic properties, enabling full electrochemical oxidization of fuel species. As a result, H_2O and CO_2 produced by full oxidization of fuel would suppress carbon build up through backward Boudouard reaction and hydrogenation.

Cerium oxide exhibits the property of releasing and incorporating oxygen [150, 151]. When aliovalent ions (divalent or tetravalent cations) are doped into ceria lattice, it may create oxygen vacancies by charge compensation mechanism, further improving oxygen storage capacity and catalytic property of ceria [152-154]. In this research, Zr and Sm were co-doped into ceria lattice and NiO – $Ce_{0.8-x}Sm_{0.2}Zr_xO_{2-\delta}$ (NiO:$Ce_{0.8-x}Sm_{0.2}Zr_xO_{2-\delta}$ = 50%:50% in weight; x=0, 0.05, 0.10, 0.15, and 0.20, or simply denoted as NiO-ZrxSDC) as anode materials were systematically studied. The Zrdoping level that minimizes polarization resistance of NiO-ZrxSDC anode was identified. A microtubular YSZ inert substrate was fabricated using an in-house built spinning extrusion system, featuring radially well-aligned microchannels open at the inner surface. Built upon the microtubular YSZ substrate and the identified NiO-Zr0.1SDC anode material, inert YSZ substrate supported cell of YSZ substrate/NiO/NiO-Zr0.1SDC/YSZ/$Ce_{0.8}Sm_{0.2}O_{1.9}$/$La_{0.6}Sr_{0.4}Co_{0.2}Fe_{0.8}O_{3-\delta}$ was fabricated through dip-coating and sintering process alternatively. The combination of such a cell design with NiO-Zr0.1SDC anode material is expected to suppress carbon deposition in the anode functional layer, thereby achieving stable electrochemical performance with hydrocarbon fuels.

5.2 Experimental

5.2.1 Material Synthesis

All the chemicals used in the experiments were purchased from Alfa Aesar and used as-purchased unless otherwise specified. The anode powdersof50% NiO – 50%$Ce_{0.8-x}Sm_{0.2}Zr_xO_{1.9}$ (NiO-ZrxSDC) in weight were synthesized by a urea combustion method in one pot. Particularly, stoichiometric amounts of $NiO(NO_3)_2{\cdot}6H_2O$(98.0% purity), $Ce(NO_3)_3{\cdot}6H_2O$ (99.5% purity), $Sm(NO_3)_3{\cdot}6H_2O$(99.9% purity), Zirconyl nitrate solution (99.0% purity), and urea ($CO(NH_2)_2$) (99.0-100.5% purity) were dissolved into deionized water to form a solution. The solution was magnetically stirred for 3hrs, followed by heating on a hot plate until self-ignited. After self-sustaining combustion, ash-like material was obtained. The obtained ash was subsequently ground for 24hrs in an ethanol medium using a ball milling process with zirconia balls. After drying, the ash was calcinated at 1000ºCintheair for 2hrs to form NiO-ZrxSDC phases. $La_{0.6}Sr_{0.4}Co_{0.2}Fe_{0.8}O_{3-\delta}$ (LSCF) powders were synthesized by a glycine nitrate process. Briefly, stoichiometric amounts of $La(NO_3)_3{\cdot}6H_2O$ (99.9% purity), $Sr(NO_3)_2$ (99.0% purity), $Co(NO_3)_3{\cdot}6H_2O$ (97.7%purity), $Fe(NO_3)_3{\cdot}9H_2O$ (98.0-101.0% purity) and glycine (99.5% purity) were dissolved into deionized water to form a solution. The solution was magnetically stirred for 3hrs followed by heating on a hot plate until combustion, resulting in ash-like material.

The obtained ash-like material was subsequently ground for 24hrs in ethanol medium using a ball milling process with zirconia balls. After drying, the ash was calcinated at 700ºC in the air for 2hrs to form the LSCF phase.

5.2.2 Symmetric Button Cell Preparation

The SDC powders (Fuel Cell Materials, USA) with the binder of 2% polyvinyl butyral in weight were mixed and ground in ethanol. After drying, the mixture of powder and binder was iso-statically cold-pressed at 600MPa to form an electrolyte substrate, resulting in a diameter of ~ 10mm and a thickness of ~1mm. The green electrolyte substrate was then sintered at 1450ºC in the air for 6hrs to form a dense SDC electrolyte. The surface of sintered SDC electrolyte substrate was mechanically polished using sand-papers and subsequently washed by anhydrous ethanol in an ultrasonic cleaner. The resulting thickness of SDC electrolyte substrates was about 400μm. 5% ethyl-cellulose (TCI, Japan)in weight was mixed with 95%α-terpineol(TCI, Japan) in weight to form an organic solution. The synthesized fine powders (NiO-ZrxSDC, 66.67% in weight) were then mixed with the organic solution(33.33% in weight) to form electrode inks. The electrode inks were screen-printed onto either side of the dense SDC electrolyte substrate.

After drying and aging, the electrode-electrolyte assembly was sintered at 1250ºC in the air for 2hrs to form symmetrical cell NiO-ZrxSDC | SDC | NiO-ZrxSDC. Silver wire was attached to either side of the symmetrical cells using silver paste (Heraeus 2807) as a current collector and external wires for further electrochemical measurement.

5.2.3 Single Microtubular Cell Fabrication

Microtubular YSZ inert substrate was first prepared. Briefly, polyethersulfone (PESf, Veradel 3000P, Solvay Specialty Polymers, USA; 3.5% in weight) and polyvinylpyrrolidone (PVP, K30, CP, Sinopharm Chemical Reagent Co., China; 0.5% in weight) were dissolved in N-methyl-2-pyrrolidone (NMP, HPLC grade, Sigma Aldrich, USA; 21% in weight) and ball-milled for 2hrs to form an organic mixture. Commercial

YSZ powder (Tape grade, Fuel Cell Material, USA; 75.0% in weight) was added into the organic mixture and ball-milled for 48hrs to form a homogeneous extrusion slurry. The as-prepared slurry was de-aired for 10 min and then loaded into an in-house build spinneret extrusion system to obtain green microtubular substrate. The extrusion system and related extrusion process were detailed elsewhere [61, 108-109]. The green substrate was sintered at 1100ºCin the air for 3hrs to achieve sufficient mechanical strength for subsequent functional layer coatings of NiO, NiO-Zr0.1SDC, YSZ, SDC, and LSCF sequentially. In particular, 0.4% ethyl cellulose and 99.6% ethanol in weight were mixed together to form an organic solution. 16.0% NiO (Fuel cell materials, USA) and 1.8% potato starch (J.T. Baker, USA) powders in weight were then mixed with the organic solvent to form a NiO slurry. The sintered YSZ microtubular substrates were sealed at both ends using PTFE films and vertically immersed into the prepared NiO slurry for 30 seconds. After drying in the air for 12hrs, the coated samples were calcinated at 600ºC in the air for 30min to burn out organics and bind the NiO layer onto the YSZ substrate. The preparation and coating of NiO-Zr0.1SDC slurry were similar to those of the NiO layer but calcined at 900ºC in air for 1hr. For YSZ electrolyte fabrication, 30% B73210 organic binder in weight (Ferro Electronics Materials, USA), 40% α-terpineol in weight, and 30% ethanol in weight were first mixed to form an organic slurry. 17% YSZ powders (Fuel cell materials, USA) in weight were then mixed with the organic slurry to form a YSZ slurry. The YSZ slurry was then dip-coated onto the NiO-Zr0.1SDC layer, followed by dip-coating a SDC layer in a similar way. After drying, the coated samples were sintered at 1400ºC in the air for 4hrs to form half-cells. Finally, the LSCF cathode layer was fabricated. Specifically, an organic slurry was first prepared by mixing 63.0% 2-butanone, 31.0% ethanol, 0.5% triethanolamine, 1.0% dibutyl phthalate, 1.0% polyethylene glycol 300 (ACROS, USA), and 3.5% butvar B-98 (Spectrum, USA) in weight. 10.0% LSCF powders were then mixed with the prepared organic slurry to form a LSCF cathode slurry. The LSCF cathode slurry was then dip-coated onto the half-cells. After drying, the coated samples were sintered at 950 ºC in the air for 2hrs to form a single microtubular cell of YSZ substrate/NiO/NiO-ZSDC/YSZ/SDC/LSCF. The resulting cathode area was about 0.3 cm^2. The silver paste was painted onto the cathode as a current collector. Silver wire was wound around the cathode and at either end of the anode substrate to serve as a current collector and external circuit.

5.2.4 Characterization and Electrochemical Measurements

The phase purity of the prepared powder materials was characterized and identified using the X-ray diffraction technique (XRD, D/MAX-3C) with Cu Kα radiation (λ=1.5406 Å) at room temperature with a scanning rate of 5^o min^{-1} in the range of $20^o \leq 2\theta \leq 80^o$. Microstructures of prepared samples and cells were characterized using scanning electron microscopy (SEM, Zeiss Ultra Plus FESEM, Germany). Microstructures and element distributions of prepared microtubular cells were also examined using SEM in combination with Energy-dispersive X-ray spectroscopy (EDS, Oxford Instruments detector).

The symmetrical cell prepared above was sealed in an alumina test chamber. A high-temperature tube furnace controlled the temperature of the chamber. The temperature of the furnace was increased from room temperature to 800ºC at a rate of 2ºC min^{-1} while nitrogen with the flow rate of 30ml min^{-1} was supplied into the alumina chamber. Once the furnace temperature reached 800ºC, the supplied gas was switched from nitrogen to humidified hydrogen (~3% H_2O, 30cm^3 min^{-1}). Under this condition, the experiment lasted for 3hrs, allowing the completion of NiO reduction to Ni in the electrodes. Electrochemical impedance spectra (EIS) of the symmetric cell were then measured using the Solartron1260/1297 electrochemical workstation. The EIS measurement was obtained from 800 to 600°C with a voltage perturbation of 10mV over the frequency range from 0.01Hz to 1MHz under open circuit voltage conditions.

The fabricated microtubular cell was electrochemically tested from 600 to 800°C. Both humidified hydrogen and methane were used as fuel, while ambient air was used as an oxidant. The surface of the cathode and anode electrode was coated with silver paste and encircled with silver wires as the current collectors. Ceramic paste (Aremco products, inc. USA) was used to seal and attach two alumina tubes to either end of the YSZ substrate of the cell. The procedure is detailed in the paper published elsewhere [61]. The temperature of the cell was controlled by a tube furnace (MTI, USA). Nitrogen gas was first supplied into the anode of the cell at room temperature. The cell was then heated up from room temperature to 800°C at the rate of 2°C min^{-1}. Once the cell temperature reached 800°C, the gas supplied to the anode was switched from nitrogen to humidified hydrogen (~3% H_2O). The flow rate of hydrogen was controlled at 30cm^3 min^{-1} using a precision flowmeter (APEX). The reduction of NiO current collector layer and NiO-Zr0.1SDC anode functional layer under this condition lasted for 3hrs before electrochemical testing. The voltage-current (V-I) curves and EIS were measured using a Solartron1260/1287 electrochemical workstation from 800 to 600°C. The EIS measurements were performed with a voltage perturbation of 10mV over the frequency range from 0.01Hz to 1MHz under open-circuit voltage conditions. Similarly, V-I curves and EIS of the cell were measured using methane as fuel with the flow rate of 30cm^3 min^{-1} in the temperature range of 600 – 800°C. A short-term stability test was also carried out with methane as fuel at an operating temperature of 700°C. The voltage of 0.7V was applied to the cell while the time history of current cell density was recorded.

5.3 Results and Discussion

5.3.1. Materials characterization

Fig. 5.1a shows the XRD patterns of the synthesized NiO-$Ce_{0.8-x}Sm_{0.2}Zr_xO_{2-\delta}$ (NiO-ZrxSDC, x= 0.05, 0.10, 0.15, and 0.20) powders. All characteristic diffraction peaks correspond to the NiO and ZrxSDC phases. No other phases could be detected, implying that Zr was totally dissolved into theSDC lattice. The XRD patterns further indicate very good chemical compatibility between NiO and ZrxSDC phases. Fig.1b shows the XRD patterns of the powders in the 2θ range of 54-58°. It can be seen that the peak was shifted to the higher angles with increasing Zr dopant contents from 0.05% mol to 0.20% mol, indicating the decrease of lattice volume. Since the atomic radius of Zr^{4+} (80Å) is smaller than that of Ce^{4+} (90Å), the Zr doping leads to the decreased lattice parameter.

Fig. 5.2 shows SEM images of the synthesized NiO-ZrxSDC powders. The powders consisted of fine and homogeneous particles with certain agglomerations. The average size of agglomerations is about 545nm. It seems that the agglomerations become weaker beyond the Zr doping level of 0.05.

5.3.2. Symmetry cells

Fig. 5.3 shows the polarization resistances (R_p) values of the symmetrical cells Ni-ZrxSDC|SDC|Ni-ZrxSDC(x = 0, 0.05, 0.10, 0.15, and 0.20) measured in humidified hydrogen at the temperatures of 600 – 800°C. The R_p values of different Zr doping levels at different temperatures were obtained from the equivalent circuit technique fitting from the EIS curves. The obtained R_p values werethen corrected by the electrode area and divided by two due to the symmetrical configuration of the cell. It can be seen that the polarization resistance tended to decrease with increasingZr doping level in the range of 0 to 0.1%mol at every operating temperature. Beyond 0.1%mol,the polarization resistance increased with increasing Zr dopant. The Ni-Zr0.1SDC electrode obtained the minimum polarization resistance among different Zr doping levels. In what follows, NiO-Zr0.1SDC will be used as anode material to fabricate microtubular YSZ inert substrate-supported single cell for electrochemical performance study.

5.3.3. Single-cell performances

Fig. 5.4 shows a cross-sectional SEM image of the fabricated microtubular cell YSZ substrate/NiO/NiO-Zr0.1SDC/YSZ/SDC/LSCF. It can be seen that radially well-aligned microchannels were embedded in the thick YSZ substrate, which is open at the inner surface (Fig. 5.4a). Multiple functional layers can also be observed on the thick YSZ substrate, including ~3µm NiO current collector layer, ~4µm NiO-Zr0.1SDC anode functional layer, ~10µm YSZ electrolyte layer, ~5µm SDC buffer layer, and ~10µm LSCF cathode layer (Fig. 5.4b). Intimate adhesions were obtained between different layers. The YSZ electrolyte layer is very dense. The SDC layer contains closed pores but is good enough as a buffer layer to separate the YSZ electrolyte layer from the LSCF cathode layer, which allows avoiding chemical reactions between YSZ and LSCF at elevated temperatures. The NiO layers and NiO-Zr0.1SDC exhibited porous microstructure features, and the porosity would be further improved in these two layers after NiO is reduced to Ni.

To examine the quality of the fabricated cell in a comprehensive manner, a benchmark test was first carried out. Before the test, the NiO current collector and NiO-Zr0.1SDC anode functional layer were first reduced. In particular, nitrogen with the flow rate of 30cm^3 min^{-1} was supplied to the anode side while the cell was heated up by a tube furnace. When the cell temperature reached 800ºC, the supplied nitrogen was switched to humidified hydrogen with a flow rate of 30cm^3 min^{-1}. The experiment under this condition was lasted for 3hrs, allowing for the completion of NiO reduction. The electrochemical performance of the cell was then measured in the temperature range of 800 – 600ºC, with the cathode electrode being exposed to ambient air. Fig. 5.5a shows the corresponding voltage-current (V-I) curves and power density (P-I) curves. The OCVs of 1.01 to 0.94V were obtained at the temperature range of 600 – 800ºC. These values are close to the theoretical Nernst potentials (e.g., ~1.10V) when YSZ is employed as electrolyte material, indicating that the YSZ electrolyte is dense and the rest of the cell components functioned well. The results further imply that the process for cell fabrication is reliable. The peak power density of the cell reached about 204, 272, 385, 500, and 602mWcm^{-2} at 600, 650, 700, 750, and 800ºC, respectively. The EIS curves of the cell measured at OCV conditions are shown in Fig. 5.5b. Using equivalent circuit and curve-fitting technique, the ohmic resistance (R_{ohm}) and polarization resistance (R_p) of the cell were obtained from EIS curves and listed in Table 5.1. As one can see that with increasing the operating temperature from 600 to 800ºC, the cell R_{ohm} decreased from 0.93 to 0.25Ω cm^2 while the cell R_p decreased from 1.12 to 0.23 Ω cm^2, respectively. The $R_{ohm}$is contributed by electrolyte and the skeleton of porous anode and cathode electrode as well as associated current collectors. The increasing temperature would directly reduce ohmic resistances of YSZ electrolyte and Ni-Zr0.1SDC anode as well as LSCF cathode skeletons; therefore, the cell R_{ohm} decreased. Similarly, higher temperatures would enhance the electrochemical kinetic properties of both anode and cathode electrodes, including surface exchange coefficients and bulk diffusivities. Accordingly, the cell R_p decreased. Overall, the benchmark test results indicate that the cell obtained reasonably good electrochemical performance, confirming that the cell fabrication process is reliable.

The electrochemical performance of the fabricated cell fueled with methane is then tested. The effectiveness of a synergistic combination of Ni-Zr0.1SDC anode material and cell architecture for suppression of carbon deposition is further examined. Shown in Fig. 5.6a are V-I curves and P-I curves of the cell directly fueled with methane in the temperature range of 600 – 800°C. The cell obtained OCVs of 1.02, 1.01, 1.00, 0.98, and 0.967V and peak power densities of 173, 259, 327, 384, and 456mW·cm^{-2} at the temperatures of 600, 650, 700, 750, and 800°C, respectively. Fig. 5.6b shows the EIS curves of the cell under open-circuit voltage conditions. Using equivalent circuit and curve-fitting technique, the cell ohmic resistance (R_{ohm}) and polarization resistance (R_p) were obtained from the measured EIS curves. The results are summarized in Table 5.2. In particular, the ohmic resistance of 0.45, 0.52, 1.05, 1.57, and 1.98 Ω cm^2 and the polarization resistance of 0.47, 0.51, 0.89, 1.23, and 1.43 Ωcm^2 were obtained at the temperatures of 600, 650, 700, 750, and 800°C, respectively.

To examine the stability of the cell directly fueled with methane, a short-term durability test was carried out. The temperature of the cell was controlled at 700°C. The voltage of 0.7V was applied to the cell while the current of the cell was monitored. Under these conditions, the experiment was run for about 26hrs. The history of current cell density is shown in Fig. 5.7. It is obvious to see that the current density of the cell was very stable, performance degradations could not be observed. It is noteworthy that methane-fueled YSZ inert substrate-supported SOFC has been studied in the open literature [155], where Ni-SDC was used as anode functional layer material, and the porosity of YSZ substrate was randomly distributed without any radially well-aligned microchannels. Nevertheless, the corresponding cell showed a voltage loss of 9% during short-term stability of 13 h at 700°C in methane. Comparing our results mentioned above with those in [155], it seems to indicate that the combination of Zr doped SDC anode material and YSZ inert substrate embedded with radially well-aligned microchannels is able to effectively improve the performance stability of the cell directly fueled with methane. After the short-term durability test, the cell was further characterized. Shown in Fig. 5.8a is the cross-sectional SEM image of the post-test microtubular cell ranging from part of the YSZ substrate to part of the dense YSZ electrolyte.

The radially well-aligned microchannels in the YSZ substrate still can be observed. The Ni current collector layer and Ni-Zr0.1SDC anode functional layer can be identified and show intimate contact with one another. Further EDS analysis indicates that Ni elements are mainly confined within the Ni-current collector layer and Ni-Zr0.1SDC anode functional layer (Fig. 5.8b). Zr elements are mainly located in the substrate and YSZ electrolyte layer (Fig. 5.8d). Interestingly, C elements were primarily located in the substrate (Fig. 5.8c). Quantitative line EDS analysis (Fig. 5.8e) indicates that some carbon elements could still be detected in the Ni current collector layer but not in the Ni-Zr0.1SDC anode functional layer. It is noteworthy that such a Ni current collector region is directly connected to a microchannel in the substrate, whereby methane diffusion to the current collector is relatively easy.

To understand the mechanisms and reactions in the anode and the prevention of carbon deposition in the anode functional layer, the experimental data mentioned above is further compared and interpreted from a theoretical point of view. When methane is employed as fuel for Ni-cermet anode, very complicated chemical/electrochemical reactions would take place. These could include the steam reforming reaction of CH_4, the dry (CO_2) reforming reaction of CH_4, and water gas shift reaction, as shown below, respectively,

Steam reforming reaction: $\mathrm{CH_4 + H_2O \leftrightarrow CO + 3H_2}$ (1)

Dry reforming reaction: $\mathrm{CH_4 + CO_2 \leftrightarrow 2CO + 2H_2}$ (2)

Water-gas shift reaction: $\mathrm{CO + H_2O \leftrightarrow CO_2 + H_2}$ (3)

As a result, the fuel species of H_2 and CO are generated from these three reactions, meanwhile CO_2 is produced from the water gas shift reaction. Electrochemical oxidations of fuel speciesCH_4, H_2, and COwould then take place at triple phase boundaries (TPBs) in the anode functional layerby using oxygen ions released from theZr0.1SDC phase. Depending on the amount of CH_4 and oxygen ion (O^{2-}) available at TPB sites, both full and partial electrochemical oxidations could occur, specifically,

Full oxidation of CH_4: $\mathrm{CH_4 + 4O^{2-} \rightarrow CO_2 + 2H_2O + 8e^-}$ (4)

Partial oxidation of CH_4:$\mathrm{CH_4 + O^{2-} \rightarrow CO + 2H_2 + 2e^-}$ (5)

$\mathrm{H_2 + O^{2-} \rightarrow H_2O + 2e^-}$ (6)

$\mathrm{CO + O^{2-} \rightarrow CO_2 + 2e^-}$ (7)

According to the Nernst potential equation, the OCV of the cell is dependent on the partial pressures of oxidant at the cathode side and fuels at the anode side. Since three fuel species of CH_4, H_2, and CO directly involved in electrochemical oxidations through the reactions of (4) – (7), the OCV of the cell would be determined by these four reactions in a combinational way. Theoretically, it has been demonstrated that the OCVs for electrochemical oxidations of H_2 and CO, and the full electrochemical oxidation of CH_4 decrease with increasing operating temperatures while that for partial electrochemical oxidation of CH_4 increases distinctly [156]. As demonstrated above, the OCVs of the cell fueled with H_2 decreased from 1.01 to 0.94 V when the temperature was increased from 600 to 800ºC, which is consistent with the theoretical predictions. With CH_4 as fuel, the OCVs of the cell decreased from 1.02 to 0.967 V with increasing the temperature from 600 to 800ºC. This observation indicates that the OCVs contributed by the full electrochemical oxidations of CH_4, H_2, and CO outperformed the contribution from the partial electrochemical oxidation of CH_4, and the latter is not a dominant reaction in the anode. As mentioned above, the type of electrochemical oxidations of CH_4 is dependent on the concentrations of gas species CH_4 and oxygen ion (O^{2-}) at TPB sites.

According to the reactions (4) and (5), when CH_4 concentration is relatively low while that of mobile O^{2-} near the TPB sites are relatively high, the full oxidation of CH_4 would occur; in other extreme situations of high CH_4 concentration and low concentration of mobile O^{2-}, the partial oxidation of CH_4 could take place. We have experimentally demonstrated that the microtubular substrate with radially well-aligned microchannels facilitates facile gas diffusion and is able to obtain very high gas permeability [61, 109]. Accordingly, sufficiently high CH_4 concentration would be maintained in the anode functional layer. Since the full oxidation of CH_4 in combination with the oxidations of H_2, and CO outperformed the partial oxidation of CH_4 in the anode functional layer, as demonstrated by the OCVs of the cell, it is reasonable to assume that sufficient oxygen ions are available for these reactions at the TPBs in the anode functional layer. This indicates the good oxygen storage capacity and catalytic property of the Zr0.1SDC phase, which is consistent with the above understanding of Zr doped SDC material.

When CH_4 is directly utilized as fuel for SOFCs, carbon could be generated through three reactions, including direct cracking of CH_4, Boudouard reaction, and hydrogenation, in particular,

Direct cracking of CH_4: $CH_4 \leftrightarrow 2H_2 + C$ (8)

Boudouard reaction: $2CO \leftrightarrow CO_2 + C$ (9)

Hydrogenation: $CO + H_2 \leftrightarrow H_2O + C$ (10)

The reaction of CH_4 direct cracking is usually obtained byNi's excellent catalytic activity. For the studied microtubularcell, the Ni phase is confined within the thin Ni current collector layer and Ni-Zr0.1SDC anode functional layer. Since H_2O and CO_2areproduced onlyin the thin anode functional layer through electrochemical oxidization of fuels, which facilitates the reforming reactions of $CH_4$and water gas shift reaction, it is less likely for directCH_4cracking(reaction (8)) to occur in the thin Ni-containing layers. Therefore, carbon could be produced only through the Boudouard reaction (9) and hydrogenation (10). When the concentrations of H_2O and CO_2 arerelatively high, which is usually the case in the thin anode functional layer, the backward reactions of (9) and (10) would be favored. As a result, carbon accumulation would be inhibited in the anode functional layer. This could be why the cell demonstrated very stable performance in the short-term test when directly fueled with methane. Depending on various species concentrations, the forward Boudouard reaction and hydrogenation could still occur in the YSZ microstructure substrate, and carbon could be built up in the substrate and current collector region near microchannels. This understanding is also consistent with the above EDS results of carbon element distribution.

5.4 Conclusions

A family of NiO 50%-Ce0.8-xSm0.2ZrxO2-δ50% in weight (x = 0.0, 0.05, 0.10, 0.15, 0.20) anode composite powders were successfully synthesized using urea combustion method in one pot. The Zr doping effects were systematically studied using symmetric cells in a reducing atmosphere at elevated temperatures. The Zr doping level of x = 0.1 that minimizes the anodic polarization resistance of the composite anode was identified. Microtubular YSZ substrate was fabricated using an in-house built spinning extrusion system, featuring radially well-aligned microchannels open at the substrate inner surface. Built upon the fabrication of thick YSZ substrate, thin layers of NiO current collector, NiO-Zr0.1SDC anode, YSZ/SDC electrolyte, and LSCF cathode were sequentially fabricated through dip-coating/sintering process alternatively, forming a microtubular cell of YSZ substrate/NiO/NiO-Zr0.1SDC/YSZ/SDC/LSCF. The cell exhibited the peak power densities of 602 and 456mWcm^{-2} at 800℃ when ambient air was used as an oxidant, and humidified hydrogen and methane were used as fuel, respectively. The cell also exhibited very good performance stability in the26hrs short-term durability test at 700ºC near the condition of peak power density output when directly fueled with methane. The capability of carbon deposition prevention was achieved through a synergistic combination of oxygen storage and catalytic properties of the Zr0.1SDC phase in the anode functional layer and novel architecture design of the cell. The fundamental mechanisms for carbon suppression are analyzed.

Table 5.1 Open circuit voltage (OCV), ohmic resistance (R_{ohm}), polarization resistance (R_p), maximum power density (MPD) of the single cell in hydrogen at different temperatures.

Temperature / °C	800	750	700	650	600
OCV / V	0.94	0.96	0.988	1.00	1.01
MPD / mWcm^{-2}	602	500	385	272	204
$_{ohm}$ / Ω cm^2	0.25	0.46	0.71	0.82	0.93
R_p / Ω cm^2	0.23	0.45	0.67	0.94	1.12

Table 5.2 Open circuit voltage (OCV), ohmic resistance (R_{ohm}), polarization resistance (R_p), maximum power density (MPD) of the single cell in methane at different temperatures.

Temperature / °C	800	750	700	650	600
OCV / V	0.967	0.98	1.00	1.01	1.02
MPD / $mWcm^{-2}$	456	384	327	259	173
R_{ohm} / Ω cm^2	0.45	0.52	1.05	1.57	1.98
R_p / Ω cm^2	0.47	0.51	0.89	1.23	1.43

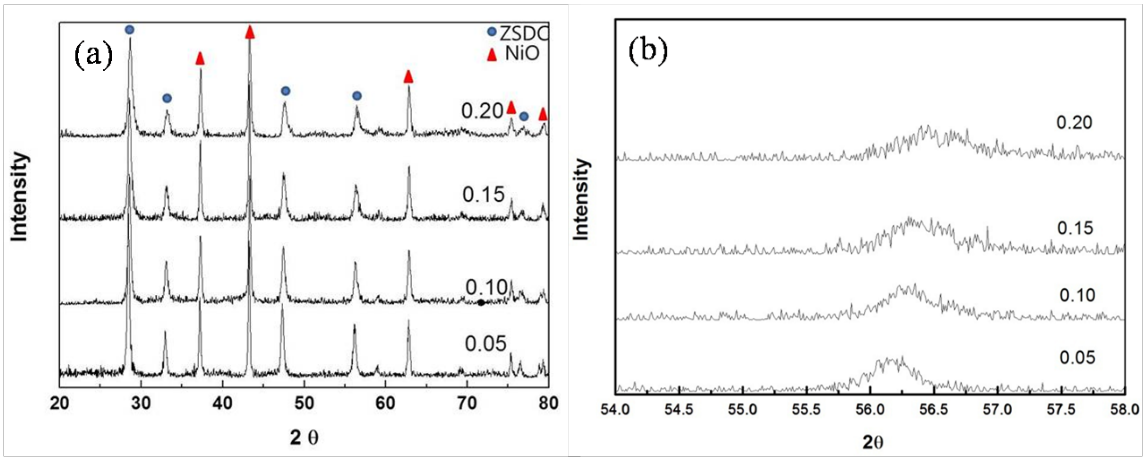

Figure 5.1(a) XRD patterns of synthesized NiO-ZrxSDC powders in the 2θ range of 20-80°. (b) XRD patterns of the powders in the 2θ range of 54-58°.

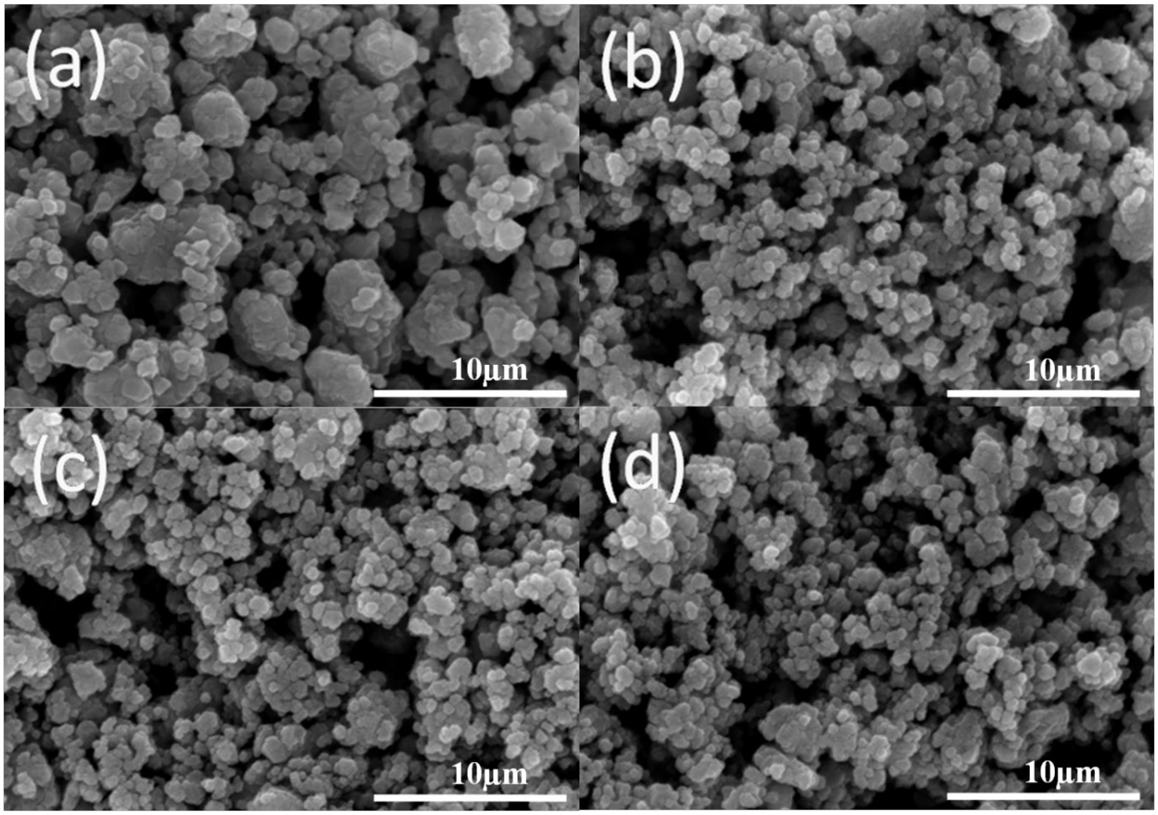

Figure 5.2 SEM images of the synthesized NiO-ZrxSDC powders. (a) x=0.05, (b) x= 0.10, (c) x= 0.15 and (d) x= 0.20.

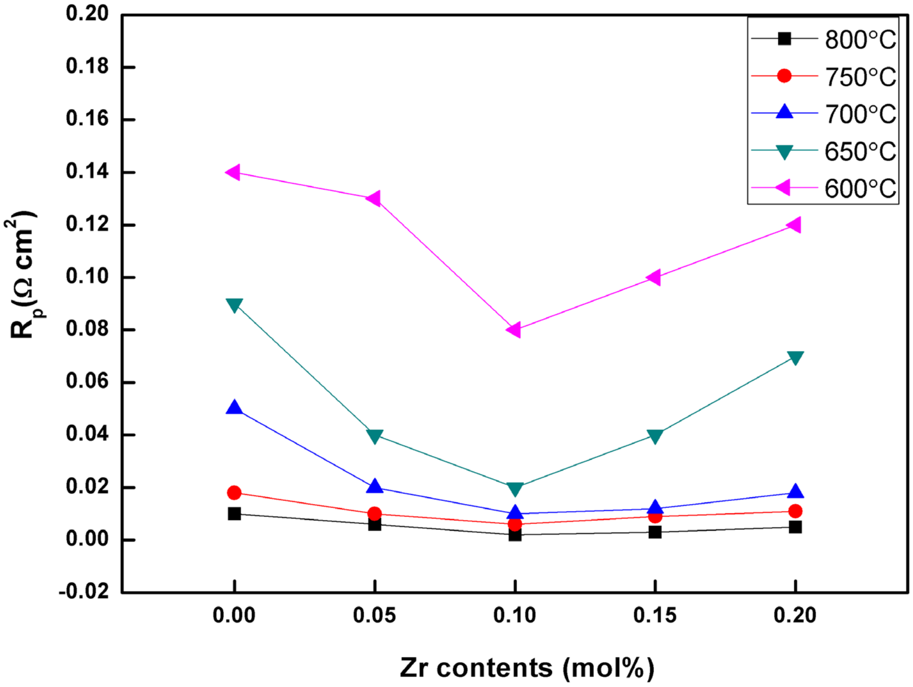

Figure 5.3 Polarization resistance (R_p) of the Ni-ZrxSDC electrode symmetry cell.

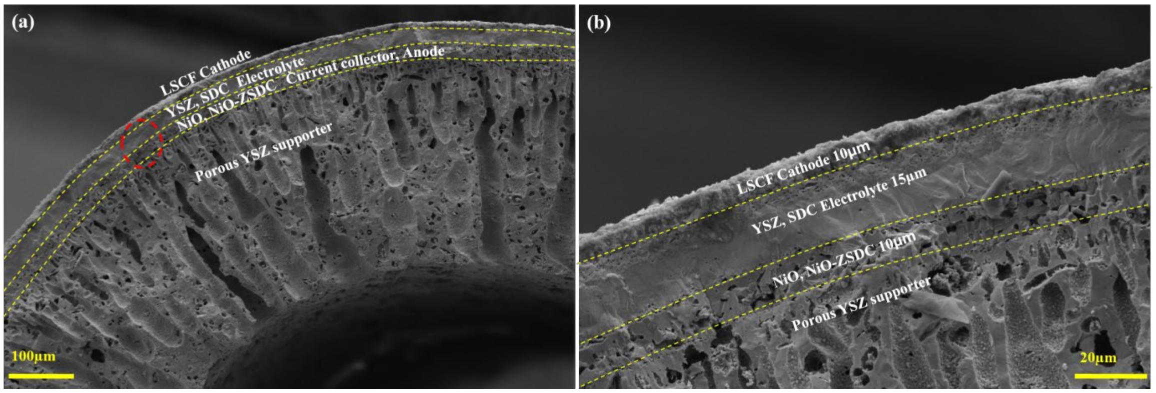

Figure 5.4 (a) SEM cross-sectional image of as-prepared porous YSZ supported single cell. (b) Enlarged SEM image of local area marked with the red circle in (a).

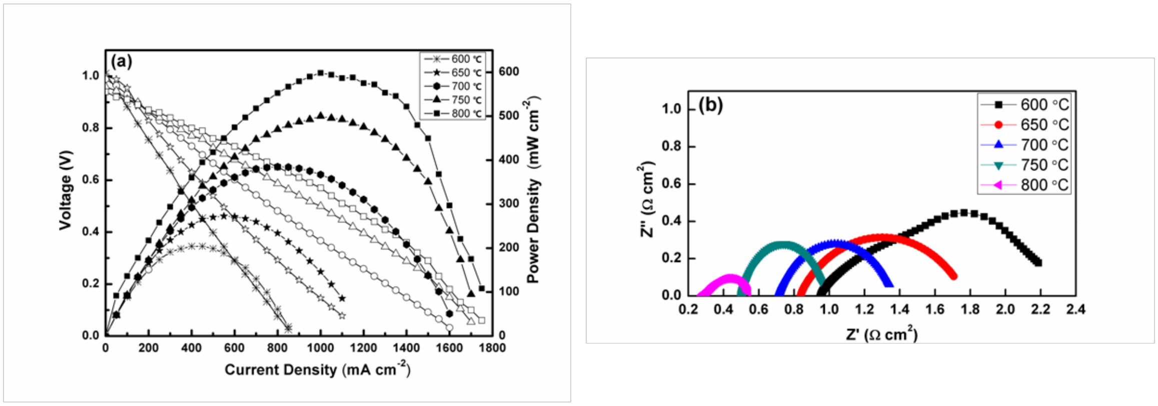

Figure 5.5(a) V-I curves and power density curves of the single cell in hydrogen. (b) EIS curves of the single cell in hydrogen under open circuit voltage conditions.

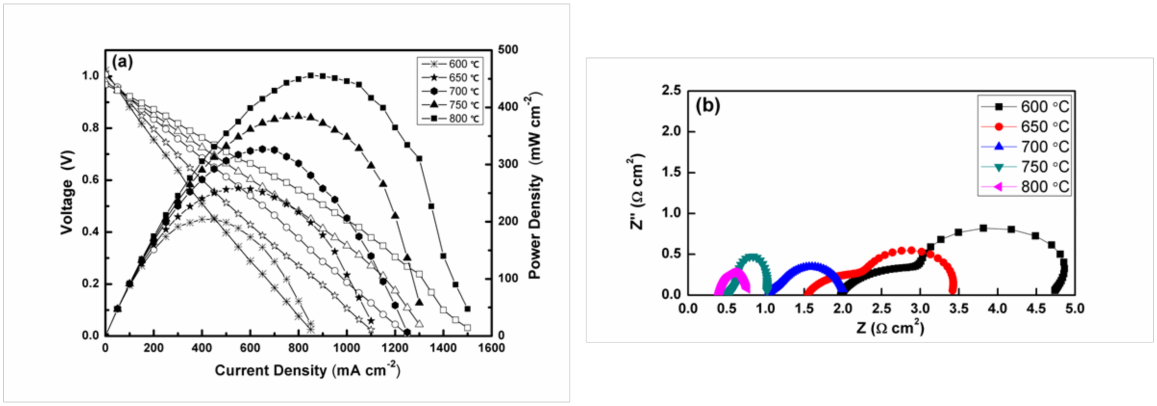

Figure 5.6 (a) V-I curves and power density curves of the single cell in methane. (b) EIS curves of the single cell in methane under open circuit voltage conditions.

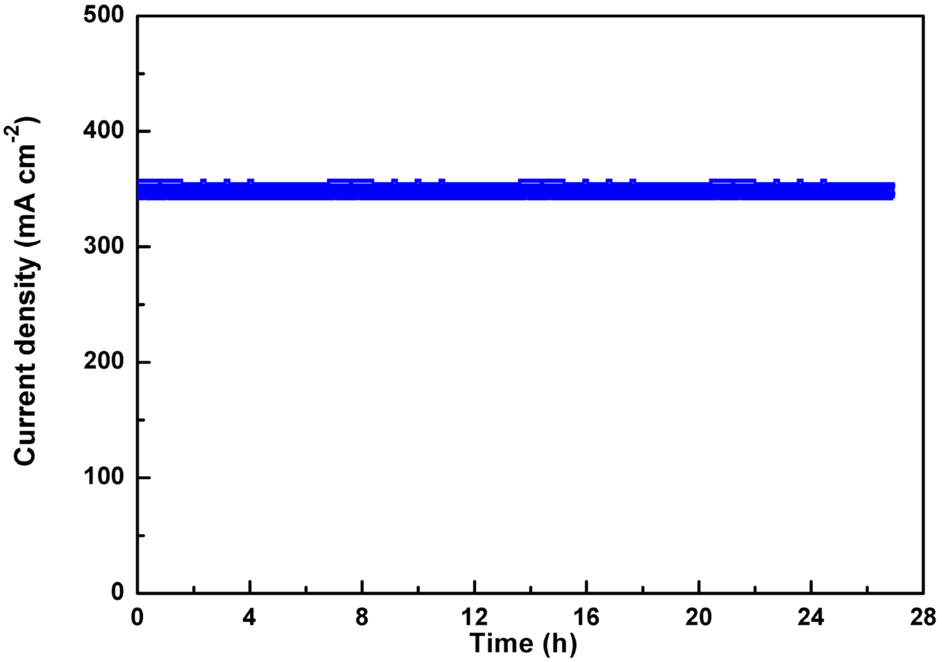

Figure 5.7 Short-term performance stability of the single cell in methane fuel at 0.7 V and 700ºC.

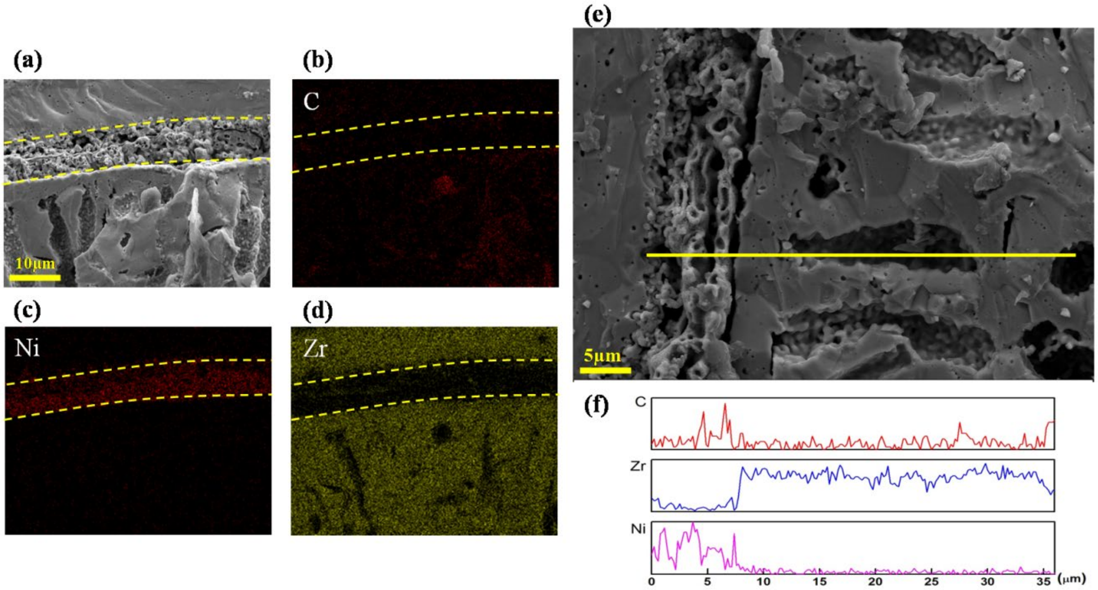

Figure 5.8 SEM and EDS images of the single cell after stability measurement. (a) Cross sectional SEM image of the single cell. (b) EDS mapping ofNi. (c) EDS mapping of C. (d) EDS mapping of Zr. (e)Location for line EDS characterization and C, Zr, Ni line EDS spectrum.

CHAPTER 6

SUMMARY

Oxygen is very important in modern industries because it makes carbon dioxide which is an emission gas generated from the combustion process to be collected for the usage of other industries or further sequestration. As a result, it can prevent the direct release of emission gas as a greenhouse gas.

Using mixed ionic and electronic conducting (MIEC) dense ceramic membrane to separate oxygen from the air has received widely great attention due to its simple, cost-effective operation. It has become one of the important technologies in energy generation based on clean combustion when combined with gasification combined cycle, oxygen enrichment, oxyfuel, decarbonized fuel, gas to a liquid, etc.

Planar and tubular types are widely used as configurations in oxygen permeation membranes. The planar design is easy to manufacture but requires a long sealing length bringing up sealing problems. The tubular design exhibits great advantages of short sealing length and good thermal shock resistance. Especially, micro-tubular type demonstrates a high surface to volume ratio that may effectively increase the volumetric density of oxygen permeation flux. However, challenges in fabricating process of tubular design, particularly for miniaturization designs where the diameters of a millimeter or sub-millimeter scale. In the past few years, the slurry spinneret technology in combination with phase inversion method has been developed to fabricate hollow fiber membranes successfully.

Despite all these great advantages, the current membrane developments either show high permeability but poor stabilities or great robustness and durability but low oxygen permeation performance. The intrinsic material brittleness limits the mechanistic strength of the membranes, therefore their robustness and stability. This limits the upscaling ability of hollow fiber membranes for compact stack/module development. It is necessary to improve the mechanical strength of individual hollow fiber membranes. One potential method is to use composite materials for hollow fibers for instance simple metal oxides. However, the addition of simple metal oxides may decrease the effective conductivity of the membrane for charge transport. In this dissertation, a composite hollow fiber-supported thin film membrane with a configuration of LSCF-ZnO7525/LSCF dense functional layer/PBCFZY porous catalytic layer was fabricated. Composite hollow fiber support improves the mechanical strength of the membrane, and the thin film membrane overcomes the issue possibly induce by a composite hollow fiber substrate. The performance and long-term stability of the membrane are systematically measured and characterized. Results indicate that ZnO addition to the hollow fiber substrate can not only decrease the sintering temperature for thin film densification but also enhance the mechanical strength, and robustness leading to great stability.

For practical applications, the assembly of the membrane stack was also studied. Current assembly techniques are cantilever-like assembly strategy and bundle strategy. The cantilever-like can prevent mechanical loads from applying on hollow fiber membranes but one side port of membranes needs to be closed end for operation, confining the stack operating vacuum mode only. The bundle strategy is to bundle individual membranes together with porous ceramic material, significantly enhancing the mechanical strength. However, the porous material used to bundle membranes will increase the resistance for gas diffusion between bundle circumference and individual membranes in the bundle leading to deteriorating oxygen permeation performance. Furthermore, the sealing issue becomes more prominent at the stack level due to the increased sealing length. For easy gas-tight sealing, the low-temperature sealants of epoxy resin or silicon were typically used for stack. These materials must be located out of hot zone to avoid high-temperature conditions. Consequently, only a small portion of the membranes play a role of oxygen permeation. Given high capital cost of membrane materials, ideally, the full length of hollow fibers in the stack should be able to participate in efficient oxygen permeation. This requires that the full length of hollow fibers and therefore the sealing portion be confined in hot zone. This further implies that hollow fibers in the stack should be strong enough to support various loads and sealing portions should be reliable in harsh temperature conditions.

The membrane stack was developed using hollow fiber substrate-supported thin film membranes. Three membranes were used for the stack assembly. The improved mechanical strength with composite substrate allows assembling hollow fiber membranes individually in parallel to form a membrane stack. The reliable sealing strategy by combining ceramic paste with adhesive ink enables direct operations of the stack including the sealing portions in a hot zone. Results indicate excellent chemical compatibility among involved materials and microstructural stability of individual hollow fibers in the stack as well as reliable sealing portions. Also, the membrane used in this study is applicable for stack development with the bundle and cantilever-like strategies.

Solid oxide fuel cell (SOFC) has attracted considerable attention due to their high efficiency, low pollutant emission, and fuel flexibility. Due to the use of all solid oxide materials, the operating temperature of SOFCs is high (>800°C), and hydrocarbon fuel can be directly utilized without reforming. However, the high catalytic activity of Ni in anode can lead to carbon deposition when running in hydrocarbon fuel. This will deactivate active reaction sites, restrict gas flow, and damage microstructures, overall leading to severe degradations in anode performance and long-term stability. To improve the performance stability of the single cell in methane fuel, a synergic strategy is employed to design anode electrodes. Zr is incorporated into $Ce_{0.8}Sm_{0.2}O_{2-\delta}$ lattice to tailor oxygen storage and catalytic properties of Ni-$Ce_{0.8-x}Sm_{0.2}Zr_xO_{2-\delta}$ anode for improving electrochemical oxidation of various fuel species. And an inert thick YSZ microtubular substrate with radially well-aligned microchannels open at the inner surface supports multi-thin functional layers of the cell. The thick YSZ substrate inhibits the ratio of fuel to product gases in the thin anode functional layer, which favors the prevention of carbon buildup in the thin anode layer when synergistically combined with Ni-$Ce_{0.8-x}Sm_{0.2}Zr_xO_{2-\delta}$ anode material. Results exhibited very good performance stability for 26hrs short-term durability test at 700°C near the condition of peak power density output when directly fueled with methane. The capability of carbon deposition prevention was achieved through a synergistic combination of oxygen storage and catalytic properties of the ZrSDC phase in the anode functional layer and novel architecture design of the cell.

This dissertation has successfully fabricated and characterized asymmetric hollow fiber-supported thin film membranes for oxygen separation from air and solid oxide fuel cell in methane fuel. The membrane performance is greatly enhanced and showed excellent long-term stability even under harsh thermal cycling stability. Furthermore, a stack was successfully developed using the fabricated membranes. The improved mechanical strength with composite substrate allows the assembling of hollow fiber membranes individually in parallel to form a membrane stack. The membrane stack showed great oxygen permeation flux, as well as excellent long-term stability, showing the applicable stack development of this study.

Also, the single cell for solid oxide fuel cell (SOFC) was successfully fabricated to improve the performance stability in methane fuel. The thick YSZ substrate with radially well-aligned microchannels open at the inner substrates and the Ni-ZSDC anode synergistically combined which favors the prevention of carbon buildup in the thin anode functional layer. The cell exhibited very good performance stability and showed the capability of carbon deposition prevention was achieved.

REFERENCES

[1] Pachauri R. K., Allen M. R., Barros V. R., Broome J., Cramer W., Christ R., Church J. A., Clarke L., Dahe Q. and Dasgupta P., Climate change 2014: synthesis report. Contribution of Working Groups I, II and III to the fifth assessment report of the Intergovernmental Panel on Climate Change, *Ipcc* (2014).

[2] Baker R.W., Future direction of membrane gas separation technology, *Industrial & Engineering Chemistry Research,* 41(6), 1393-1411, (2002).

[3] MacDowell N., Florin N., Buchard A., Hallett J., Galindo A., Jackson G., Claire S. A., Williams C.K., Shah N. and Fennell P., An overview of CO_2 capture technologies, *Energy & Environmental Science,* 3, 1645-1669, (2010).

[4] Smart S., Lin C.X.C., Ding L., Thambimuthu K., and Diniz da Coasta J.C., Ceramic membranes for gas processing in coal gasification, *Energy & Environmental Science,* 3, 268-278, (2010).

[5] Matson S.L., Ward W.J., Kimura S.G., and Browall W.R., Membrane oxygen enrichment: II. Economic assessment, *Journal of Membrane Science,* 29(1), 79-96, (1986).

[6] Surya Murali R., Sankarashana T., and Sridhar S., Air separation by polymer-based membrane technology, *Separation & Purification Reviews,* 42(2), 130-186, (2013).

[7] Geffroy P.M., Blond E., Richet N., and Chartier T., Understanding and identifying the oxygen transport mechanisms through a mixed-conductor membrane, *Chemical Engineering Science,* 162(27), 245-261, (2017).

[8] Sunarso J., Liu S., Lin Y.S., and Diniz da Costa J.C., High performance BaBiScCo hollow fibre membranes for oxygen transport, *Energy & Environmental Science,* 4, 2516-2519, (2011).

[9] Yadav M., Gong W., and Jacobson A.J., Electrically driven oxygen separation through gadolinia-doped ceria using $PrBaCo_2O_{5+x}$ and $NdBaCo_2O_{5+x}$ electrodes, *Journal of Solid State Electrochemistry,* 15, 293-301, (2011).

[10] Wang L., Imashuku S., Grimaud A., Lee D., Mezghani K., Habib M.A., and Yang S.H., Enhancing oxygen permeation of electronically short-circuited oxygen-ion conductors by decorating with mixed ionic-electronic conducting oxides, *ECS Electrochemistry Letters,* 2(11), F77-F81, (2013).

[11] Zeng P., Ran R., Chen Z., Gu H., Shao Z., and Liu S., Novel mixed conducting $SrSc_{0.05}Co_{0.95}O_{3-\delta}$ ceramic membrane for oxygen separation, *AIChE Journal,* 53(12), 3116-3124, (2007).

[12] Puig-Arnavat M., Søgaard M., Hjuler K., Ahrenfeldt J., Henriksen U. and Hendriksen P.V., Integration of oxygen membranes for oxygen production in cement plants, *Energy,* 91, 852-865, (2015).

[13] Wagner C., Equations for transport in solid oxides and sulfides of transition metals, *Progress in Solid State Chemistry*, 10(3), 3-16, (1975).

[14] Minh N.Q., and Takahashi T., Science and technology of ceramic fuel cells, *Elsevier,* (1995).

[15] Singhal S., High-temperature solid oxide fuel cells: fundamentals, design and application, *Elsevier,* (2003).

[16] Sharaf O. Z. and Orhan M. F., An overview of fuel cell technology: Fundamentals and applications, *Renewable and Sustainable Energy Reviews,* 32, 810-853, (2014).

[17] O'hayre R., Cha S.W., Colella W., and Prinz F. B., Fuel cell fundamentals, *John Wiley & Sons,* (2016).

[18] Goodenough J.B., Oxide-ion electrolytes, *Annual review of materials research*, 33, 91-128, (2003).

[19] Steele B.C.H. and Heinzel A., Materials for fuel-cell technologies, *Nature,* 414, 345-354, (2001).

[20] Kharton V.V., Marques F.M.B, and Atkinson A., Transport properties of solid oxide electrolyte ceramics: a brief review, *Solid State Ionics,* 174(1-4), 135-149, (2004).

[21] Omar S., Belda A., Escardino A., and Bonanos N., Ionic conductivity ageing investigation of 1Ce10ScSZ in different partial pressures of oxygen, *Solid State Ionics,* 184(1), 2-5, (2011).

[22] Tsipis E., and Kharton V., Electrode materials and reaction mechanisms in solid oxide fuel cells: a brief review, *Journal of a Solid State Electrochemistry,* 12, 1367-1391, (2008).

[23] Tsipis E., and Kharton V., Electrode materials and reaction mechanisms in solid oxide fuel cells: a brief review, III. Recent trends and selected methodological aspects, *Journal of Solid State Electrochemistry,* 15, 1007-1040, (2011).

[24] Wang W., Su C., Wu Y., Ran R., and Shao Z., Progress in solid oxide fuel cells with nickel-based anodes operating on methane and related fuels, *Chemical Reviews,* 113(10), 8104-8151, (2013).

[25] Sarkar P., Yamarte L., Rho H., and Johanson L., Anode-supported tubular micro-solid oxide fuel cell, *International Journal of Applied Ceramic Technology,* 4(2), 103-108, (2007).

[26] Takeguchi T., Kani Y., Yano T., Kikuchi R., Eguchi K., Tsujimoto K., Uchida Y., Ueno A., Omoshiki K. and Aizawa M., Study on steam reforming of CH_4 and C_2 hydrocarbons and carbon deposition on Ni-YSZ cerments, *Journal of Power Sources,* 112(2), 588-595, (2002).

[27] Ke K., Gunji A., Mori H., Tsuchida T., Takahashi H., Ukai K., Mizutani Y., Sumi H., Yokoyama M. and Waki K., Effect of oxide on carbon deposition behavior of CH_4 fuel on Ni/ScSZ cermet anode in high temperature SOFCs, *Solid State Ionics,* 177(5-6), 541-547, (2006).

[28] Kim H., Lu C., Worrell W.L., Vohs J.M., and Gorte R.J., Cu-Ni cermet anodes for direct oxidation of methane in solid-oxide fuel cells, *Journal of Electrochemical Society,* 149(3), A247-A250, (2002).

[29] Myung J.H., Kim S.D., Shin T.H., Lee D.H., Irvine J.T.S., Moon J. and Hyun S.H., Nano-composite structural Ni-Sn alloy anodes for high performance and durability of direct methane-fueled SOFCs, *Journal of Materials Chemistry A*, 3, 13801-13806, (2015).

[30] Wu X., Zhou X., Tian Y., Kong X., Zhang J., Zuo W., Ye X. and Sun K., Preparation and electrochemical performance of silver impregnated Ni-YSZ anode for solid oxide fuel cell in dry methane, *International Jouranl of Hydrogen Energy,* 40(46), 16484-16493, (2015).

[31] Tao S., and Irvine J.T.S., A redox-stable efficient anode for solid-oxide fuel cells, *Nature Materials*, 2, 320-323, (2003).

[32] Huang Y.H., Dass R.I., Xing Z.L. and Goodenough J.B., Double perovskites as anode materials for solid oxide fuel cells, *Science,* 312(5771), 254-257, (2006).

[33] Ozawa M., Kimura M. and Isogai A., The application of Ce-Zr oxide solid solution to oxygen storage promoters in automotive catalysts, *Journal of Alloys and Compounds,* 193(1-2), 73-75, (1993).

[34] Zhu W.Z. and Deevi S.C., A review on the status of anode materials for solid oxide fuel cells, *Materials Science and Engineering: A,* 365(1-2), 228-239, (2003).

[35] Ormerod R.M., Solid oxide fuel cells, *The Royal Society of Chemistry,* 32, 17-28, (2003).

[36] Murray E.P., Tsai T. and Barnett S.A., A direct-methane fuel cell with a ceria-based anode, *Nature,* 400, 649-651, (1999).

[37] Liu S., Li K. and Hughes R., Preparation of porous aluminum oxide hollow fibre membranes by a combined phase inversion and sintering method, *Ceramics International*, 29 (875), 875-881, (2003).

[38] Hsieh H. P., Inorganic membrane reactor, *Catalysis Reviews*, 33(1), 1-70, (1991).

[39] McKeen L.W., Permeability properties of plastics and elastomers, *William Andrew Publishing,* 61-81, (2016).

[40] Lonsdale H.K., The growth of membrane technology, *Journal of membrane science,* 10(2-3), 81-181, (1982).

[41] Benfer S., Popp U., Richter H., Siewert C. and Tomandl G., Development and characterization of ceramic nanofiltration membranes, *Separation and Purification Technology*, 22-23(231), 231-237, (2001).

[42] Wang Q., Wang Z. and Wu Z., Effects of solvent compositions on physicochemical properties and anti-fouling ability of PVDF microfiltration membranes for wastewater treatment, *Desalination*, 297(79), 79-86, (2012).

[43] Li L., Chen M., Dong Y., Dong X., Cerneaux S., Hampshire S., Cao J., Zhu L., Zhu Z. and Liu J., A low-cost alumina-mullite composite hollow fiber ceramic membrane fabricated via phase-inversion and sintering method, *Journal of the European Ceramic Society,* 36 (8), 2057-2066, (2016).

[44] Drioli E. and Giorno L., Membrane operations: innovative separations and transformantions, *John Wiley&Sons,* (2009).

[45] Zare S. and Kargari A., Emerging technologies for sustainable desalination handbook, V.G. GUde Editor, *Butterworth-Heinemann,* 107, (2018).

[46] Purkait M.K., Sinha M.K., Mondal P. and Singh R., Interface Science and Technology, *Elsevier,* 1, (2018).

[47] Strathmann H., Scheible P. and Baker R.W., A rationale for the preparation of Loeb-Sourirajan-type cellulose acetate membranes, *Journal of Applied Polymer Science,* 15, 811-828, (1971).

[48] Wu Z.T., Othman M.H.D., Kingsbury B.F.K. and Li K., Advanced membrane science and technology for sustainable energy and environmental applications, Basile A. and Nunes S.P. Editors, *Woodhead Publishing,* 496, (2011).

[49] Tan X., Li K., Handbook of Membrane Reactors, A. Basile Editor, *Woodhead Publishing,* 271 (2013).

[50] Wang D., Li K. and Teo W., Preparation of annular hollow fibre membranes, *Journal of Membrane Science,* 166, 31-39, (2000).

[51] He T., Mulder M., Strathmann H. and Wessling M., Preparation of composite hollow fiber membranes: co-extrusion of hydrophilic coatings onto porous hydrophobic support structrues, *Journal of Membrane Science,* 207, 143-156, (2002).

[52] Li D.F., Chung T.S., Wang R. and Liu Y., Fabrication of fluoropolyimide/polyethersulfone (PES) dual-layer asymmetric hollow fiber membranes for gas separation, *Journal of Membrane Science,* 198, 211-223, (2002).

[53] Cao C., Chung T.S., Chen S.B. and Dong Z., The study of elongation and shear rates in spinning process and its effect on gas separation performance of poly (ether sulfone)(PES) hollow fiber membrnaes, *Chemical Engineering Science,* 59, 1053-1062, (2004).

[54] Li K., Tan X. and Liu Y., Single-step fabrication of ceramic hollow fibers for oxygen permeation, *Journal of Membrane Science,* 272, 1-5, (2006).

[55] Widjojo N., S Zhang.D., ChungT.S. and Liu Y., Enhanced gas separation performance of dual-layer hollow fiber membranes via substructure resistance reduction using mixed matrix materials, *Journal of Membrane Science,* 306, 147-158, (2007)..

[56] Yin W., Meng B., Meng X., and Tan X., Highly asymmetric yttria stabilized zirconia hollow fibre membranes, *Journal of Alloys and Compounds,* 476 (1-2), 566-570, (2009).

[57] Bhide B. D. and Stern S. A., A new evaluation of membrane processes for the oxygen enrichment air. II. effects of economic-parameters and membrane-properties, *Journal of Membrane Science,* 62 (1), 37-58, (1991).

[58] Wu F. Argyle M. D. Dellenback P. A. and Fan M., Progress in O_2 separation for oxy-fuel combustion–A promising way for cost-effective CO_2 capture: A review, *Progress in Energy and Combustion Science,* 67, 188-205, (2018).

[59] Wang Z., Yang N., Meng B., Tan X., and Li K., Preparation and Oxygen Permeation Properties of Highly Asymmetric $La_{0.6}Sr_{0.4}Co_{0.2}Fe_{0.8}O_{3-\alpha}$ Perovskite Hollow-Fiber Membranes, *Industrial and Engineering Chemistry Research,* 48(1), 510-516, (2009).

[60] Liu S., and Gavalas G. R., Oxygen selective ceramic hollow fiber membranes, *Journal of Membrane Science,* 246(1), 103-108, (2005).

[61] Ren C., Gan Y., Lee M., Yang C., He F., Jiang Y., Dong G., Green R. D. and Xue X., Fabrication and Characterization of High Performance Intermediate

Temperature Micro-Tubular Solid Oxide Fuel Cells. *Journal of Electrochemical Society,* 163(9), F1115-F1123, (2016).

[62] Zydorczak B., Wu Z., and Li K., Fabrication of ultrathin $La_{0.6}Sr_{0.4}Co_{0.2}Fe_{0.8}O_{3-\delta}$ hollow fibre membranes for oxygen permeation, *Chemical Engineering Science,* 64, 4383-4388, (2009).

[63] Liu N., Tan X., Meng B. and Liu S., Honeycomb-structured perovskite hollow fiber membranes with ultra-thin densified layer for oxygen separation, *Separation and Purification Technology,* 80, 396-401, (2011).

[64] Han N., Zhang S., Meng X., Yang N., Meng B., Tan X. and Liu S., Effect of enhanced oxygen reduction activity on oxygen permeation of $La_{0.6}Sr_{0.4}Co_{0.2}Fe_{0.8}O_{3-\delta}$ membrane decorated by K_2NiF_4-type oxide, *Journal of Alloys and Compounds,* 654, 280-2898, (2016).

[65] Zhang S., Li C., Meng X., Tan X., Zhu Z., Sunarso J. and Liu S., CO_2-resistant SDC-SSAF oxygen selective dual-phase hollow fiber membranes, *Asia-Pacific Journal of Chemical Engineering,* 15, e2528, (2020).

[66] Meng X., Sunarso J., Jin Y., Bi X., Yang N., Tan X., Wang S. and Liu S., Robust CO_2 and H_2 resistant triple-layered (Ag-YSZ)/YSZ/($La_{0.8}Sr_{0.2}$MnO3- δ-YSZ) hollow fiber membranes with short-circuit for oxygen permeation. *Journal of Membrane Science,* 524, 596-603, (2017).

[67] Li D., Wang R. and Chung T.S., Fabrication of lab-scale hollow fiber membrane modules with high packing density, Separation and Purification Technology, 40, 15-30, (2004).

[68] Tan X., Liu Y. and Li K., Mixed conducting ceramic hollow-fiber membranes for air separation, *AIChE Journal,* 51(7), 1991-2000, (2005).

[69] Tan X., Wang Z., Meng B., Meng X. and Li K., Pilot-scale production of oxygen from air using perovskite hollow fibre membranes, *Journal of Membrane Science,* 352(1-2), 189-196, (2010).

[70] Schulz M., Pippardt U., Kiesel L., Ritter K. and Kriegel R., Oxygen permeation of various archetypes of oxygen membranes based on BSCF, *AIChE Journal,* 58(10), 3195, (2012).

[71] Baumann S., Meulenberg W.A. and Buchkremer H.P., Manufacturing strategies for asymmetric ceramic membranes for efficient separation of oxygen from air, *Journal of European Ceramic Society,* 33, 1251-1261, (2013).

[72] An R., Song J., Li Y., Tan X., Sunarso J., Zhang C., Wang S. and Liu S., Bundling strategy to simultaneously improve the mechanical strength and oxygen permeation flux of the individual perovskite hollow fiber membranes, *Journal of Membrane Science,* 527, 137-142, (2017).

[73] Hu Y., An R., Chu Y., Tan X., Sunarso J., Wang S. and Liu S., Perovskite hollow fiber membranes supported in a porous and catalytically active perovskite matrix for air separation, *Separation and Purification Technology,* 192, 435-440, (2018).

[74] Song J., Feng B., Tan X., Han N., Sunarso J. and Liu S., Oxygen selective perovskite hollow fiber membrane bundles, *Journal of Membrane Science,* 581, 393-400, (2019).

[75] Tan X. and Li K., Oxygen production using dense ceramic hollow fiber membrane modules with different operating modes, *AIChE Journal,* 53 (4), 838-845, (2007).

[76] Tan X., Pang Z. and Li K., Oxygen production using $La_{0.6}Sr_{0.4}Co_{0.2}Fe_{0.8}O_{3-\alpha}$ (LSCF) perovskite hollow fibre membrane modules. *Journal of Membrane Science,* 310(1-2), 550-556, (2008).

[77] Ren C., Gan Y., Yang C., Lee M. and Xue X., A rational asymmetric hollow fiber membrane for oxygen permeation, *International Journal of Applied Ceramic Technology,* 16 (2), 791-801, (2019).

[78] Gan Y., Ren C., Lee M., Yang C. and Xue X., Fabrication and characterization of microtubular solid oxide cell supported with nanostructured mixed conducting perovskite fuel electrode, *Journal of Solid State Electrochemistry,* 22 (9), 2929-2943, (2018).

[79] Tikkanen H., Suciu C., Wærnhus I., and Hoffmann A. C., Examination of the co-sintering process of thin 8YSZ films obtained by dip-coating on in-house produced NiO–YSZ, *Journal of the European Ceramic Society,* 31 (9), 1733-1739, (2011).

[80] Yamaguchi T., Suzuki T., Shimizu S., Fujishiro Y. and Awano M., Examination of wet coating and co-sintering technologies for micro-SOFCs fabrication, *Journal of Membrane Science,* 300 (1), 45-50, (2007).

[81] Morales M., Laguna-Bercero M. A., Navarro M. E., Espiell F. and Segarra M.,' The effect of anode support on the electrochemical performance of microtubular solid oxide fuel cells fabricated by gel-casting, *RSC Advances,* 5 (49), 39350-39357, (2015).

[82] Tai L. W., Nasrallah M. M., Anderson H. U., Sparlin D. M. and Sehlin S. R., Structure and electrical properties of $La_{1-x}Sr_xCo_{1-y}Fe_yO_3$. Part 1. The system $La_{0.8}Sr_{0.2}Co_{1-y}Fe_yO_3$, *Solid State Ionics,* 76 (3), 259-271, (1995).

[83] Wei B., Lü Z., Li S., Liu Y., Liu K. and Su W., Thermal and Electrical Properties of New Cathode Material $Ba_{0.5}Sr_{0.5}Co_{0.8}Fe_{0.2}O_{3-\delta}$ for Solid Oxide Fuel Cells, *Electrochemical and Solid-State Letters,* 8 (8), A428, (2005).

[84] Wang Z., Liu H., Tan X., Jin Y. and Liu S., Improvement of the oxygen permeation through perovskite hollow fibre membranes by surface acid-modification, *Journal of Membrane Science,* 345(1-2), 65-73, (2009).

[85] Meng Y., He W., Li X., Gao J., Zhan Z., Yi J., Chen C. and Bouwmeester H.J.M., Asymmetric $La_{0.6}Sr_{0.4}Co_{0.2}Fe_{0.8}O_{3-\delta}$ membrane with reduced concentration polarization prepared by phase-inversion tape casting and warm pressing, *Journal of Membrane Science,* 533, 11-18, (2017).

[86] Wang Z., Yang N., Meng B., Tan X. and Li K., Preparation and oxygen permeation properties of highly asymmetric $La_{0.6}Sr_{0.4}Co_{0.2}Fe_{0.8}O_{3-\delta}$ perovskite hollow-fiber membranes. *Industrial and Engineering Chemistry Research,* 48, 510-516, (2009).

[87] Shao X., Dong D., Parkinson G. and Li C.Z., Improvement of oxygen permeation through microchanneled ceramic membranes, *Journal of Membrane Science,* 454, 444-450, (2014).

[88] Han D., Sunarso J., Tan Xi., Yan Z., Liu L. and Liu S., Optimizing oxygen transport through $La_{0.6}Sr_{0.4}Co_{0.2}Fe_{0.8}O_{3-\delta}$ hollow fiber by microstructure modification and Ag/Pt catalyst deposition, *Energy and fuels,* 26(8), 4728-4734, (2012).

[89] Han D., Wu J., Yan Z., Zhang K., Liu J. and Liu S., $La_{0.6}Sr_{0.4}Co_{0.2}Fe_{0.8}O_{3-\delta}$ hollow fibre membrane performance improvement by coating of $Ba_{0.5}Sr_{0.5}Co_{0.9}Nb_{0.1}O_{3-\delta}$ porous layer, *RSC Advances.*, 4, 19999-20004, (2014).

[90] Pan H., Li L., Deng X., Meng B., Tan X. and Li K., Improvement of oxygen permeation in perovskite hollow fibre membranes by the enhanced surface exchange kinetics, *Journal of Membrane Science,* 428, 198-204, (2013).

[91] Gopan A., Kumfer B.M., Phillips J., Thimsen D., Smith R., Axelbaum R.L., Process design and performance analysis of a Staged, Pressurized Oxy-combustion (SPOC) power plant for carbon capture, Applied Energy, 125, 179-188, (2014).

[92] Lupiáñez C., Díez L.I., Romeo L.M., Influence of gas-staging on pollutant emissions from fluidized bed oxy-firing, Chemical Engineering Journal, 256, 380-389, (2014).

[93] Burdyny T., Struchtrup H., Hybrid membrane/cryogenic separation of oxygen from air for use in the oxy-fuel process, Energy, 35, 1884-1897, (2010).

[94] Sircar S., Pressure swing adsorption, Industrial & Engineering Chemistry Research, 41, 1389-1392, (2002).

[95] Ismail A.F., Khulbe K.C., Matsuura T., Gas Separation Membranes, Springer, (2015).

[96] Tan X., Liu Y., Li K., Preparation of LSCF ceramic hollow-fiber membranes for oxygen production by a phase-inversion/sintering technique, Industrial & Engineering Chemistry Research, 44, 61-66, (2005).

[97] Caro J., Hierarchy in inorganic membranes, Chemical Society Reviews, 45, 3468-3478, (2016).

[98] Vente J.F., Haije W.G., Ijpelaan R., Rusting F.T., On the full-scale module design of an air separation unit using mixed ionic electronic conducting membranes, Journal of Membrane Science, 278, 66-71, (2006).

[99] Feng B., Song J., Wang Z., Dewangan N., Kawi S., Tan X., CFD modeling of the perovskite hollow fiber membrane modules for oxygen separation, Chemical Engineering Science, 230, 116214, (2021).

[100] Jogdand S.M., Bedadur P.R., Torris A., Agrawal R., Kharul U.K., Devi R.N., Addressing challenges in sealing of scalable multifiber module for O2 enrichment using LSCF membranes, International Journal of Applied Ceramic Technology, 19, 1561-1571, (2022).

[101] Li K., Tan X., Liu Y., Single-step fabrication of ceramic hollow fibers for oxygen permeation, Journal of Membrane Science, 272, 1-5, (2006).

[102] Tan X., Liu N., Meng B., Liu S., Morphology control of the perovskite hollow fibre membranes for oxygen separation using different bore fluids, Journal of Membrane Science, 378, 308-318, (2011).

[103] Tan X., Wang Z., Liu H., Liu S., Enhancement of oxygen permeation through $La_{0.6}Sr_{0.4}Co_{0.2}Fe_{0.8}O_{3-\delta}$ hollow fibre membranes by surface modifications, Journal of Membrane Science, 324, 128-135, (2008).

[104] Gaudillere C., Garcia-Fayos J., Serra J.M., Enhancing oxygen permeation through hierarchically-structured perovskite membranes elaborated by freeze-casting, Journal of Materials Chemistry A, 2, 3828-3833, (2014).

[105] Wang B., Song J., Tan X., Meng B., Liu J. Liu S., Reinforced perovskite hollow fiber membranes with stainless steel as the reactive sintering aid for oxygen separation, Journal of Membrane Science, 502, 151-157, (2016).

[106] Chi Y., Li T., Wang B., Wu Z., Li K., Morphology, performance and stability of multi-bore capillary $La_{0.6}Sr_{0.4}Co_{0.2}Fe_{0.8}O_{3-\delta}$ oxygen transport membranes, Journal of Membrane Science, 529, 224-233, (2017).

[107] Lee M., Gan Y., Yang C., Ren C., Xue X., Fabrication and accelerated long-term stability test of asymmetrical hollow fiber-supported thin film oxygen separation membrane, Journal of Membrane Science, 655, 120600, (2022).

[108] Ren C., Gan Y., Yang C., Lee M., Xue X., Fabrication and characterization of direct methane fueled thin film SOFCs supported by microchannel-structured microtubular substrates, Applied Energy Materials, 3, 1831-1841, (2020).

[109] Ren C., Gan Y., Yang C., Lee M., Green R.D., Xue X., Fabrication and characterization of microtubular solid oxide cells for CO2/CO redox operations, Journal of Applied Electrochemistry, 48, 959-971, (2018).

[110] Ren C., Gan Y., Yang C., Lee M., Dong G., Xue X., Fabrication and characterization of high performance intermediate temperature alumina substrate supported micro-tubular SOFCs, Journal of the Electrochemical Society, 164 (7), F722-F731, (2017).

[111] Xu S.J. and Thomson W.J., Oxygen permeation rates through ion-conducting perovskite membranes, *Chemical Engineering Science,* 54 (17), 3839-3850, (1999).

[112] Fang W., Liang F., Cao Z., Steinbach F. and Feldhoff A., A mixed ionic and electronic conducting Dual-phase membrane with high oxygen permeability, *Angewandte Chemie International Edition,* 54 (16), 4847-4850, (2015).

[113] Wei Y., Yang W., Caro J. and Wang H., Dense ceramic oxygen permeable membranes and catalytic membrane reactors, *Chemical Engineering Journal,* 220, 185-203, (2013).

[114] Rachadel P., Garcia G.S., Machado R.A.F., Hotza D. and Diniz da Costa J.C., Current developments of mixed conducting membranes on porous substrates, *Materials Research,* 17, 242-249, (2014).

[115] Zhang K., Sunarso J., Shao Z., Zhou W., Sun C., Wang S. and Liu S., Research progress and materials selection guidelines on mixed conducting perovskite-type ceramic membranes for oxygen production, *RSC Advances,* 1, 1661-1676, (2011).

[116] Baumann S., Serra J.M., Lobera M.P., Escolastico S., Schulze-Kuppers F. and Meulenberg W.A., Ultrahigh oxygen permeation flux through supported $Ba_{0.5}Sr_{0.5}Co_{0.8}Fe_{0.2}O_{3-\delta}$ membranes, *Journal of Membrane Science,* 377, 198-205, (2011).

[117] Guo S., Zhu J., Liu Z., Jian X., Zhang Z. and Jin W., Enhanced high oxygen permeation of mixed-conducting multichannel hollow fiber membrane via surface modified porous layer, *Industrial & Engineering Chemistry Research,* 54, 6985-6992, (2015).

[118] Zhang Y., Yuan R.H., Gao J.F. and Chen C.S., Oxygen permeation properties of supported planar $Zr_{0.84}Y_{0.16}O_{1.92}$-$La_{0.8}Sr_{0.2}Cr_{0.5}Fe_{0.5}O_{3-\delta}$ composite membranes, *Separation and Purification Technology,* 166, 142-147, (2016).

[119] He W., Huang H., Gao J.F., Winnubst L. and Chen C.S., Phase-inversion tape casting and oxygen permeation properties of supported ceramic membranes, *Journal of Membrane Science,* 452, 294-299, (2014).

[120] Wang H., Schiestel T., Tablet C., Schroeder M. and Caro J., Mixed oxygen ion and electron conducting hollow fiber membranes for oxygen separation, *Solid State Ionics,* 177, 2255-2259, (2006).

[121] Dashti A. and Asghari M., Recent progresses in ceramic hollow-fiber membranes, *Chemical Bio Engineering Reviews,* 2(1), 54-70, (2015).

[122] Gromada M., Trawczynski J., Wierzbicki M. and Zawadzki M., Effect of forming techniques on efficiency of tubular oxygen separating membranes, *Ceramics International,* 43, 256-261, (2017).

[123] Jamil S.M., Othman M., Rahman M.A., Jaafar J., Ismail A.F. and K. Li., Recent fabrication techniques for micro-tubular solid oxide fuel cell support: A review, *Journal of the European Ceramic Society,* 35, 1-22, (2015).

[124] Lawlor V., Review of the micro-tubular solid oxide fuel cell (Part II: Cell design issues and research activities), *Journal of Power Sources,* 240, 421-441, (2013).

[125]

[126] Serra J.M., Garcia-Fayos J., Baumann S., Schulze-Kuppers F. and Meulenberg W.A., Oxygen permeation through tape-cast asymmetric all-$La_{0.6}Sr_{0.4}Co_{0.2}Fe_{0.8}O_{3-\delta}$ membranes, *Journal of Membrane Science,* 447, 297-305, (2013).

[127] Wang H. and Barnett S.A., Degradation mechanisms of porous $La_{0.6}Sr_{0.4}Co_{0.2}Fe_{0.8}O_{3-\delta}$ solid oxide fuel cell cathodes, *Journal of the Electrochemical Society,* 165, F564-F570, (2018).

[128] Minh N., Solid oxide fuel cell technology-features and applications, *Solid State Ionics*, 174(1-4), 271-277, (2004).

[129] Zhan Z. and Barnett S. A., An octane-fueled solid oxide fuel cell, *Science*, 308(5723), 844-847, (2005).

[130] Nakagawa N. and Ishida M., Performance of an internal direct-oxidation carbon fuel cell and its evaluation by graphic exergy analysis, *Industrial & Engineering Chemistry Research,* 27, 1181-1185, (1988).

[131] Yang L., Wang S., Blinn K., Liu M., Liu Z., Cheng Z. and Liu M., Enhanced sulfur and coking tolerance of a mixed ion conductor for SOFCs: $BaZr_{0.1}Ce_{0.7}Y_{0.2-x}Yb_xO_{3-\delta}$, *Science,* 326, 126-129, (2009).

[132] Takeguchi T., Kikuchi R., Yano T., Eguchi K. and Murata K., Effect of precious metal addition to Ni-YSZ cermet on reforming of CH_4 and electrochemical activity as SOFC anode, *Catalysis Today,* 84, 217-222, (2003).

[133] Sumi H., Yamaguchi T., Hamamoto K., Suzuki T. and Fujishiro Y., Impact of direct butane microtubular solid oxide fuel cells, *J. Power Sources*, 220, 74-78, (2012).

[134] Kim Y., Kim J.H., Bae J., Yoon C.W. and Nam S.W., In situ analyses of carbon dissolution into Ni-YSZ anode materials, *Journal of Physical Chemistry C,* 116, 13281-13288, (2012).

[135] Miao H., Liu G., Chen T., He C., Peng J., Ye S. and Wang W.G., Behavior of anode-supported SOFCs under simulated syngases, *Journal of Solid State Electrochemistry,* 19, 639-646, (2014).

[136] Zhu H., Wang W., Ran R. and Shao Z., A new nickel-ceria composite for direct-methane solid oxide fuel cells, *International Journal of Hydrogen Energy,* 38, 3741-3749, (2013).

[137] Suzuki T., Yamaguchi T., Hamamoto K., Fujishiro Y., Awano M. and Sammes N., A functional layer for direct use of hydrocarbonfuel in low temperature solid-oxide fuel cells, *Energy & Environmental Science,* 4, 940-943, (2011).

[138] Wang K., Ran R. and Shao Z., Methane-fueled IT-SOFCs with facile in situ inorganic templating synthesized mesoporous $Sm_{0.2}Ce_{0.8}O_{1.9}$ as catalytic layer, *Journal of Power Sources,* 170(2), 251-258, (2007).

[139] Yoon D. and Manthiram A., Hydrogen tungsten bronze as a decoking agent for long-term natural gas-fueled solid oxide fuel cells, *Energy & Environmental Science,* 7(9), 3069-3076, (2014).

[140] Ma J., Jiang C., Connor P. A., Cassidy M. and Irvine J. T. S., Highly efficient, coking-resistant SOFCs for energy conversion using biogas fuels, *Journal of Material Chemistry A,* 3, 19068-19076, (2015).

[141] Wu X., Zhou X., Tian Y., Kong X., Zhang J., Zuo W., Ye X. and K. Sun, Preparation and electrochemical performance of silver impregnated Ni-YSZ anode for solid oxide fuel cell in dry methane, *International Journal of Hydrogen Energy,* 40(46), 16484-16493, (2015).

[142] Qiao J., Zhang N., Wang Z., Mao Y., Sun K. and Yuan Y., Performance of mix-impregnated CeO2-Ni/YSZ anodes for direct oxidation of methane in solid oxide fuel cells, *Fuel Cells*, 9, 729-739, (2009).

[143] Atkinson A., Barnett S., Gorte R. J., Irvine J. T. S., McEvoy A. J., Mogensen M., Singhal S. C. and Vohs J., Review of anode materials development in solid oxide fuel cells, *Nature Materials,* 3, 17, (2004).

[144] Sengodan S., Choi S., Jun A., Shin T. H., Ju Y. W., Jeong H. Y., Shin J., Irvine J. T. S. and Kim G., Layered oxygen-deficient double perovskite as an efficient and stable anode for direct hydrocarbon solid oxide fuel cells, *Nature Materials,* 14, 205-209, (2015).

[145] Dong G., Yang C., He F., Jiang Y., Ren C., Gan Y., Lee M., and Xue X., Tin doped $PrBaFe_2O_{5+\delta}$ anode material for solid oxide fuel cells, *RSC Advances*., 7, 22649-22661, (2017).

[146] McIntosh S., Gorte R. J., *Chemical Review,* 104, 4845-4866, (2004).

[147] Lin Y., Zhan Z. and Barnett S.A., Improving the stability of direct-methane solid oxide fuel cells using anode barrier layer, *Journal of Power Sources,* 158, 1313-1316, (2006).

[148] Zhu H., Colclasure A.M., Kee R.J., Lin Y. and Barnett S.A., Anode barrier layers for tubular solid-oxide fuel cells with methane fuel streams, *Journal of Power Sources,* 161, 413-419, (2006).

[149] Bierschenk D.M., Pillai M.R., Lin Y. and Barnett S.A., Effect of ethane and propane in simulated natural gas on the operation of Ni-YSZ anode supported solid oxide fuel cells, *Fuel Cells*, 10, 1129-1134, (2010).

[150] Novik N.N., Konakov V.G. andArchakov I. Y., Zirconia and ceria based ceramics and nanoceramics-A review on electrochemical and mechanical properties, *Reviews on Advanced Materials Science,* 40, 188, (2015).

[151] Zhao K. and Du Y., Calcium-doped ceria materials for anode of solid oxide fuel cells running on methane fuel, *Journal of Power Sources,* 347, 79-85, (2017).

[152] Larrondo S., Vidal M., Irigoyen B., Craievich A.F., Lamas D.G., Fabregas I.O., Lascalea G.E., Walsoe de Reca N. and Amadeo N., Preparation and characterization of Ce/Zr mixed oxides and their use as catalysts for the direct oxidation of dry CH_4, *Catalysis Today,* 107, 53, (2005).

[153] Laguna O.H., Sarria F.R., Centeno M.A. and Odriozola J.A., Gold supported on meetal-doped ceria catalysts (M=Zr, Zn and Fe) for the preferential oxidation of CO(PROX), *Journal of Catalysis,* 276, 360-370, (2010).

[154] Venkataramana K., Madhusudan C., Madhuri C., Reddy C. V., Synthesis, characterization and thermal expansion of Ce0.8-xSm0.2ZrxO2-δ solid electrolytes for IT-SOFC applications, *Materials Today: proceedings,* 3(10), 3908-3913, (2016).

[155] Lee M.J., Jung J.H., Zhao K., Kim B.H., Xu Q., Ahn B.G., Kim S.S.H. and Kim S.Y., Fabrication and electrochemical properties of SOFC single cells using porous yttria-stabilized zirconia ceramic support layer coated with Ni, *Journal of the European Ceramic Society,* 34(7), 1771-1776, (2014).

[156] Panthi D., Choi B. and Tsutsumi A., Direct methane operation of a micro-tubular solid oxide fuel cell with a porous zirconia support, *Journal of Solid State Electrochemistry,* 21, 255-262, (2017). [167]A. Mineshige *et al.*, "Introduction of A-site deficiency into La0. 6Sr0. 4Co0. 2Fe0. 8O3–δ and its effect on structure and conductivity," *Solid State Ionics,* vol. 176, no. 11-12, pp. 1145-1149, 2005.